Hydrophilic and Hydrophobic Microporous Layer Coated Gas Diffusion Layer to Enhance Performance of Polymer Electrolyte Fuel Cell

王, 鵬

Hydrophilic and Hydrophobic Microporous Layer Coated Gas Diffusion Layer to Enhance Performance of Polymer Electrolyte Fuel Cell

PENG WANG

Hydrogen Energy Systems

Graduate School of Engineering

Kyushu University, Fukuoka, Japan

January 2024

Contents

Acknowledgment

First and foremost, I extend my deepest appreciation to my supervisor, Assoc. Prof. Dr. Tatsumi Kitahara, for his unwavering support, invaluable guidance, and continuous encouragement throughout this journey. His expertise, dedication, and willingness to share knowledge played a pivotal role in the success of this project. He spent countless hours invested in guiding me through challenges and complexities. His generosity in sharing their expertise has been a source of inspiration and has left an indelible mark on the outcomes of this research.

I extend my sincere appreciation for Prof. Dr. Kohei Ito, whose meticulous approach to every aspect of the research process, from experimental design to data analysis, his attention to detail, and his insistence on scientific rigor have been instrumental in shaping my study attitude.

I appreciate Prof. Dr. Gen Inoue for the valuable comments, which have greatly helped me improve the research content of my thesis.

I am fortunate to have had the privilege of working alongside Asst. Prof. Dr. Hironori Nakajima has provided invaluable assistance in experiments, offering crucial insights and expertise that significantly enriched the quality of my research. His commitment to excellence and collaborative spirit created a positive and productive working environment.

I am also grateful to the Japan New Energy and Industrial Technology Development Organization (NEDO) for funding my doctoral studies at Kyushu University in Japan.

To Linjun Li, Songsong Ma, Xuefeng Wang, Ziyi Wu, and Xiaoning Zhang, our working life has been a journey marked by shared dedication, mutual support, and the joy of working together towards a common goal. Thank you all for the memories we have created together.

Lastly, I have special thanks to my family for their unwavering support throughout my academic journey. My parents, my aunt, and my girlfriend, their love, encouragement, and understanding have been the pillars that sustained me during the highs and lows of this challenging endeavor. My heartfelt appreciation extends to the entire family for creating an environment where learning is valued, and aspirations are supported. Your patience during demanding times and your celebration during moments of success have made this journey more meaningful. Thank you for being the foundation of my success.

PENG WANG

Kyushu university, Fukuoka, Japan

January 2024

List of Figures

List of Tables

Nomenclature

Symbol	Meaning
A	Cross-sectional area (cm^2)
b	Fitting line slope
$C_{O2,channel}$	Oxygen concentration in the flow channel (mol m^{-3})
$C_{O2,electrode}$	Oxygen concentration at the CL (mol m^{-3})
C_{ref}	Standard oxygen concentration (mol m^{-3})
d	Pore diameter (μm)
d_j	Specific pore diameter (μm)
d_{max}	Maximum pore diameter (μm)
E	Reversible voltage (V)
F	Faraday constant (96485 C/mol)
G	Gibbs free energy (kJ)
h	Length of the pore (m)
i	Current density (A cm^{-2})
i_0	Exchange current density (A cm^{-2})
i_{lim}	Limiting current density (A cm^{-2})
j	Serial number of pore diameter
K	Absolute permeability (m^2)
k_{O2}	Relative oxygen permeance
n	Number of electrons in the reaction
n_j	Number of water-permeable pores with specific pore diameter
p	Pressure (Pa)
p_0	Atmospheric pressure (Pa)
p_{O2}	Oxygen partial pressure (Pa)
p_{H2}	Hydrogen partial pressure (Pa)

p_{H2O}	Water partial pressure (Pa)
p_c	Capillary pressure (Pa)
p_j	Capillary pressure with specific pore diameter (Pa)
q_{water}	Water flow rate ($cm^3\ min^{-1}$)
q_j	Water flow rate with specific pore diameter ($cm^3\ min^{-1}$)
Q_{water}	Water permeability ($cm\ min^{-1}$)
Q_{vapor}	Water vapor flow rate ($mg\ min^{-1}$)
q_{vapor}	Water vapor permeance ($mg\ min^{-1}\ cm^{-2}$)
$q_{O2,dry}$	Oxygen permeance of dry GDL ($cm\ min^{-1}$)
$q_{O2,wet}$	Oxygen permeance of wet GDL ($cm\ min^{-1}$)
R	Gas constant ($8.314\ J\ mol^{-1}\ K^{-1}$)
R_{O2}	Total oxygen transport resistance under specific conditions ($s\ m^{-1}$)
R_{ch}	Oxygen transport resistance in the flow channel ($s\ m^{-1}$)
R_{GDL}	Oxygen transport resistance in the GDL ($s\ m^{-1}$)
R_{CL}	Oxygen transport resistance in the CL ($s\ m^{-1}$)
R_{mol}	Molecular diffusion resistance ($s\ m^{-1}$)
R_{other}	Resistance except for molecular diffusion ($s\ m^{-1}$)
R_p	Pressure-dependent resistance ($s\ m^{-1}$)
R_{np}	Pressure-independent oxygen transport resistance ($s\ m^{-1}$)
R_Ω	Ohmic resistance (Ω)
s_l	Water saturation
s_g	Gas saturation
T	Temperature (K)
T_{cell}	Cell temperature (°C)
$V_{C2\text{-}C1}$	Voltage change from concentration change (V)
V_C	Voltage under specific concentration (V)
V_{ocv}	Open circuit voltage (V)

Greek symbol	Meaning
α	Charge transfer coefficient
γ	Surface tension of wetting liquid (N m^{-1})
ε	Porosity
η	Equilibrium potential (V)
θ	Surface contact angle (deg)
θ_{pore}	In-pore contact angle (deg)
μ	Viscosity coefficient (Pa s)

1. Introduction

1.1 Background

1.1.1 The Hydrogen Energy and Fuel Cell

As fossil energy is gradually consumed, attention is growing toward its diminishing reserves and the environmental pollution it causes [1]. To relieve the reliance on fossil energy and reduce ecological damage, the countries are actively striving to explore a new generation of alternative energy sources.

Hydrogen, a renewable energy source and an abundant element in the Earth that can be harnessed from various sources, including water electrolysis and organic compounds, has received widespread attention from all walks of life [2]. Hydrogen is a widely adopted energy carrier in chemical production and power generation, known for its non-toxic nature and safe handling, with applications spanning the automotive, electronics, and construction sectors [3,4]. Moreover, hydrogen presents numerous advantages as an energy carrier, including minimal emissions of greenhouse gases and hazardous substances during energy release, its compatibility with fuel cells, and its role as a sustainable alternative to traditional fuels like gasoline, diesel, and natural gas [5-7].

Within the realm of fuel cell systems, polymer electrolyte fuel cell systems (PEFCs) stand out for their rapid start-up, compact size, high efficiency, low operating temperatures, impressive power density, stable operation, and absence of environmental emissions [8-10]. In its capacity as a power generation system, the chemical potential in the hydrogen is efficiently transformed into electrical energy, producing water and heat as byproducts [11-13]. By assembling and compressing the multiple individual cells to generate different characteristic stacks of PEFC to satisfy the usable output voltage needs of various application scenarios [14]. These attributes make PEFCs ideal for various commercial applications across the automotive, rail, maritime, drone, and aviation transportation industries [15-17]. Given the growing ecological and global warming concerns, PEFCs are recognized as a clean solution for automotive powertrains, especially for heavy-duty vehicles (HDV) [18].

1.1.2 The Components and Working Principle of PEFC

PEFCS are intricate systems composed of several essential components, each with a unique role in ensuring efficient operation [19]. These pivotal elements include the anode, cathode, catalyst layer (CL), proton exchange membrane, microporous layer (MPL) coated gas diffusion layer (GDL), and bipolar plate (BP), as illustrated in Figure 1.1 [20].

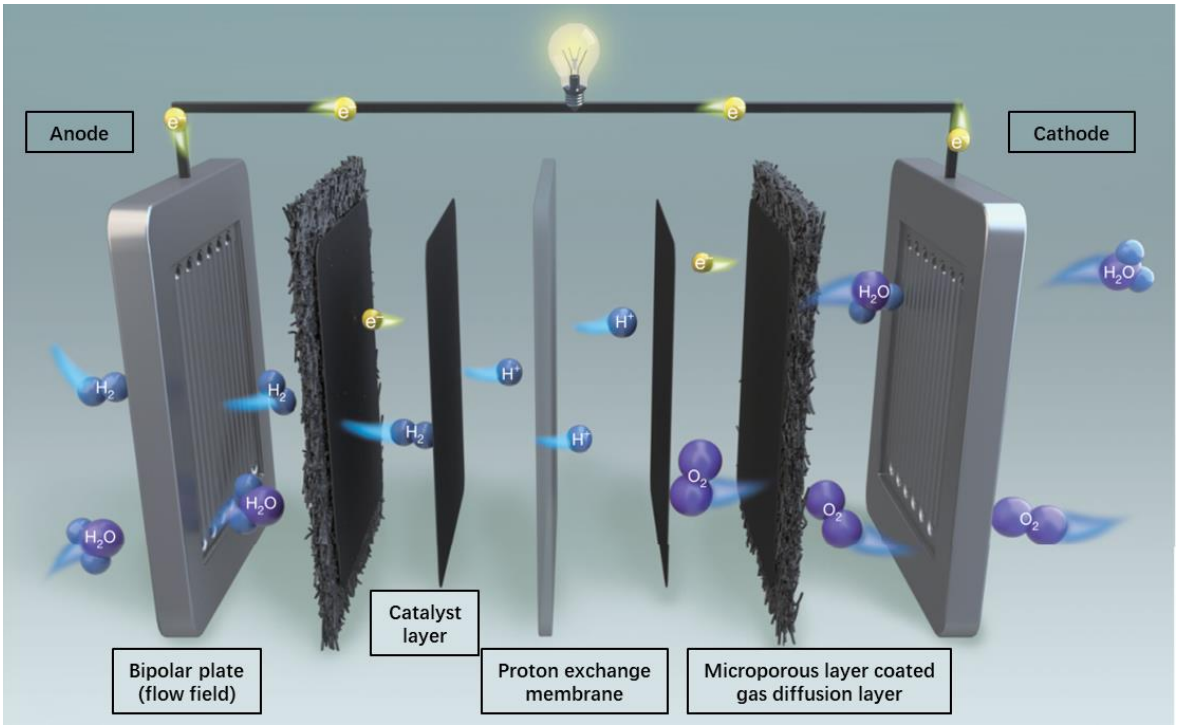

Figure 1.1 The schematic diagram of the working principle of the polymer electrolyte fuel cell (PEFC) [20].

Bipolar plates assume a pivotal role in the intricate functioning of fuel cells, orchestrating the flow of electrons from the anode to the cathode, either within the external circuit or to the adjacent cathode in a stack. Simultaneously, they facilitate the seamless transport of fuel and the removal of reaction byproducts through carefully delineated channels. Moreover, these plates contribute to the structural integrity of the stack and efficiently dissipate the waste heat generated during the reaction, employing a coolant flow through the current collector [21-23].

The CL takes center stage within the cell by enabling fuel oxidation and reduction reactions. This multifaceted role involves supplying the necessary catalyst, conducting ions from the reaction site to the membrane, guiding electrons from the reaction site to the anode bipolar plate, and facilitating the transport of reactants and removal of products to and from the catalyst locations.

The proton exchange membrane (PEM) embodies diverse critical functions, including high ionic conductivity, minimal crossover of hydrogen and oxygen gases, chemical stability, thermal resilience across a spectrum of operating temperatures, and robust mechanical strength [24]. The perfluorosulfonic acid (PFSA) membrane currently stands as the prevailing choice. When coated with CLs, this membrane transforms into a cohesive unit called the catalyst-coated membrane (CCM) [25,26].

Nestled between the bipolar plate and CCM, the GDL is pivotal in optimizing cell performance [27]. It serves many functions, providing crucial mechanical support, facilitating the transfer of water, gas, and heat, and ensuring efficient electrical conduction. Modern GDLs typically comprise a carbon-based substrate and an MPL [28-30]. The substrate, fashioned from either carbon paper, carbon felt, or carbon fibers as shown in Figure 1.2, undergoes impregnation with a hydrophobic agent polytetrafluoroethylene (PTFE), with loadings ranging from 5-30 wt.% [31-33]. One side of the fiber substrate is commonly coated with an MPL comprising a hydrophobic polymeric binder, carbon black, or graphite. The total uncompressed thickness of cutting-edge GDLs falls within the 100-250 μm range, with an MPL thickness ranging from 20 to 50 μm. Pore sizes exhibit variability, ranging from 10-80 μm in the substrate to 30 nm to 20 μm in the MPL [34].

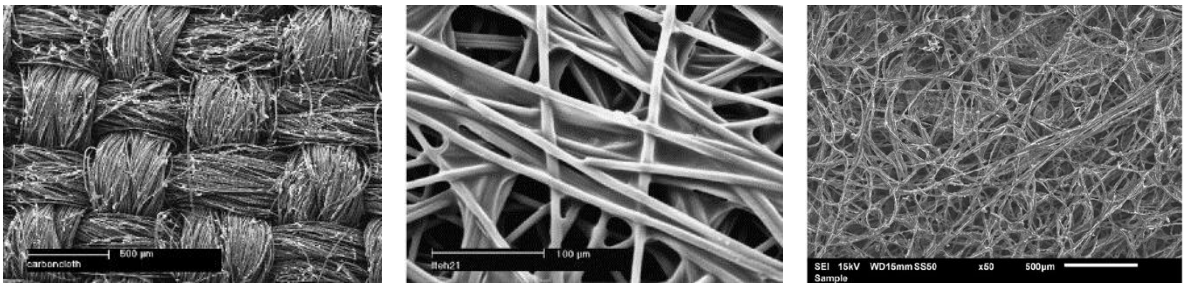

(a) Carbon cloth (b) Carbon paper (c) Carbon felt

Figure 1.2 The different substrates of (a) carbon cloth, (b) carbon paper [31], and (c) carbon felt used in MPL coated GDLs [32].

To initiate the PEFC energy generation process, hydrogen is introduced into the system at the anode, which divides hydrogen molecules into electrons and protons via the hydrogen oxidation reaction (HOR) denoted as Eq. (1.1). Subsequently, the bipolar plates efficiently capture the released electrons from the hydrogen atoms, generating an electric current capable of powering various external electronic devices [35,36].

Simultaneously, the separated protons, originating from the hydrogen at the anode, traverse the proton exchange membrane (PEM). This specialized membrane allows for the selective transport of protons, facilitating their movement from the anode to the cathode [37]. Upon reaching the cathode, the protons unite with oxygen from the surrounding environment, participating in a chemical reaction that yields water as a byproduct of the oxygen reduction reaction (ORR) represented by Eq. (1.2). This reaction within the PEFC system plays a pivotal role in its environmentally friendly operation by producing clean water without harmful emissions as the overall reaction as Eq. (1.3) [36].

$$H_2 \rightarrow 2H^+ + e^- \tag{1.1}$$

$$H_2 + \frac{1}{2}O_2 + 2e^- \rightarrow H_2O \tag{1.2}$$

$$H_2 + \frac{1}{2}O_2 \rightarrow H_2O \tag{1.3}$$

In summary, the PEFC is a remarkable piece of technology, ingeniously designed to split hydrogen into electrons and protons, with the former being channeled to power external electrical devices and the latter used to create water through a proton exchange membrane (PEM). This process underscores the importance of PEFC in sustainable and clean energy solutions, making it a promising technology for a greener future [38].

1.1.3 The Overpotentials During PEFC Operation

During PEFC operation, the cell performance can be effectively assessed through the polarization curve (I-V curve) [39], as illustrated in Figure 1.3. This curve is a comprehensive indicator, encapsulating essential data regarding cell voltage, current density, and output power.

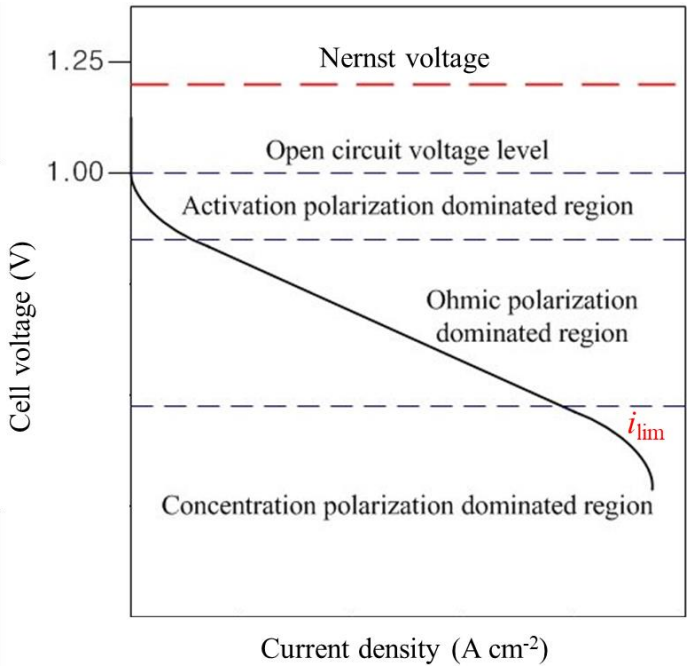

Figure 1.3 The polarization curve and various overpotentials during PEFC operation [39].

As for the maximum ideal voltage (Nernst voltage) in the PEFC, the Nernst equation shows the reversible cell voltage $E(T, p)$ as a function of temperature T and pressure p. For an ideal gas mixture in PEFCs, the Nernst equation can be written as Eq. (1.4).

$$E(T,p) = \frac{-\Delta G}{nF} + \frac{RT}{nF}\ln\frac{p_{H_2}p_{O_2}^{\frac{1}{2}}}{p_{H_2O}} \tag{1.4}$$

where ΔG is the Gibbs free energy (kJ), n is the number of electrons involved in the electrode reaction, F is the Faraday constant (96485 C/mol), R is the gas constant (8.314 J mol^{-1} K^{-1}), T is the temperature (K), p_{H2}, p_{O2}, and p_{H2O} are hydrogen, oxygen, and water partial pressures, respectively (kPa).

However, the species crossover through the electrolyte, internal electron leakage, or potential contamination and impurities caused the undesired disparity between the ideal and open circuit voltage (OCV) results. Moreover, the actual power output of PEFCs is also subject

to the influence of various irreversible voltage losses, specifically, ohmic overpotential, activation overpotential, and concentration overpotential [40].

(a) Activation overpotential

Activation overpotential, a kinetic hindrance occurring at the electrodes, mainly causes the potential drop at the beginning of the operation, as shown in Figure 1.3. It can be expressed by a classical model of the Bulter-Volmer (BV) equation (1.5). The BV model describes an electrochemical process limited by the charge transfer of electrons.

$$i = i_0 \left[\exp\left(\frac{\alpha n F \eta}{RT}\right) - \exp\left(\frac{-(1-\alpha) n F \eta}{RT}\right) \right] \tag{1.5}$$

where i is the net current density, i_0 is the exchange current density, α is the charge transfer coefficient, and under equilibrium is 0.5, η is the equilibrium potential (V).

When focusing on the increasing η of the anodic or cathodic branch, the rest will be diminished so that the BV equation can be simplified as Eq. (1.6).

$$i = i_0 \exp\left(\frac{\alpha n F \eta}{RT}\right) \tag{1.6}$$

Taking the logarithm of both sides simultaneously in Eq. (1.6) and moving the η to the left side, the Tafel equation is obtained as Eq. (1.7). According to this relationship, the activation overpotential can be separated from the initial range of the polarization curve.

$$\eta = \frac{RT}{\alpha n F} \ln\left(\frac{i}{i_0}\right) \tag{1.7}$$

(b) Ohmic overpotential

The ohmic overpotential encompasses all electrical and ionic conduction losses spanning the electrolyzer, catalyst layers, cell interconnects, and contacts. It becomes dominant in the middle of the operation in Figure 1.3. This loss is profoundly affected by the thickness, conductivity, and surface roughness of the GDL coated with an MPL. Furthermore, managing water within the MEA is essential in dictating ohmic loss. Variations in wettability can significantly impact the proton conductivity of the membrane. When the MEA lacks adequate wetness, the dry membrane impedes the transport of protons, leading to an increase in ohmic resistance. The ohmic overpotential can be determined through high-frequency resistance (HFR), electrochemical impedance spectroscopy (EIS), or current interruption method.

(c) Concentration overpotential

The concentration overpotential arises from limitations in the mass transport of reactants to the catalyst. This loss influences the I-V characteristic before the PEFC system stabilizes, particularly under low ambient temperature and high current density conditions. Besides, higher current densities generated by the oxygen reduction reaction (ORR) at the cathode within the catalyst layer produce excess liquid water [37,41,42]. This scenario gives rise to the challenge of liquid water accumulation within the cell, especially on the cathode side [43,44]. The accumulation leads to liquid water blockage in the pores of the electrolyte and GDL, causing a significant reduction in the oxygen transport rate to the catalyst when the oxygen concentration becomes zero, where the limiting current density occurs in Figure 1.3. In cases where the system fails to expel water through the GDL efficiently, this accumulated water hampers reactions, resulting in a voltage drop known as flooding. The limitation in oxygen diffusion primarily depends on the oxygen diffusion capability on the cathode side of the fuel cell engine, a factor significantly influenced by the properties and structure of the cathode-side CL and GDL [45,46]. The voltage change at the electrode due to concentration changes in reactant diffusion can be described by Eq. (1.8). Assuming the reaction occurs only at the CL, kinetic effects can be ignored, as shown in the left parts of Eq. (1.9).

$$\Delta V_{C_2-C_1} = \eta = V_{C_2} - V_{C_1} = \frac{RT}{(n+\gamma)F}\ln\left(\frac{C_2}{C_1}\right) \tag{1.8}$$

$$\eta = -\frac{RT}{nF}\ln\left(1-\frac{i}{i_{\lim}}\right) \tag{1.9}$$

where the $V_{C2\text{-}C1}$ is the voltage change from concentration change (V), V_C is the voltage under specific concentration (V), γ is the reaction order, C is the reactant concentration (mol m^{-3}), the i_{lim} is the limiting current density (A cm^{-2}).

Among all the overpotentials, the concentration overpotential is the main factor influencing the power output under high current density. Therefore, an effective water management strategy in the PEFC should have the dual objectives of preventing dehydration of the MEA by utilizing water generated by electrochemical reactions in dry conditions while expelling excess water from the catalyst layer. This approach helps maintain gas diffusion to reduce concentration overpotential during high relative humidity or high current density conditions

[47-49]. Thus, the MPL part becomes indispensable to achieve this favorable MPL/CL interface water-gas transport balance within the cells [50-52].

1.1.4 The Mass Transport in PEFC

A profound understanding of mass transport mechanisms is essential for designing and optimizing the MPL coated GDL in PEFC. The intricacies of the transport mechanisms are notable, necessitating the use of complex equations. The mechanisms explicitly involve the movement of gases and liquids within the cell, the fundamental processes significantly influencing the overall performance of the PEFC [53-55]. Recognizing and delving into a detailed exploration of the intricate interplay among various factors affecting gas and liquid transport is essential to establishing the groundwork for targeted MPL coated GDL design and improvement, ensuring optimal performance and efficiency in PEFCs.

1.1.4.1 The Oxygen Transport in the PEFC

Before modifying the cell components, it is crucial to grasp the oxygen diffusion mechanism. The flow channel must supply oxygen to the catalyst, traversing through the GDL, MPL, and CL. Since these layers have distinct pore distributions and structures, the varying pore size distributions yield unique gas and water transport properties.

Considering the oxygen transport components from GDL to CL in Figure 1.1, the total oxygen transport resistance R_{O2} can be divided into several parts for easier understanding [56], as Eq. (1.10).

$$R_{O2} = R_{ch} + R_{GDL} + R_{MPL} + R_{CL} \tag{1.10}$$

where R_{O2} is the total oxygen transport resistance from the flow channel to the CL, R_{ch} is the oxygen transport resistance in the flow channel, R_{GDL} is the oxygen transport resistance in the GDL, R_{MPL} is the oxygen transport resistance in the MPL, R_{CL} is the gas transport resistance in the catalyst layer.

During the cell operation, the I-V curve exhibited i_{lim} behavior where the oxygen concentration in the CL tends to be zero, as shown in Figure 1.3. From Baker et al. research, the R_{O2} in the cell is calculated as the difference in oxygen concentrations between the flow-field inlets and the electrode divided by the average oxygen flux to the electrode [57], as Eq. (1.11).

$$R_{O2} = \frac{C_{O2,channel} - C_{O2,CL}}{\overline{Oxygen\ Flux}} = \frac{4F}{RT}\frac{p_{O2}}{i_{lim}} \tag{1.11}$$

Where the $C_{O2,channel}$ is the oxygen concentration in the flow channel (mol m^{-3}), $C_{O2,electrode}$ is the oxygen concentration at the CL (mol m^{-3}), p_{O2} is the oxygen partial pressure (Pa).

In Figure 1.4, the oxygen transport mechanism significantly changed from GDL to CL with varying pore sizes. The molecular diffusion mainly occurs in the MPL and GDL, and the Knudsen diffusion becomes dominant with the decreasing pore structures in the CL [58]. Therefore, based on Baker's report, the R_{O2} can be further decomposed into two components: molecular diffusion resistance R_{mol} and the remaining resistance R_{other} as Eq. (1.12) [59,60].

$$R_{O2} = \frac{4FC_{O2}}{i_{lim}} = R_{mol}\frac{p}{p_0} + R_{other} \tag{1.12}$$

where C_{O_2} is the concentration of oxygen molecule (mol m^{-3}), p is the partial pressure (Pa), p_0 is the reference total pressure (0.1 MPa), C_{O2} is the oxygen concentration (mol m^{-3}), R_{mol} is the molecular diffusion resistance (s m^{-1}), R_{other} is the resistance of Knudsen diffusion and diffusion within the ionomer and liquid water (s m^{-1}),

The initial resistance in Eq. (1.12) primarily arises from intermolecular diffusion within the GDL, characterized by relatively large pores, with diffusion coefficients inversely proportional to the total pressure, as shown in Figure 1.5(a) and (b). The subsequent resistance is associated with diffusion in the CL, featuring small pores and a thin ionomer layer, as shown in Figure 1.5(c) [61-63].

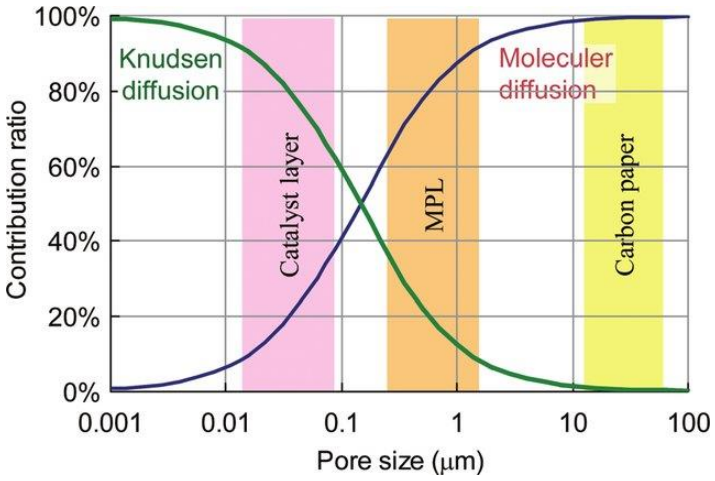

Figure 1.4 The mechanisms of oxygen diffusion in PEFC [58].

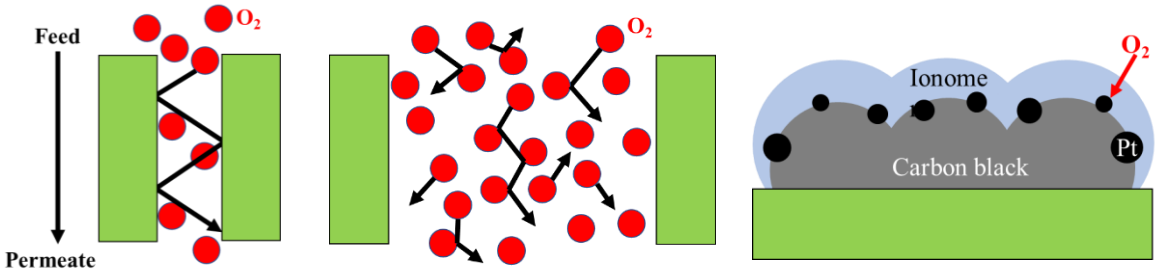

(a) Knudsen diffusion. (b) Molecular diffusion. (c) The oxygen permeation through the ionomer film.

Figure 1.5 The (a) Knudsen diffusion, (b) molecular diffusion, and (c) ionomer permeation of the oxygen.

In this context, gas transport is predominantly influenced by pressure-independent Knudsen diffusion and diffusion within the ionomer and liquid water. Therefore, the R_{O2} under a specific condition can be described as Eq. (1.13).

$$R_{O2} = R_p + R_{np} \tag{1.13}$$

where R_p and R_{np} are pressure-dependent and pressure-independent oxygen transport resistances (s m^{-1}), which respectively correlate to R_{mol} and R_{other}.

According to the above analysis, reducing overpotential in oxygen diffusion hinges on minimizing the low oxygen diffusion resistance, with R_p and R_{np} serving as benchmarks for evaluating GDL modification.

1.1.4.2 The Liquid Water Transport Mechanisms in the PEFC

The typical operating temperature range for a PEFC is 60°C to 100°C [64]. However, during start-up or cold start conditions, the cell undergoes a state change before reaching a steady state under lower temperatures. Consequently, water in the system exists not only in the gas phase but also in the liquid phase. Effective water management in this PEFC is crucial. The system must expel excess water to prevent drainage and maintain the CL in highly humid conditions to enhance the membrane proton conductivity [65,66]. However, the appearance of condensed liquid water on the cathode catalyst layer brings high water saturation s_l and lowers the effective surface area of Pt metal, as shown in Figure 1.6 [40,67,68].

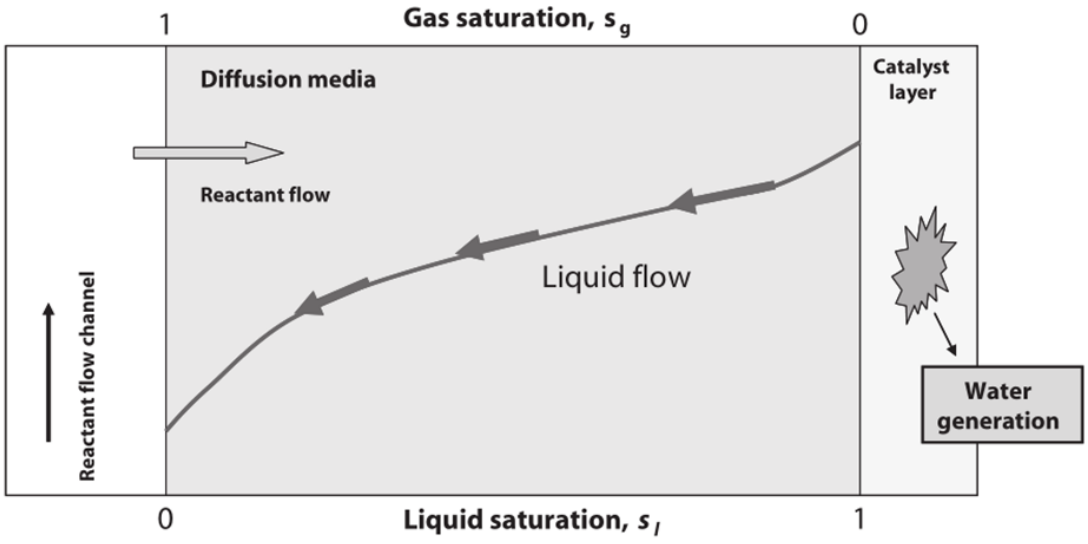

Figure 1.6 Capillary-induced liquid transport in a hydrophobic fuel cell GDL [40].

Meanwhile, the high s_l impedes oxygen diffusion and reduces gas saturation s_g. The accumulated water at the CL can passivate active sites, reducing the efficiency of gas molecule diffusion to the CL surface. Similarly, the active pore area may become partially blocked if water droplets gather at the GDL [53].

The central aspect of water transport in MPL coated GDLs focuses on capillary pressure [69-71]. This pressure disparity arises in the MPL coated GDL when gas and liquid water coexist in the PEFC. The pressure difference at the interface between these phases results from interfacial tensions caused by the imbalance of molecular forces at the contact line. The disparity between the pressure of liquid water p_l and gas p_g at the interface is termed capillary pressure p_c, which utilizes the widely recognized Levertte approach in Eq. (1.14) and Eq.(1.15),

providing a means to assess the pressure required for a non-wetting fluid to infiltrate a square cross-sectional pore [72-74]. The water generated is not stationary, and the liquid water migrates from the catalyst to the gas channel. As Leverett's approach describes, the p_c influences the water saturation s_l. Consequently, pore size and hydrophobicity alterations induced by p_c changes lead to diverse liquid water transport properties. Specifically, decreasing pore size and increasing contact angle can reduce the saturation level within a specified range [75,76].

$$p_c = \gamma \cos \theta_{pore} \left(\frac{\varepsilon}{K}\right)^{0.5} J(s_l) \tag{1.14}$$

$$J(s) = 1.417 s_l - 2.120 s_l^2 + 1.263 s_l^3 \tag{1.15}$$

where p_c is the capillary pressure, γ is the wetting liquid's surface tension, θ_{pore} is the in-pore contact angle, K is the absolute permeability, ε is the porosity, and s_l is liquid water saturation.

1.2 The Role of the Hydrophobic MPL

Effective water management in MPL coated GDLs becomes crucial for achieving lower R_{np} and R_p resistances while simultaneously achieving higher output power at a specific current density. A widely adopted practice in the industry involves extensively using conventional hydrophobic MPL coated GDLs to regulate liquid water and maintain a consistent oxygen supply within the MEA, and the configuration is shown in Figure 1.7 [77,78].

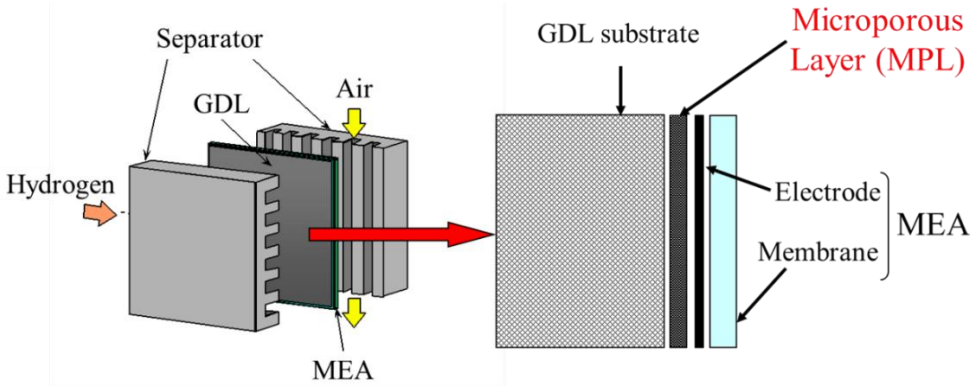

Figure 1.7 The MPL coated GDL configuration in the PEFC.

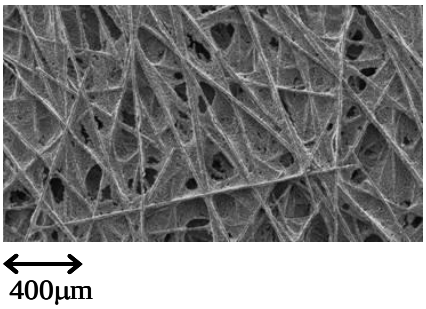

(a) SGL24BA without MPL

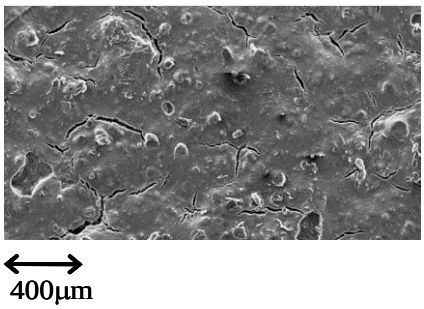

(b) SGL24BC with MPL

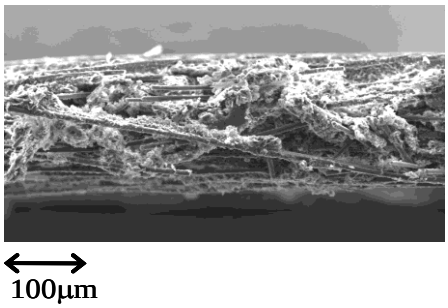

(c) SGL24BA without MPL

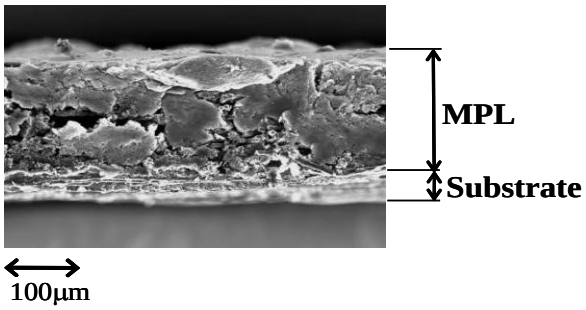

(d) SGL24BC with MPL

Figure 1.8 The SEM photos of the commercial bare carbon paper (SGL 24BA) are in (a) and (c), and commercial MPL coated GDL (SGL 24BC) is in (b) and (d) [79].

This approach entails the utilization of hydrophobic MPLs, frequently in conjunction with a polytetrafluoroethylene (PTFE) binder. In Figure 1.8, SEM images compare a commercial substrate (SGL 24BA) with a commercial MPL coated GDL (SGL 24BC), illustrating the direct application of the hydrophobic MPL onto the substrate. This application forms smaller pore structures with varying degrees of hydrophobicity within the MPL [79]. The smooth surface of MPL also helps reduce contact resistance between the MPL and the CL.

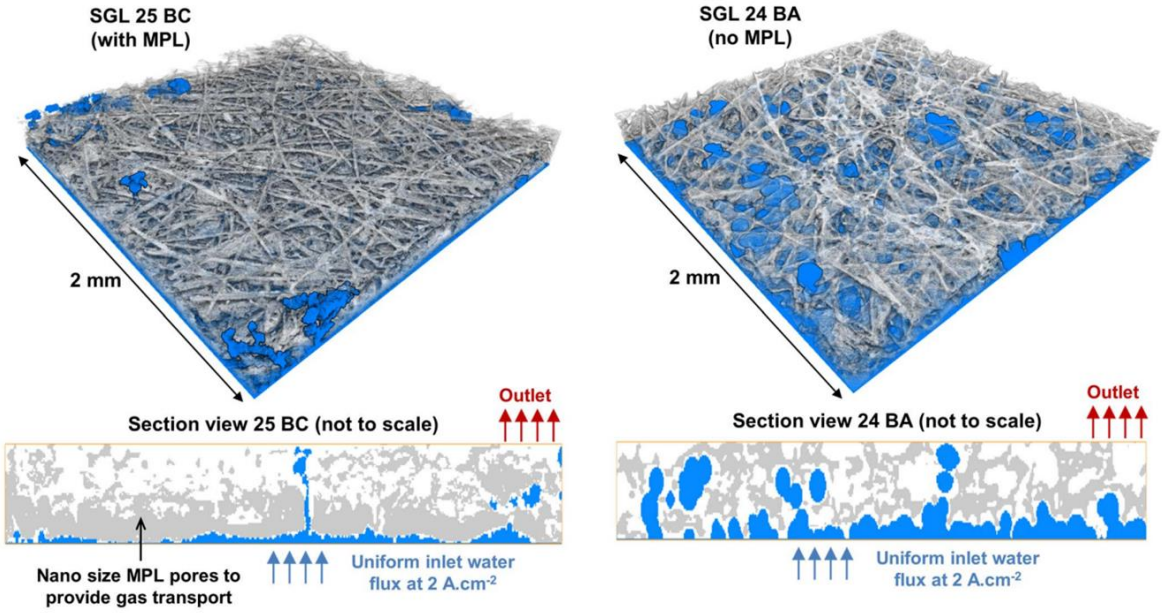

(a) SGL 25BC (b) SGL 24BA

Figure 1.9 Simulated liquid water (blue) distribution at steady state along with microstructures (light gray) of (a) SGL 25 BC and (b) SGL 24 BA [80].

Besides, the experimental and simulation reports have shown that introducing the MPL can reduce the saturation level [53]. Cetinbas et al. adopted a 110° contact angle for commercial SGL 24BA and SGL 25BC fibers and a 120° contact angle for the MPL material in the 25BC scenario [80]. As depicted in Figure 1.9, the model results reveal multiple water breakthroughs occurring at various locations and time steps under these conditions. The simulation result suggested the formation of very few water paths from the inlet to the outlet of the SGL 25BC setup because the MPL material, comprising hydrophobic nano-pores, limits water intrusion into the GDL, as shown in Figure 1.9(a). The nano-pores act as barriers preventing water flow, while more considerable pores are conduits for draining accumulated water under elevated pressure. In contrast, Figure 1.9(b) shows many water clusters, with a small fraction reaching

a breakthrough at the outlet of SGL 24 BA. Consequently, only a limited number of distinct water paths were established from the electrode to the outlet boundary of the SGL 25BC system, and most of the water accumulated at the CL/MPL interface, creating a barrier to oxygen transport to the catalyst. As illustrated in the section view, liquid water accumulates in the middle and lower heights of SGL 24 BA with the gas-blocking effect.

As shown in Figure 1.10, Sarker et al. compared commercial GDL (Toray-H-060) to hydrophobic MPL coated GDL through I-V curves under both relatively dry and wet conditions [81]. Under dry operating conditions, no significant differences are observed, as kinetic and ohmic losses primarily dominate the polarization curve, as shown in Figure 1.10(a). In contrast, under wet operating conditions, especially in the mass transport region, the impact of PTFE impregnation and MPL becomes more evident, as illustrated in Figure 1.10(b). The collective findings indicate that water condenses rapidly, reaching a high saturation level in the bare GDL. In contrast, the sample with 5 wt% PTFE impregnation and MPL maintains a low water saturation level, demonstrating the capacity of MPL to handle liquid water and facilitate oxygen transport at high current densities. Adding MPL to the cathode GDL is crucial for establishing stable operation under wet conditions, especially for high current density operations.

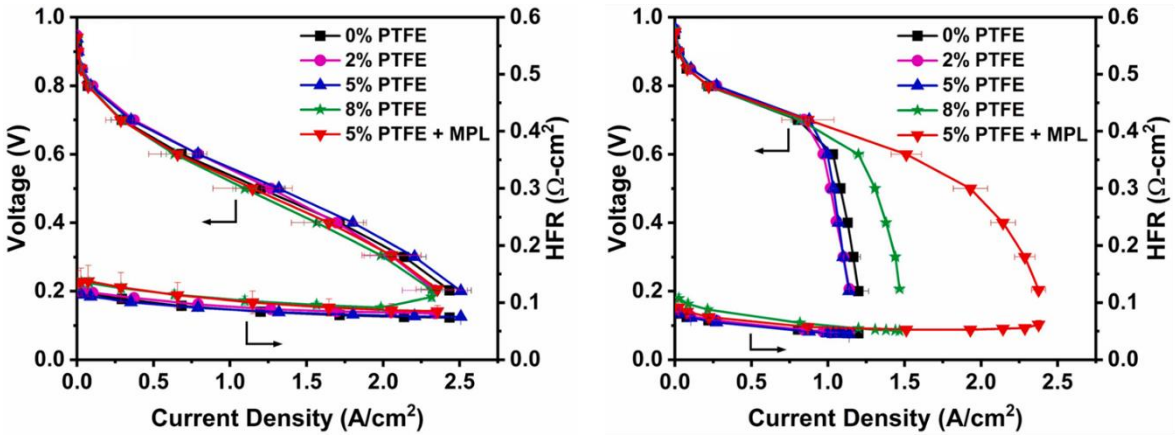

(a) 70 °C, 64%RH, 100 kPa abs (b) 70 °C, 100%RH, 300 kPa abs

Figure 1.10 Performance curves for Toray-H-060 with 0, 2, 5, 8 wt% PTFE and 5 wt% PTFE with MPL under (a) dry conditions, 70 °C, 64% RH, 100 kPa abs, and (b) wet conditions, 70 °C, 100% RH, 300 kPa abs [81].

Furthermore, Kitahara et al. reported similar I-V curves and overpotential results for the commercial untreated GDL (SGL 20AA), GDL with hydrophobic treatment (SGL 20BA), and

hydrophobic MPL coated GDL (SGL 20BC), as shown in Figure 1.11 [82]. Under 100%RH, the performance of the PEFC using the 20BA GDL with PTFE treatment surpasses that of the 20AA GDL at high current densities, and even superior performance is achieved when employing the 20BC GDL with the MPL. Although the IR and activation overpotentials exhibit relative uniformity across all GDLs, both PTFE treatment and the inclusion of the MPL prove effective in reducing flooding and suppressing concentration overpotential. Notably, the best performance under high humidity conditions is observed with the 20BC GDL featuring the MPL. Extra investigation of the I-V curve and overpotentials of the hydrophobic MPL coated GDL under different humidity conditions are shown in Figure 1.12. It was found that the humidity in the cell significantly influenced the output power, and the hydrophobic MPL coated GDL cannot always bring the suitable water management manner to prevent drying up and flooding when the humidity changed from low to high [82,83].

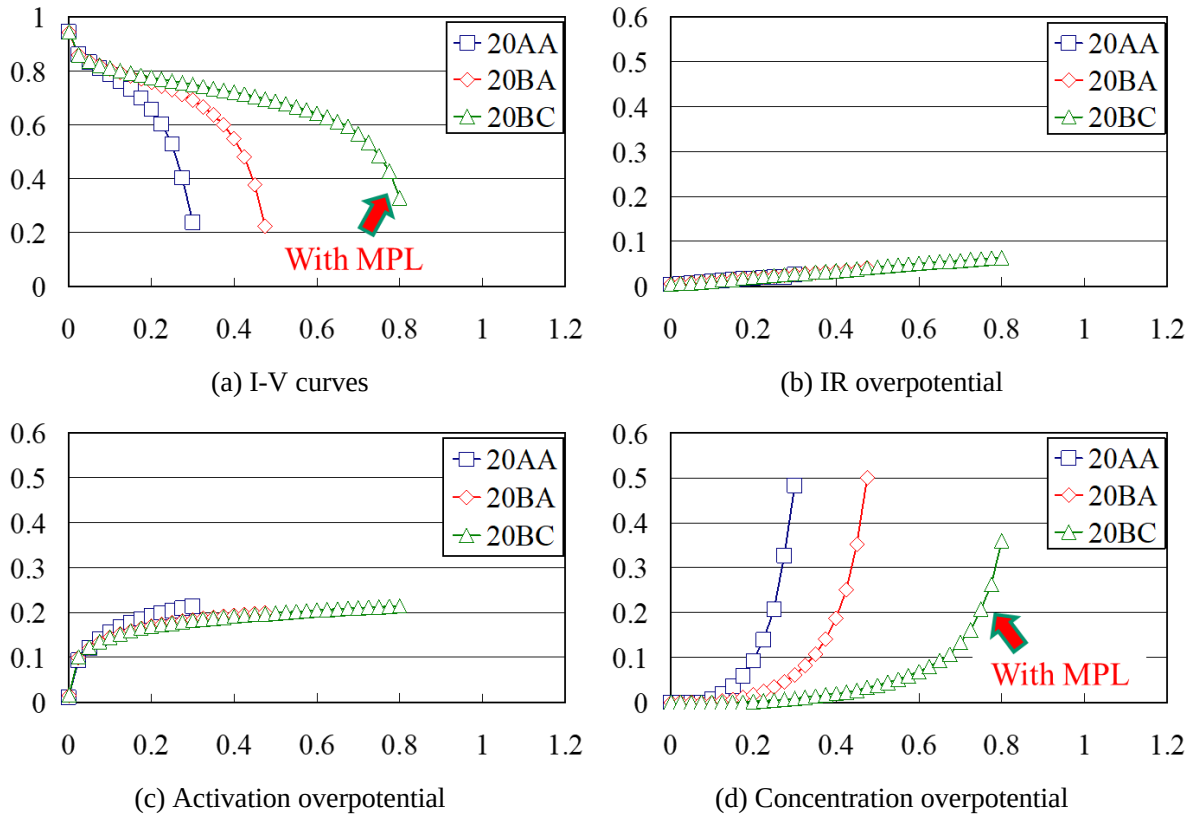

Figure 1.11 The I-V and overpotentials of commercial bare GDL and GDL with MPL under mild humidity conditions (100%RH) [82].

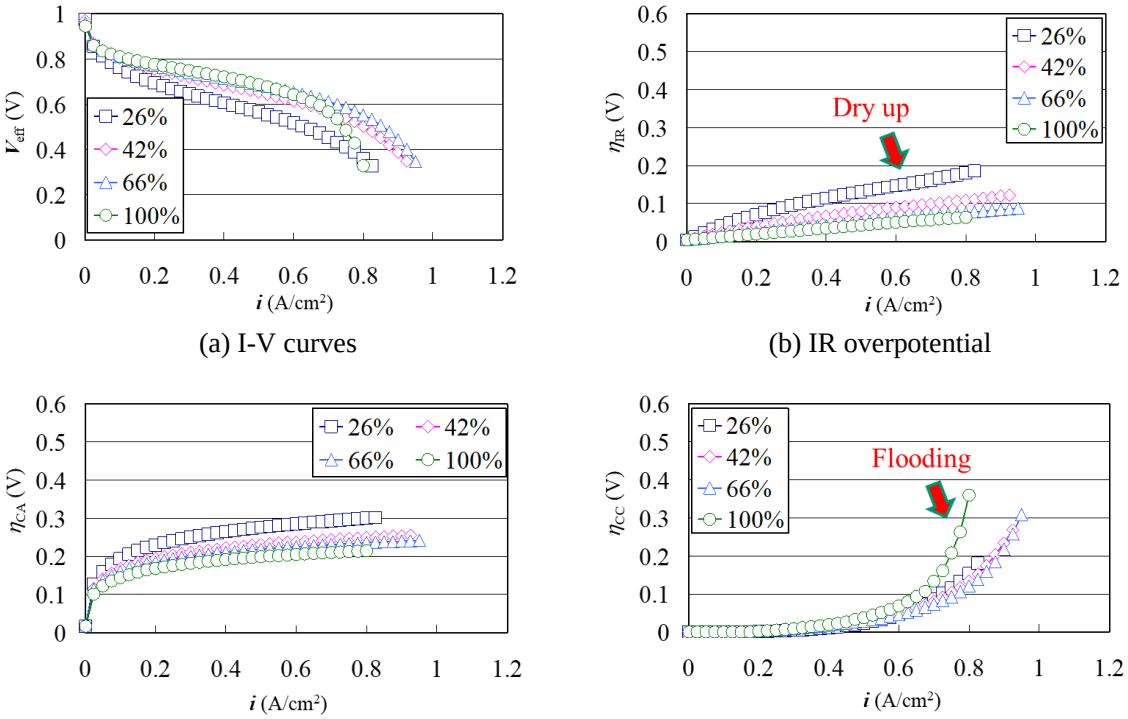

(a) I-V curves

(b) IR overpotential

(c) Activation overpotential

(d) Concentration overpotential

Figure 1.12 The I-V and overpotentials of hydrophobic MPL coated GDL under different humidity conditions [82].

Hence, the hydrophobic MPL serves a dual purpose: facilitating water removal from the catalyst layer during high humidity and high current density conditions and preventing membrane dehydration in low humidity environments. This dual functionality efficiently manages water in PEFCs, successfully minimizing the R_{O2} [84,85]. The strategic incorporation of hydrophobic MPL coated GDLs elevates the adaptability of PEFCs to diverse environmental conditions, ultimately optimizing their overall performance. Although the hydrophobic MPL coated GDL could improve PEFC performance to a certain extent by certain water management capabilities under some conditions, to improve the performance of PEFC further, modification of geometric parameters and properties is necessary.

1.2.1 The Target Performance from NEDO

Before the novel MPL coated GDL design process, it is also necessary to determine the development target, such as performance evaluation methods and target performance values. To gradually realize the power density enhancement of PEFCs utilized in HDV, the Japanese Industrial Technology Development Organization (NEDO) roadmap outlines specific targets for the I-V curve, as illustrated in Figure 1.13 [86]. By 2030, the beginning of life (BOL) condition should reach 0.7 V at 3 A cm^{-2}, which aims to increase output power more than the PEFC in the second generation of Toyota MIRAI vehicles. Eq. (1.16) is employed to introduce changes in activation, gas diffusion resistance, and ohmic resistance relative to the existing I-V characteristics. This equation allows for a quantification of the impact of samples on activation, gas diffusion resistance, and other parameters influencing the I-V curve characteristics.

$$V = V_{\mathrm{OCV}} - R_{\Omega} i - \frac{RT}{\alpha F}\log\left(\frac{i}{i_0}\right) - \frac{RT}{\alpha F}\log\left(\frac{C_{\mathrm{ref}}}{C_{\mathrm{O2}} - R_{\mathrm{O2}}\frac{i}{4F}}\right) \tag{1.16}$$

where V is voltage, R_{Ω} is the ohmic resistance (Ω), V_{ocv} is the open circuit voltage (V), C_{ref} is the standard oxygen concentration.

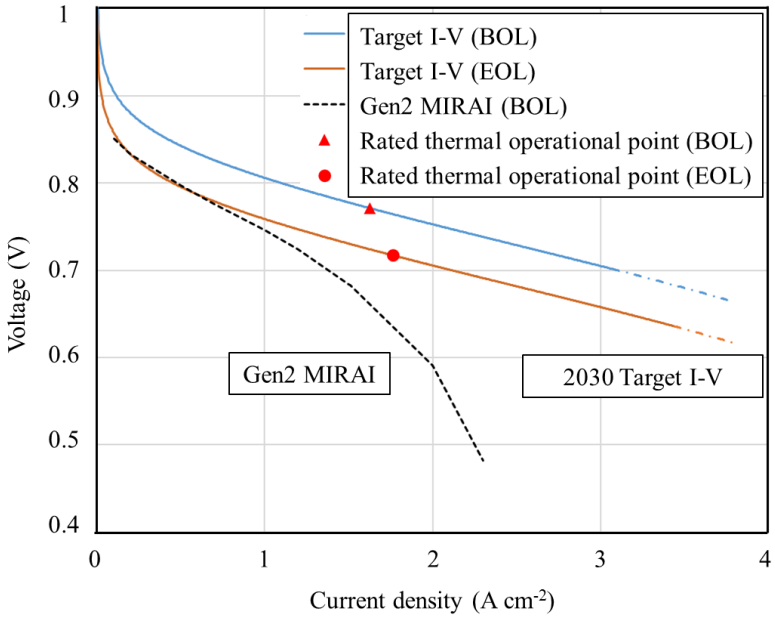

Figure 1.13 The NEDO future target of the characteristics of I-V curves [86].

Therefore, reaching these targets necessitates the development of mass production process technologies, with a critical approach being the reduction of GDL area through increased power density. NEDO has emphasized the significance of prioritizing R_p over R_{np} throughout its research and development endeavors. The focal point is to decrease the R_{O2} and achieve a target molecular diffusion resistance R_p lower than 18 s m^{-1} under 100 kPa abs, 80%RH with a cell temperature of 80°C for GDL by 2030. Based on the target established, the developed MPL coated GDLs were tested to obtain the resistance values for evaluation and comparison with these targets.

1.3 The MPL Modification to Enhance PEFC Performance

Having identified the positive function of the MPL, the next step involves the development of MPL coated GDL with enhanced performance. The goal is to improve water management for increased power output and reduced resistance to oxygen transport. Various modifications are detailed below to achieve these objectives.

1.3.1 The Hydrophobicity Modification

The most straightforward way to enhance performance is by adjusting the hydrophobic component in the microporous layer. This alteration influences the contact angle and, in turn, impacts the capillary pressure of liquid water. In Figure 1.14(a) and (b), Kitahara et al. summarized that the PEFC performance improves when the amount of PTFE in MPL (average flow pore diameter d_m=1 μm, MPL thickness h_{MPL}=180 μm) was reduced to 5% to minimize water repellency under dry conditions. In contrast, the amount of PTFE in MPL (d_m =3 μm, h_{MPL} =90 μm) was set to 20% to increase water repellency moderately, and flooding will be significantly reduced. However, if the amount of PTFE was too much, the strong hydrophobicity prevented the elimination of liquid water and increased oxygen transport resistance [87].

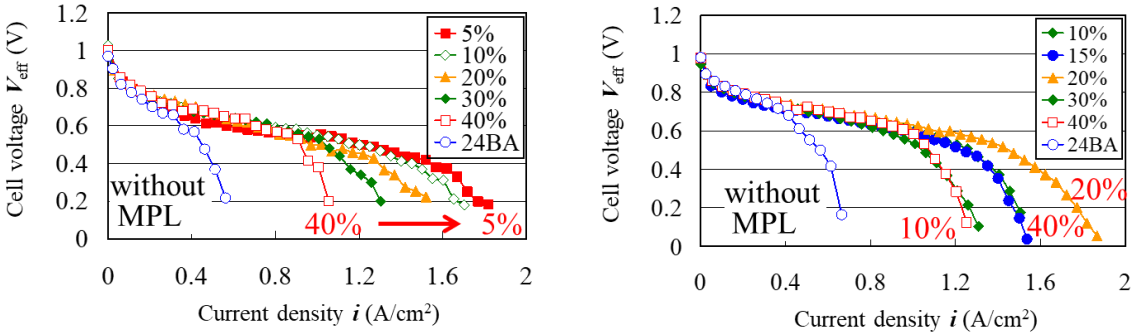

(a) I-V curves of samples with different PTFE content under 0%RH at the cathode.

(b) I-V curves of samples with different PTFE content under 100%RH at the cathode.

Figure 1.14 The I-V curves of hydrophobic MPL coated GDLs with different hydrophobicity and average pore diameters under different humidity conditions [87].

Velayutham et al. found that the carbon cloth-based gas diffusion layer (GDL) attained its highest PEFC performance when the polytetrafluoroethylene (PTFE) content reached 35 wt% [88]. Latorrata et al. proposed the strategy of employing perfluoropolyether (PFPE)

functionalization, which was adopted as an innovative hydrophobic treatment for GDL. Experimental evaluations demonstrated notable advancements when utilizing pure PFPE-based GDLs, which manifested clearly in the overall electrical performance and mitigating diffusive constraints, particularly under high-current density conditions [89]. Öztürk et al. aimed to address water management issues by preparing hydrophobic MPLs using polydimethylsiloxane (PDMS) polymers with different molecular weights and conventional fluoropolymers like PTFE and fluorinated ethylene propylene (FEP). The cell with the lowest carbon-loaded PTFE-MPL demonstrated conceivable performance, while cells with FEP-MPLs yielded unsatisfactory results. PDMS emerged as the most suitable polymer, delivering the best cell performance. The findings emphasized the importance of optimizing the hydrophobic polymer content in the MPL when different hydrophobic materials were used to maintain moderate water management [90,91]. Ong et al. developed an MPL using PVDF as the hydrophobic material. They explored the impact of preparative parameters, including polyvinylidene fluoride (PVDF) concentration, PVDF/electrically conductive filler ratio, and PVDF solvent, on MPL thickness, resistance, and gas permeability. These findings justified the appropriate utilization of PVDF for cell performance improvements [92]. Cho et al. also used PVDF as hydrophobic binder to prepare hydrophobic MPL, and proved the PVDF is suitable for MPL design and improve the water management in the cell [93].

Kitahara et al. aimed to elucidate how MPL design parameters impact PEFC performance. The optimal strategies to improve PEFC performance under low humidity conditions involved reducing the pore diameter of the MPL and PTFE content. Furthermore, it moderately reduced mean pore diameter and kept the PTFE content to 20% under high humidification conditions, effectively preventing flooding. If the amount of PTFE was too much, the strong hydrophobicity prevented the elimination of liquid water and increased oxygen transport resistance. Therefore, the design parameter requirements for the hydrophobic microporous layer are different under different humidity conditions [86]. Wong et al. reported the same situation. They thoroughly investigated the impact of PTFE in standalone MPLs on mass transport and membrane hydration. They highlighted a crucial tradeoff when augmenting the PTFE content within the MPL. Specifically, a higher PTFE content resulted in an increased accumulation of liquid water near the catalyst layer. While beneficial for enhancing membrane

hydration and proton conductivity, this phenomenon also led to a notable rise in mass transport resistance [94]. Can et al. introduced a novel approach by incorporating superhydrophobic fluorinated carbon powder into the MPL to reduce the required PTFE content. The integration of fluorinated carbon led to a notable increase in the water contact angle of the MPL, elevating it from 131° to 151°. Additionally, the MPL with fluorinated carbon exhibited reduced oxygen transport resistance, particularly under high humidity conditions [95]. Weng et al. explored the effects of integrating an MPL with a hydrophobic gradient design on PEFC performance. This configuration facilitated enhanced water retention within the membrane, ensuring efficient humidification and subsequently amplifying cell performance, particularly under low RH conditions. Under high RH conditions, the gradient MPL demonstrated proficiency in effectively expelling water from the electrode but also led to degraded mass transfer, which reminded us that balanced gas-liquid transport must be considered during the MPL design [96].

Thus, the hydrophobic MPL could not always provide favorable water management to enhance PEFC performance with the different humidity conditions because of the relatively weak robustness to the humidity variation [28,85,97]. To achieve further performance enhancement, researchers first developed varieties of hydrophobic MPLs by modifying the geometry parameters in hydrophobic MPLs through special treatment to create more pathways for water expelled from the interface between the catalyst layer and MPL.

1.3.2 The Porosity and Pore Size Distribution

In addition to changing the hydrophilicity and hydrophobicity of the MPL coated GDL, the pore size distribution (PSD) and porosity modifications are the primary and essential methods to influence the water management manner of the MPL coated GDL. The porosity and pore size distribution are intrinsically linked to factors like slurry viscosity, coating thickness, and drying process, each with potential variations [98,99]. The MPL coating applied to the GDL is a practical means to modify porosity and pore size distribution. This technique creates significantly different porous structures within the microporous and gas diffusion layers, resulting in porosity and pore size gradients that enhance overall performance.

Kitahara et al. found that the influence of the MPL mean pore diameter is shown in Figure 1.15(a) and (b). The dry-up robustness is improved by reducing the d_m of MPL (h_{MPL} =110 μm, PTFE content 20%) from 10 to 1μm and reducing the air permeability in the thickness direction. Reducing the average flow pore diameter d_m of MPL from 10 to 3 μm significantly improves the flooding resistance. However, the power generation performance will decrease if the d_m is too small [86]. Zhan and their team explained the theory. They found that in uniform porosity GDLs, gas diffusion increases with rising porosity and decreasing contact angle, and it also improves with thinner GDL thickness. In contrast, GDLs with MPL exhibit more robust gas diffusion with larger MPL porosity and thinner MPL thickness. When dealing with gradient porosity GDLs with equivalent average porosity, the gas diffusion is more favorable with a steeper porosity gradient [100]. Chun et al. investigated the pore size distribution of the MPL by using the self-made GDL. They carefully controlled the pore size distribution by applying pore-forming agents under different drying conditions. They found that the high drying temperature brought more macro pores but fewer micro pores in MPL than in low-temperature drying and proposed that the optimum pore size distribution of the MPL depended on the cell operation humidification conditions [101]. Simon et al. fabricated hydrophobic MPL with larger pores using a thermally decomposable polymeric pore-former with a specific particle diameter. When liquid water entered the MPL, these larger hydrophobic pores reduced the capillary pressure, so liquid water could only be transported through these large pores. Instead, oxygen transport occurred in the small pores defined by the carbon black structure. They

demonstrated that the gas-liquid transport balance could be maintained by constructing separate liquid water transport channels and gas transport channels by creating pore structures with different characteristics in the same MPL [34]. Athanasaki et al. employed polyethylene glycol (PEG) as a pore-forming agent to produce GDL samples with MPL devoid of cracks. They examined that enlarged pore volume in the hydrophobic MPL could significantly enhance water management from 60%RH to 100%RH conditions [102]. Kartouzian et al. reported similar findings by testing MPLs with distinct porosity distributions. The results suggested that introducing micropores into the MPL structure facilitated the removal of excess water through these pores, thereby allowing smaller pores to remain accessible for reaction gases [103]. Lin et al. prepared an innovative GDL that combined the acetylene black carbon and Vulcan XC-72, resulting in a well-balanced pore structure that enhanced the efficient transport of reaction gases and liquid water [104]. Tanuma et al. experimented with crafting hydrophilic MPLs with varying pore volumes, employing a selection of carbon materials [105]. They meticulously examined mass transfer loss at a high current density of 2.0 A/cm² to indicate water flooding within the cathode catalyst layer. The observed relationship between mass transfer loss and MPL pore volume was apparent. Notably, it became evident that as the MPL pore volume increased, the mass transfer loss decreased proportionally. This outcome underscores the profound impact of MPL pore volume on the performance of the MEA. It highlights that hydrophilic MPLs endowed with larger pore volumes are influential in mitigating water flooding within the cathode catalyst layer.

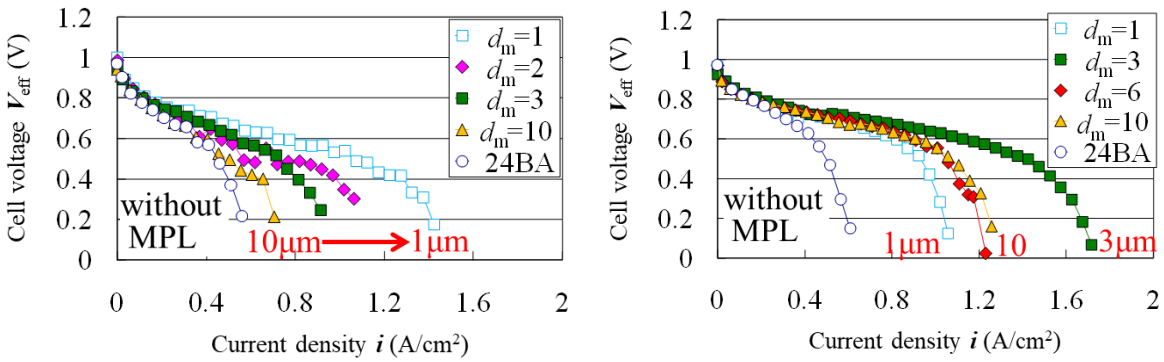

(a) I-V curves of samples with different average pore diameters under 0%RH at the cathode.

(b) I-V curves of samples with different average pore diameters under 100%RH at the cathode.

Figure 1.15 The I-V curves from hydrophobic MPL coated GDLs with different mean pore diameters [87].

1.3.3 The Gradient Pore Structure

The pore gradient can also contribute to the performance variation except for the porosity and pore size distribution modifications. Benefiting from the layers configuration of the MPL coated GDL, it is easy to control the pore size of each layer by a unique fabrication method and to utilize the pore former. Figure 1.16, discussed by Tang et al., reported that the graded pore diameter can create a difference in capillary forces according to Eq. (1.14) [106]. The comparative study examined fuel cells that incorporated MPLs with graded pores (GMPLs) and those using conventional uniform MPLs. The results indicate that GMPL-equipped fuel cells outperform their counterparts with uniform MPLs, especially under high current densities. A micro-porous layer with graded porosity significantly enhances the fuel cell reaction process. This improvement is likely due to the more effective transport of liquid water through the larger pores and the efficient diffusion of gases through the smaller pores in the GMPLs. This positive effect can be attributed to the increased capillary force generated by the porosity gradient in the MPL, consequently boosting the electrode water expulsion capacity.

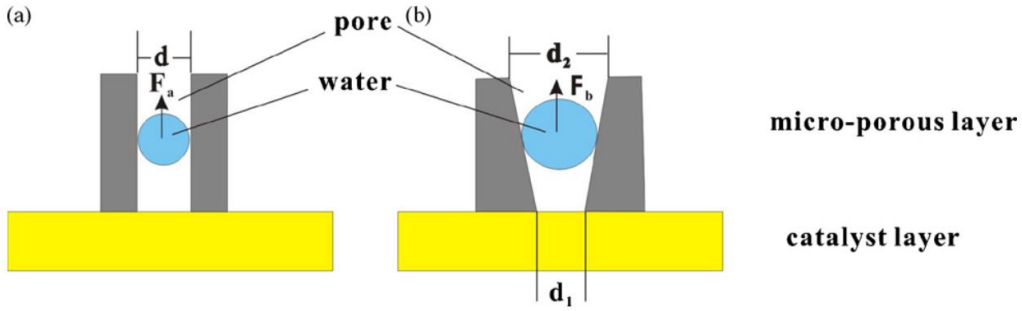

Figure 1.16 Two different pore structures of MPL: (a) Straight pore shape and (b) graded pore structure [106].

Lin et al. demonstrated a consistent water-expelling tendency, establishing that the pressure difference is the primary driving force for water removal [107]. They established three pore structural models based on the MPL coated GDL, one without gradient and two with gradient porosity, denoted as G-P-1 and G-P-2. In the case of G-P-1, where a large pore is situated near the CL and a small pore is near the substrate, the capillary pressure tendency opposes water removal. This is illustrated in Figure 1.17, where the high-pressure region extends to the middle of the channel, limiting the fluid velocity at the CL-MPL interface. Consequently, the MEA containing G-P-1 exhibits a higher mass transfer resistance than the MEA containing G-P-2,

as observed in the polarization curves. In contrast, for G-P-2, the capillary pressure tendency and water removal align in the same direction. The high-pressure region is confined to the inlet of the channel, facilitating accelerated interfacial water removal. Additionally, when compared to G-H-1 and G-H-2, the gradient-porous structure of G-P-2 offers more channels for rapid gas permeation in dry conditions and directional capillary pressure for swift water removal in wet conditions. As a result, the G-P-2 system proves to be optimal for high-performance MEA across varying humidity conditions.

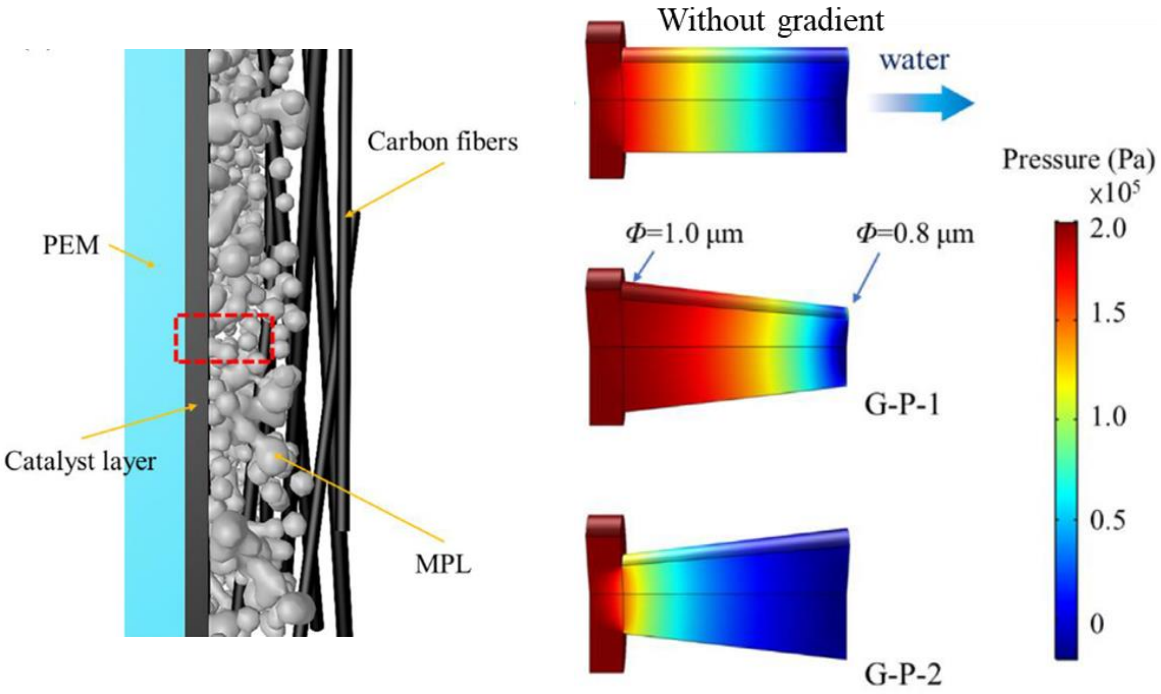

(a) Schematic of different pore structures. (b) Pressure distribution in the model.

Figure 1.17 The (a) schematic of different pore structures and (b) pressure distribution in the model [107].

Li et al. engineered GDLs that incorporated graded pores skillfully tailored with the pore-forming agent $CaCO_3$. Their investigation uncovered an intriguing trend: as the GDL thickness decreased, there was an initial increase, followed by a subsequent decrease in pores falling within the size range of 20 to 100 μm and 7 to 20 μm. The insights highlighted that the fuel cell with a 240 μm-thick GDL experienced minimal voltage loss and exhibited reduced material transmission impedance by establishing the remarkable capacity to bolster the water transfer capabilities [108]. Ko et al. discovered that GDLs with a moderate pore gradient perform better under various relative humidity (RH) conditions [109]. This performance variation is closely linked to water distribution analysis, quantified through X-ray visualization. Significantly, the

pore gradient GDL reduces water content, mitigating concentration overpotential and enhancing performance in high RH conditions. However, under low relative humidity, reduced liquid water content leads to membrane dehydration, resulting in decreased performance, especially with GDLs featuring a high pore gradient. Notably, the highest version is not necessarily associated with the most significant pore gradient, and the impact of the pore gradient becomes more pronounced when ample water is available. Zhao and their team embarked on developing a two-stage MPL characterized by a gradient pore size structure [110]. This inventive MPL was crafted using hydrophobic PTFE, the pore-forming agent $NaHCO_3$, and a conductive carbon black material. Their research illuminated that adjusting the proportions of the pore-forming agent in the MPL to modulate porosity and pore size distribution resulted in an enhanced capillary pressure difference within the GDL. By incorporating varying ratios of pore-forming agents, they increased the number of 7–20 μm pore sizes to facilitate air transmission and introduced 20–50 μm pore sizes to enhance water management within the GDL. Oh et al. innovatively created a gradient in pore sizes by constructing a dual-layered substrate using carbon fibers of varying lengths [111]. Detailed SEM and Hg porosimetry examinations revealed an intriguing pattern: smaller macro pores clustered near the MPL, while larger macro pores predominated closer to the substrate surface. This transformative structural adjustment heightened steady-state performance and magnified transient response and voltage stability within PEFCs, regardless of prevailing humidity conditions. This favorable outcome can be attributed to the dual roles played by the smaller macro pores, which enhance water retention within the membrane, and the larger macro pores, which simultaneously facilitate efficient water removal through the channels. Furthermore, the introduction of the pore size gradient structure positively impacted the bending stiffness of the GDL, underscoring its potential to enhance the durability of PEMFCs.

1.3.4 The Self-Standing Design

Besides the conventional MPL applied to GDLs, researchers are also exploring self-standing microporous layers as an alternative approach. Standing-free MPL has the potential to significantly mitigate ohmic overpotential and high thermal conduct arising from substrate thickness because the standing-free MPL can be produced in a very thin thickness.

Kim et al. researched using an MWCNTs sheet as an MPL in PEFC. The investigation revealed that the cell incorporating a 15-mm-thick CNT sheet MPL exhibited significantly enhanced electrochemical performance, surpassing conventional MPL coated GDL [112]. Electrochemical impedance analyses indicated that the CNT sheet MPL effectively reduced charge transfer resistance, enhancing reaction kinetics and mass transport within the MPL. Ito et al. investigated the intrinsic influence of standing-free MPL properties on PEFC performance in Figure 1.18 [113]. Cell performance tests demonstrated that the self-supporting MPL notably performs better than conventional MPLs. They believed the low thermal conductivity of the standing-free MPL led to elevated temperatures within the GDL.

Consequently, vapor diffusion became the dominant mechanism for transporting product water through the MPL. Chen-Yang et al. designed a series of PTFE/carbon black composite-based single-layer standing-free MPL, successfully prepared from carbon black and un-sintered PTFE [114]. This novel MPL indicated that the PTFE resins were homogeneously dispersed in the carbon black matrix and exhibited good mechanical properties, high gas permeability, and sufficient water repellency. Duan et al. employed a carbon nanofiber sheet (CNFS) produced through electrospinning, stabilization, and subsequent carbonization procedures [115]. The SEM images in Figure 1.19 revealed that the CNFS consisted of interwoven nanofibers measuring 400 to 700 nm in diameter, displaying exceptional electrical conductivity and hydrophobic properties. When utilized as an MPL coated GDL, the CNFS-enhanced GDL exhibited superior gas permeability and achieved higher peak power density than a cathode GDL incorporating a traditional MPL under identical test conditions. Cho et al. also introduced an approach by fabricating self-standing microporous layers (SSMPLs) that integrated PVDF as a binder [93]. Their investigation encompassed the underlying mechanism that elevated the performance of PEFCs by implementing PVDF-bound SSMPL. Moreover,

the study provided valuable insights into the water transport mechanism across each MPL, contributing to a deeper understanding of their functionality.

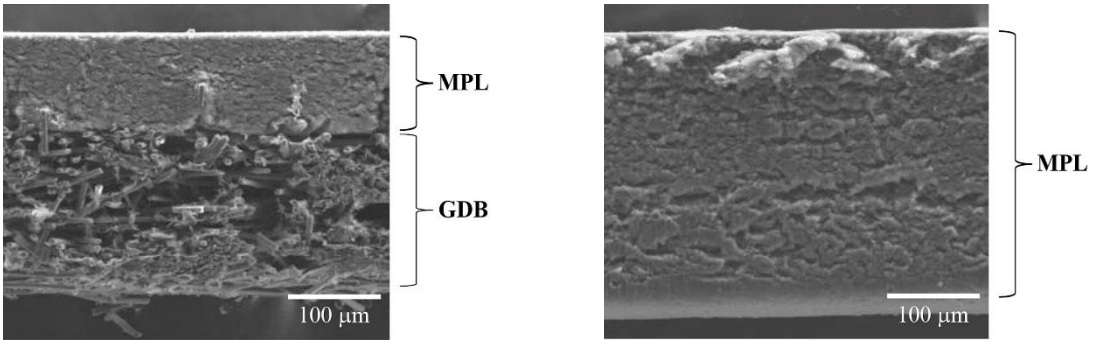

(a) GDL with MPL (b) MPL

Figure 1.18 SEM images of cross-sections of GDL samples: (a) GDL with MPL, (b) MPL [113].

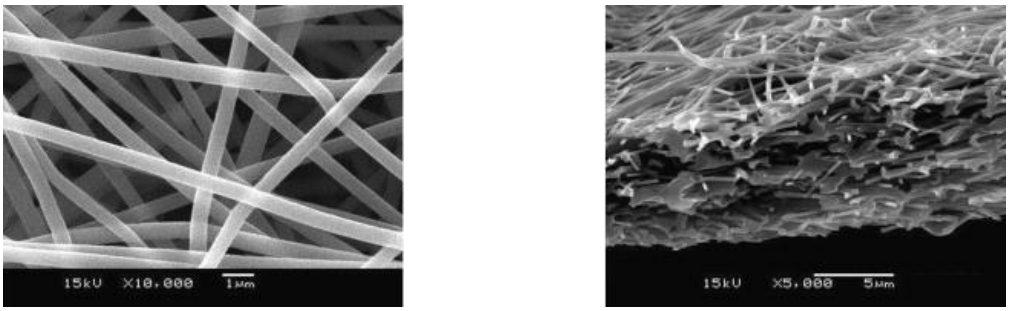

(a) Surface of a CNFS (b) Cross-section of a CNFS

Figure 1.19 SEM images of the surface (a) and cross-section (b) of a CNFS [115].

1.3.5 The Hydrophilic Materials Introduction

Although the hydrophobic MPL coated GDL can meet the demands for regulating the water content from normal to humid conditions, it cannot further improve cell performance by enhancing water management. From the analysis of hydrophobic samples, it can be known that reducing p_c can effectively reduce the difficulty of liquid water passing through the gas diffusion medium.

Therefore, adding hydrophilic materials to the microporous layer is feasible [37,53,85]. Researchers developed varieties of novel hydrophilic MPLs to enhance performance by adding hydrophilic materials or special treatments to create more pathways for water expelled from the interface between the catalyst layer and MPL. Inserting hydrophilic materials directly into hydrophobic MPL coated GDLs can solve the management needs of liquid water under different humidity conditions, in which the incorporated hydrophilic region can be the liquid water pathways under high humidity and retain water when in dry conditions.

Spernjak investigated two variations of MPLs, one featuring 30μm hydrophilic aluminosilicate fibers and the other incorporating multi-walled carbon nanotubes (MWCNTs) with a domain size of 5μm. These MPLs resided in their capacity to optimize removing liquid water from the cathode catalyst layer [116]. Kitahara et al. developed a new hydrophilic and hydrophobic double MPL coated GDL to improve the water introduction into the hydrophobic layer, as shown in Figure 1.20 [117,118]. Additionally, a hydrophobic MPL coated GDL containing hydrophilic carbon nanotubes (CNTs) was also designed, in which the hydrophilic CNTs worked as the hydrophilic water transport channels to enhance liquid water expelling from the CL, as shown in Figure 1.21, the excellent gas-liquid transport balance achieved PEFC performance improvement regardless of the humidity conditions [119]. They proved that the multiple layers of MPLs effectively decreased the oxygen transport resistance under low and high humidity conditions because the top hydrophilic layer effectively expelled water from the catalyst layer [120].

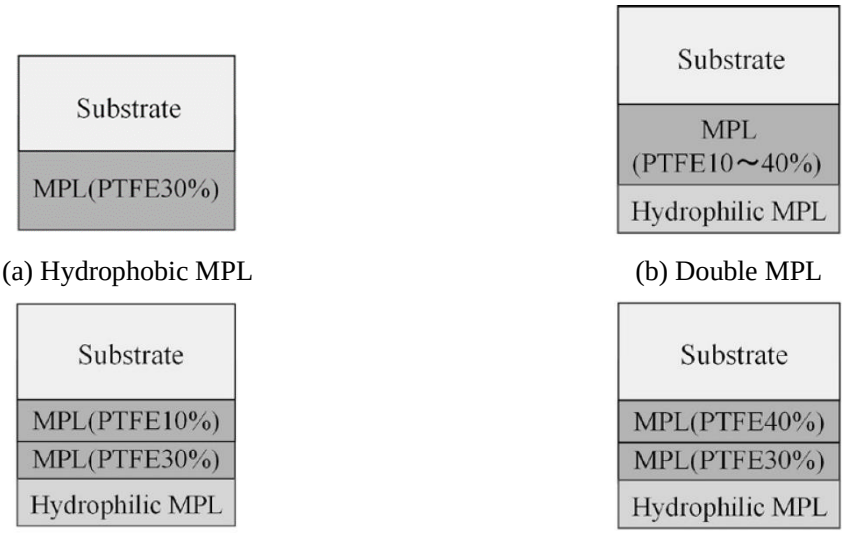

(a) Hydrophobic MPL

(b) Double MPL

(c) Triple MPL

Figure 1.20 The schematic diagram of double MPL and triple MPL coated GDLs [117].

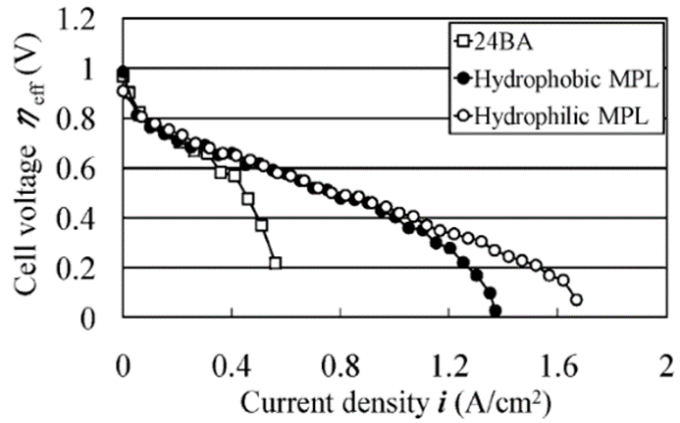

(a) Hydrophobic MPL and hydrophilic double MPL influence PEFC performance.

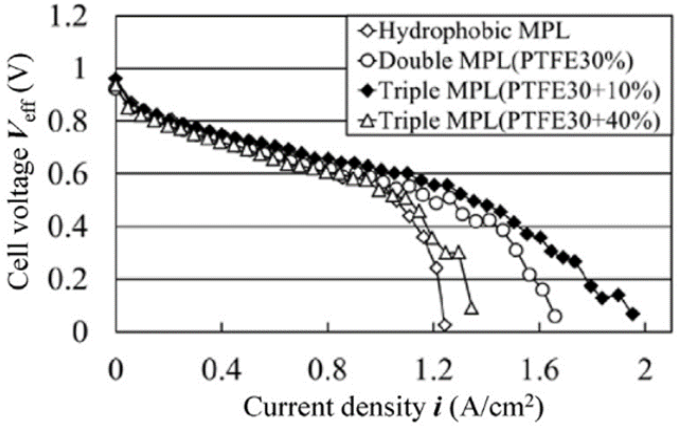

(b) Hydrophobic MPL, hydrophilic double MPL, and hydrophilic triple MPL influence PEFC performance.

Figure 1.21 The influence of (a) hydrophobic MPL and hydrophilic double MPL, (b) hydrophilic double MPL and hydrophilic triple MPL on PEFC performance [117].

Ahn et al. demonstrated that regulating the hydrophilicity of the MPL has a beneficial effect on water management in a PEFC [121]. The hydrophilic MPL exhibits a more robust capacity for excess liquid absorption from the catalyst layer than the hydrophobic MPL, which enhances the accessibility of oxygen to the active sites as an excess liquid near the catalyst agglomerates is rapidly expelled. Tanuma et al. studied the hydrophobicity and hydrophilicity of GDLs in water management characteristics and concluded that the hydrophilic MPL was suitable for preventing flooding [122,123]. Excellent performance was shown under dry and wet conditions when utilizing hydrophilic MPL [124]. They also designed a double MPL coated GDL composed of carbon fiber and a hydrophilic polymer, as shown in Figure 1.22(a). This double MPL presented different properties in different layers, which exhibited excellent performance under high and low humidity conditions. However, Simon et al. found that compared to hydrophobic MPL, purely hydrophilic MPL exhibited performance degradation due to the high water saturation. They prepared the MPL of different acetylene black and vapor-grown carbon fiber (VGCF) ratios with hydrophobic PTFE or hydrophilic perfluorosulfonic acid (PFSA) ionomer binders were studied. Liquid water invaded all pores indiscriminately in the pure hydrophilic MPL, occupying gas transmission paths and destroying the gas-liquid transport balance [125]. Therefore, the distribution and configuration of hydrophilic materials in the MPL should be carefully handled to avoid the diffusion of hydrophilic properties into all pore structures, causing an overall reduction of capillary forces and high water saturation. Schweiss et al. also introduced a strategy for enhancing PEFC performance at high current densities by incorporating hydrophilic wicking agents into the cathode MPL, as shown in Figure 1.22(b), which the observed positive effect could be attributed to improved removal of liquid water through the locally controlled placement of hydrophilic patterns in the MPL [126]. Wang et al. undertook a novel MPL with planar-distributed wettability, in which hydrophilic and hydrophobic rows were arrayed alternately in the in-plane direction but did not achieve further performance enhancement under relatively high humidity conditions, as shown in Figure 1.22(c) [127].

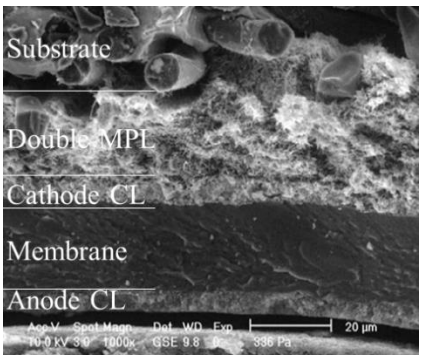

(a) Double MPL coated GDL.

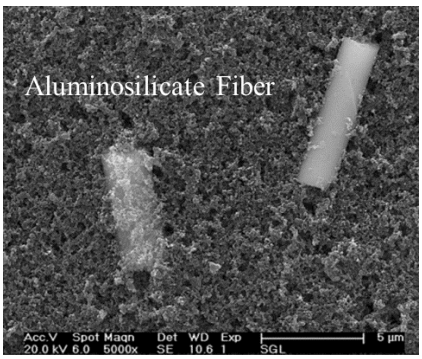

(b) MPL incorporates hydrophilic wicking agents.

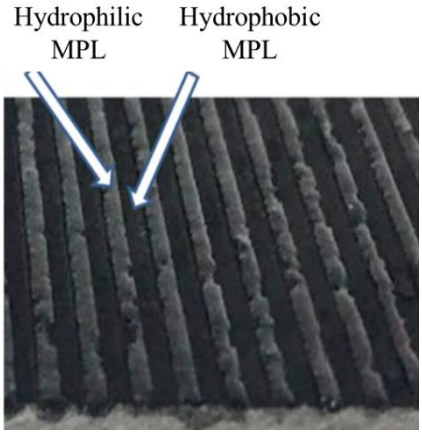

(c) Alternated hydrophilic and hydrophobic MPLs in the in-plane direction.

Figure 1.22 The different treatments to create water pathways in the MPL coated GDLs: (a) double MPL coated GDL [124], (b) MPL incorporates hydrophilic wicking agents [126], (c) alternated hydrophilic and hydrophobic MPLs in the in-plane direction [127].

1.3.6 The Perforation Modification

Creating an MPL with varying pore sizes and both hydrophilic and hydrophobic characteristics within the same layer can be challenging solely by manipulating the mud properties and the production process. Consequently, employing laser light and other methods to craft artificial holes with diverse sizes and properties is an ideal solution. Lin et al. observed that perforated cracks serve a dual role through the 3D lattice Boltzmann method (LBM): not only do they decrease capillary resistance and water saturation, but they also encourage the transition of liquid water from capillary fingering to viscous fingering [128]. This transition enhances the permeability of liquid water in the through-plane direction while reducing percolation in the in-plane direction. Furthermore, it is noteworthy that the liquid water within these perforated cracks shows limited sensitivity to the wettability of the MPL.

Manahan et al. used the ytterbium fiber laser to cut PTFE-based bi-layered diffusion media (DM) to create hydrophilic perforated holes with 100 μm diameter. The PTFE in the holes and vicinity area was also burned out to make the hydrophilic zone. These holes and regions brought significant water accumulation in the MPL, as shown in Figure 1.23(a), resulting in local flooding and low performance under highly humid conditions [129]. This sample was compared to the sample with HAZ but without perforations in Figure 1.23(b). Under low humidity and low-to-moderate current densities, the MPL facilitates water back-diffusion from the cathode to the anode. Conversely, as more water is produced or inlet streams approach saturation, the MPL transforms into a barrier, impeding the movement of liquid water. The hydrophilic HAZ was further recognized as a passive humidifier and water redistributor in dry conditions, reducing membrane and CL resistance during polarization testing.

Alink et al. obtained the same conclusion that laser perforation holes led to poor performance. When employing mechanical perforation, measures can be taken to prevent side effects, and experimental techniques show indications of a beneficial drainage effect. Surprisingly, the anticipated improvement in cell performance due to increased oxygen diffusivity resulting from reduced saturation near the holes is not observed. Instead, the limiting factor for oxygen diffusivity appears to be the liquid water in the interface between the catalyst

layer and the MPL. Perforations effectively drain this interfacial water, but exposing the MEA leads to dehydration in drying conditions, as shown in Figure 1.23(c) and (d) [130].

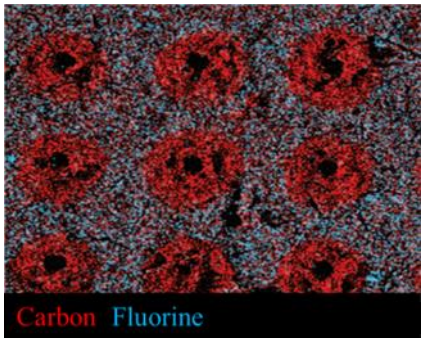

(a) MPL with HAZ and DM perforation.

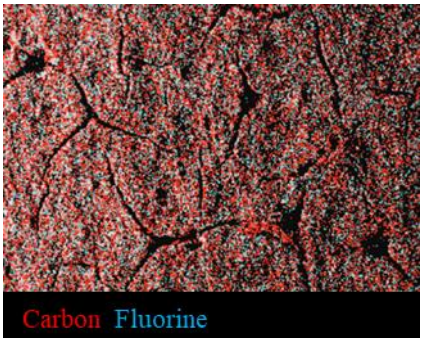

(b) MPL with HAZ but without DM perforation.

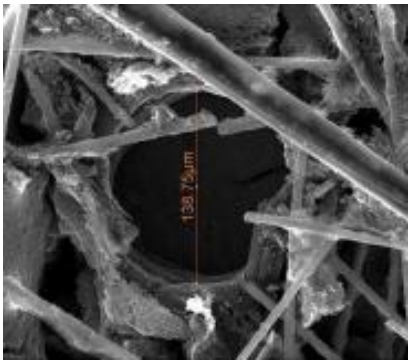

(c) Fiber structure after drilling hole.

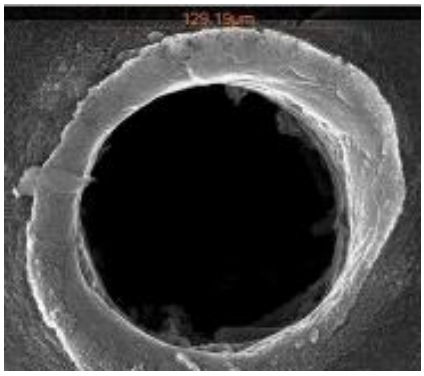

(d) MPL side after drilling hole.

Figure 1.23 The SEM images of the MPL sample after (a) laser perforations with and (b) without DM perforation [129] and (c) machined perforations by drills at the fiber side and (d) MPL side [130].

In summary, establishing separate gas and liquid water transmission channels within the same MPL could enhance performance. One feasible approach was incorporating a hydrophilic pore structure into the hydrophobic MPL coated GDL. The intentionally created hydrophilic pores facilitated the removal of liquid water from the catalyst layer, mitigating flooding effects. The balance between the reduction of oxygen transport and the alleviation of flooding should be adjusted by the configuration form and ratio of hydrophilic and hydrophobic pores to achieve optimal liquid water and oxygen transport within the cell.

1.4 The Water Management Limitation of the Present MPL Coated GDL

While various modifications have demonstrated performance improvements under specific conditions, achieving consistent enhancement remains challenging, particularly under low and high humidities and high current densities, because the MPL coated GDL may not consistently maintain an optimal balance between water and gas diffusion across all conditions. These limitations are evident in both water distribution results from visualization and modeling calculations.

1.4.1 The Water Distribution Observation of MPL Coated GDL in PEFC

Banerjee et al. achieved a comparable result using in-operando synchrotron X-ray radiography [131]. Water saturation was stabilized under high current density conditions in commercial MPL coated GDL (SGL 25BC). Simultaneously, higher current density increased water saturation, accumulating significant liquid water at the CL/MPL interface.

Similarly, Naito and colleagues highlighted this issue, utilizing X-ray imaging to expose flooding in the cathode-side catalyst layer when employing conventional hydrophobic and hydrophilic MPL coated GDLs, as depicted in Figure 1.24 [132]. With increased current density, a large amount of liquid water accumulated under the rib region, and the hydrophobic MPL faced difficulties promptly removing excess produced water, potentially leading to problems like catalyst layer flooding. The flooding can be observed in Figure 1.24(b), in which the water did not appear in the MPL but generated a thin water film at the MPL/CL interface, reducing the efficient diffusion of reactant gases to the catalyst sites. Both water visualizations suggested the same phenomenon: the hydrophobic MPL coated GDL raised the liquid water accumulation at the interface, which prevented oxygen diffusion to the CL.

Meanwhile, due to the introduction of the hydrophilic MPL, the water distribution in the cell is utterly changed by hydrophilicity, as shown in Figure 1.24(c) and (d). Unlikely when applying hydrophobic MPL coated GDL, the liquid water absorbed and accumulated in the hydrophilic MPL, leading to worse oxygen diffusion. Besides, the visualization reveals that liquid water in the MPL becomes apparent after accumulating from the rib surface and reaching the MPL region. This observation suggests that the hydrophilic MPL can also draw liquid water from the substrate side. This result supports the findings from Aoyama et al.. that liquid water

tends to be drawn from the CL and accumulates in hydrophilic MPLs, then evaporates to maintain oxygen transport [133].

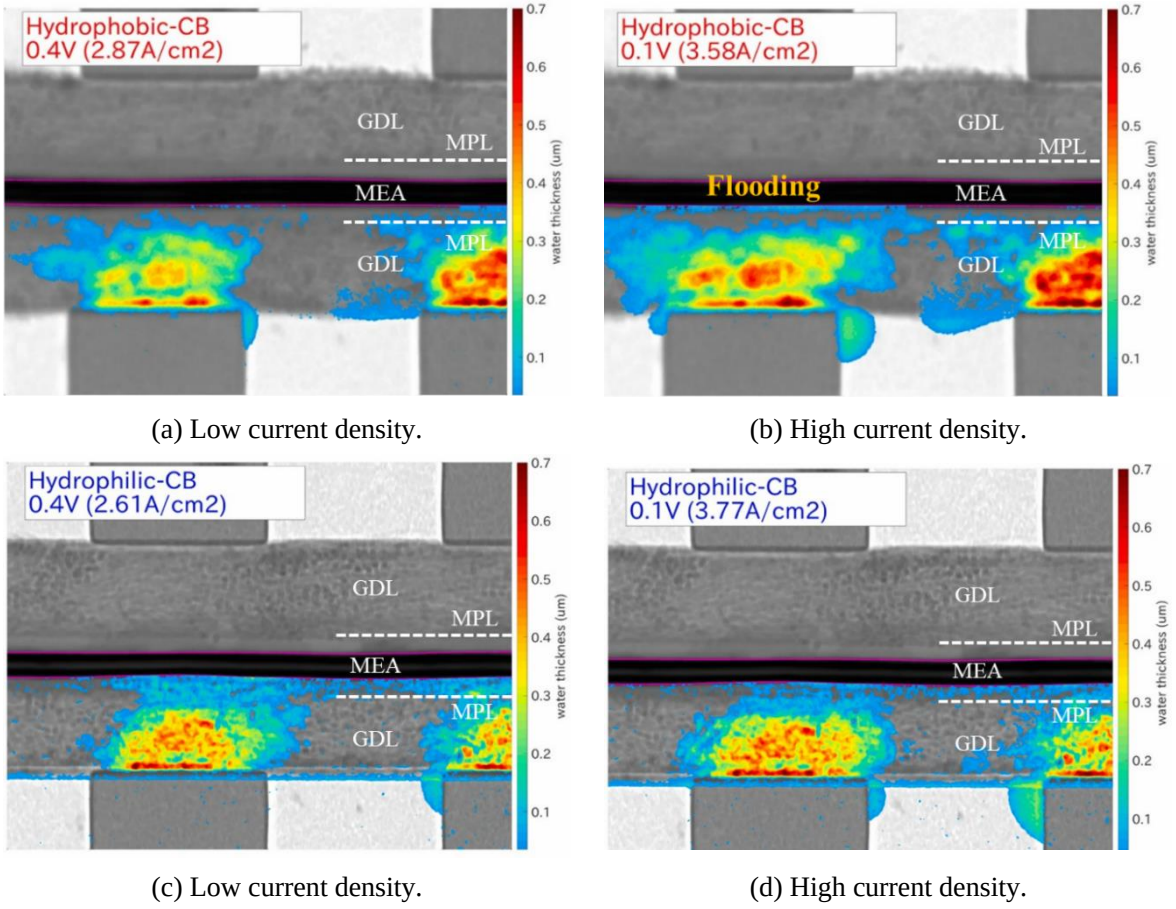

(a) Low current density. (b) High current density.

(c) Low current density. (d) High current density.

Figure 1.24 Liquid water distribution in hydrophilic MPL coated GDL under low and high current density conditions [132].

Shrestha et al. revealed the potential for tailoring the wettability of the GDL to optimize performance under specific conditions without humidification by carefully balancing membrane hydration and oxygen transport [134]. The tri-MPLs consisting of hydrophilic MPL and hydrophobic MPL significantly improved the performance of PEFCs because the hydrophilic MPL resulted in a notable increase in cell potential and was attributed to enhanced membrane hydration but also led to excessive liquid water accumulation at the cathode GDL, subsequently causing an increase in oxygen transport resistance at high current densities under the rib region, as shown in Figure 1.25. The hydrophilic MPL coating, aimed at enhancing membrane hydration, inadvertently increased cathode mass transport resistance and oxygen diffusive time. This phenomenon can be linked to the heightened liquid water saturation within the cathode GDL, subsequently causing a reduction in effective porosity and an increase in the

tortuosity of open pore space. These alterations can potentially impede oxygen transport from the flow field to the reaction sites, ultimately decreasing the effective diffusion coefficient of oxygen within the cathode GDL. Despite these challenges, the study findings underscore that the benefits derived from improved membrane hydration, facilitated by the hydrophilic MPL coating, outweigh the setbacks caused by the obstruction of oxygen transport pathways.

From a broader perspective, careful consideration of hydrophilicity modification is crucial in designing MPLs and GDLs to optimize fuel cell performance, especially in scenarios where external humidification is not employed.

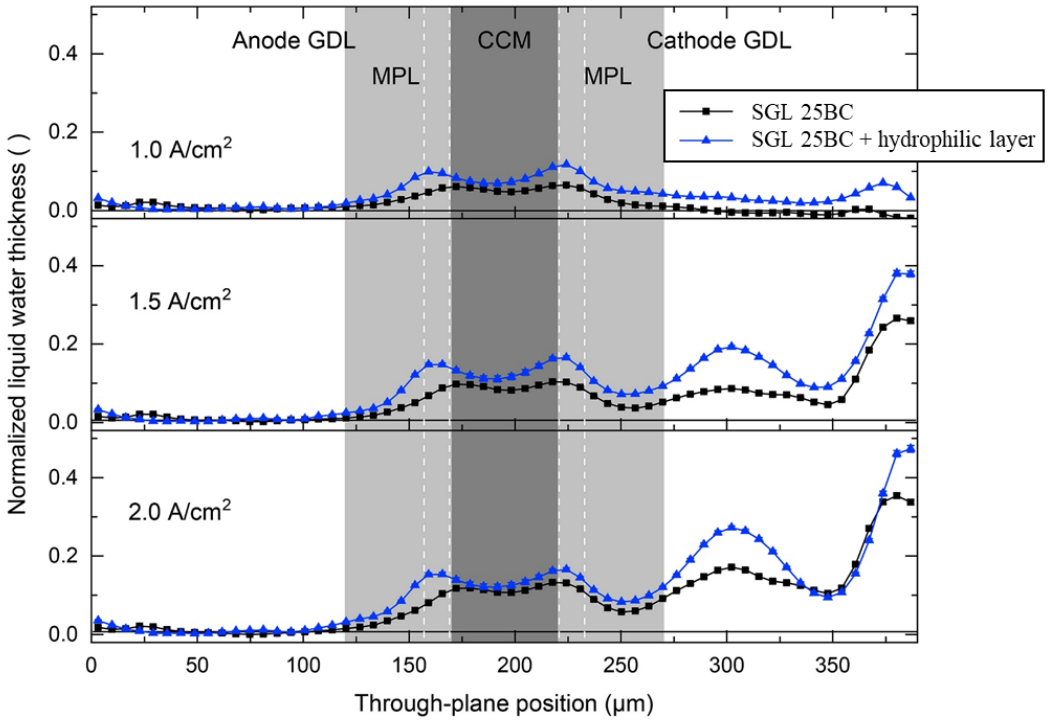

Figure 1.25 The liquid water thickness profile along the through-plane direction under the rib region [134].

1.4.2 The Water Distribution Simulation of MPL Coated GDL in PEFC

Except for water visualization, the model simulation also illustrates the water distribution of the MPL coated GDL. Hou et al. utilized Eq.(1.14) to present simulation results indicating that a pronounced hydrophobicity results in elevated local p_c [135]. The strong hydrophobicity impeded water transport, allowing water to permeate MPL under exceptionally high inlet pressure, as illustrated in Figure 1.26(a). A notable portion of water was confined, while the remaining water flowed into the GDL through larger pores with more miniature p_c. Additionally, a high contact angle in the MPL contributed significantly to the increased dry pore fraction, as depicted in Figure 1.26(b). As a result, the robust hydrophobicity gave rise to challenges in the diffusion of liquid water because of the substantial water trapping within the electrode due to the high p_c caused by the increased contact angle.

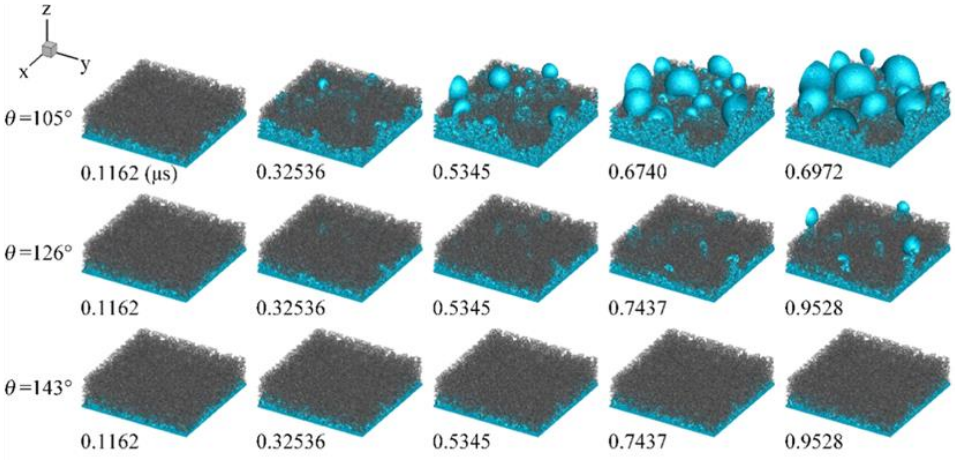

(a) Water transport inside MPL under different hydrophobicity.

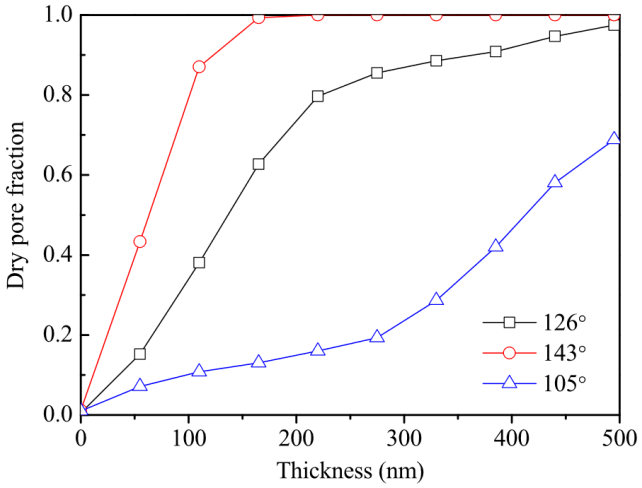

(b) Dry pore fraction along the thickness direction.

Figure 1.26 Simulation of water transport inside MPL under different hydrophobicity (a) illustrations of water transport inside MPL and (b) dry pore fraction along the thickness direction [135].

However, continuing to increase the hydrophobicity of the MPL does not lead to more significant improvements in performance. Based on the simulation from Lin et al., the polarization curves of PEFCs with MPLs of various hydrophilicity are shown in Figure 1.27 [136]. The contact angle of 95° leads to significant concentration loss, resulting in a limited PEFC performance with a small limiting current density under relatively dry conditions. Enhancing the hydrophobicity of MPL proved to be effective in improving PEFC performance. Increasing the contact angle of MPL from 95 to 135° resulted in a remarkable promotion in limiting current density. The improved fuel cell performance was attributed to good oxygen transport by diminished liquid water saturation in the CL, MPL, and GDL. However, further increasing the contact angle cannot significantly increase the limiting current density. Even though their simulation did not mention it, the increased strong hydrophobicity brought water flooding under high humidity conditions [87,92].

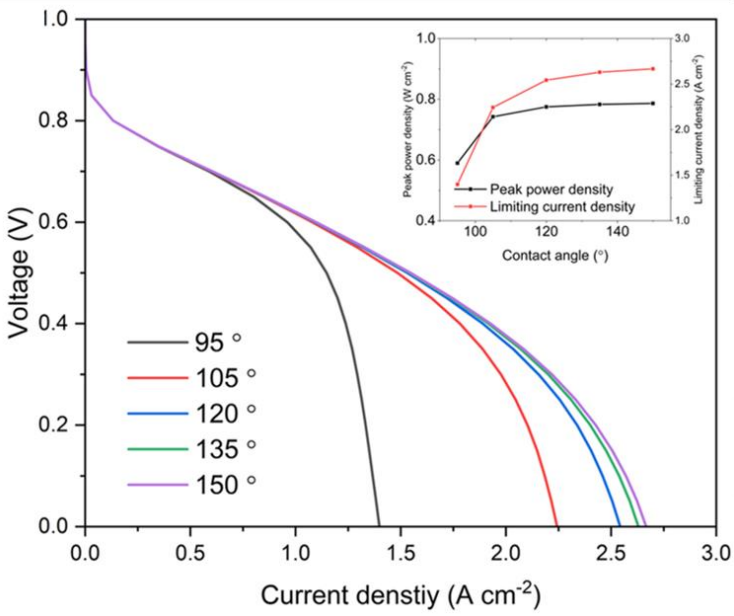

Figure 1.27 Effects of contact angle of MPL on cell performance [136].

From all of the above, researchers have explored enhancing the performance under dry conditions by adjusting the PTFE content and creating a PTFE concentration gradient [137]. However, it is essential to recognize that the hydrophobic MPL may not always provide optimal water management capabilities, especially under high humidity conditions [84]. To address this limitation and improve PEFC performance under low and high humidity conditions,

introducing hydrophilicity into the MPL becomes a pivotal method for lowering the p_c and alleviating flooding.

1.4.3 The Water Distribution of the MPL Coated GDL with Cracks

On the MPL surface, the cracks are usually generated during the MPL slurry drying process and bring large pores, which utterly change the pore distribution and water transport paths. Fishman et al. employed microscale computed tomography to assess the through-plane porosity distributions of MPL coated commercial paper and felt GDLs, specifically using SGL 10BB, SGL 25BC, and SGL 35BC. Analysis of cross-sectional images revealed that cracks were generated and the locations usually aligned with adjacent fiber locations, suggesting an influence of fibers on the occurrence of cracks in the MPL, and the porosity in the central area of the cracked MPL consistently decreased toward the catalyst layer side [138].

Dai et al. delved deep into the liquid water transport within 3D models of non-crack MPL and those with cracks [139]. They unveiled the significantly enhanced flow velocities observed within the cracks and larger interconnected pores. Applying a linear gradient pressure to both sides of the MPL prompted liquid water to coalesce and infiltrate the broad pores on the surfaces of the cracks, establishing a stable reservoir for water storage within these fissures. When maintaining a constant MPL porosity, the non-cracked MPL exhibited higher permeability than the cracked MPL average permeability, which suggested that the larger average pores among the carbon particles facilitated more efficient transport than the interconnected cracked pores.

Sasabe et al. conducted a study to examine the impact of cracks within the MPL on liquid water transport in operational PEFCs [140]. They employed soft X-ray radiography to examine liquid water, as shown visually in Figure 1.28. Their findings revealed that liquid water flowed through cracks in the MPL, while the liquid water was not present in the MPL but accumulated at the interface between the CL and the MPL. This lack of liquid water in the MPL is attributed to its highly hydrophobic nature, which hinders water access to the substrate layer. These results suggest larger pores or cracks in the MPL are conduits for liquid water to reach the substrate layer, while smaller pores facilitate gas transport. Wang et al. initiated the development of an MPL with varying ratios of intersected crack area (RICA) values, explicitly focusing on the presence of intersected cracks, as shown in Figure 1.29 [141]. Their investigation yielded compelling results, showcasing a solid connection between higher RICA

values and increased gas and water permeability within the MPL. A particularly striking observation was the nearly threefold rise in water permeability. Additionally, the current density at the dry-wet boundary exhibited a noteworthy and positive enhancement. These findings robustly underscored the pivotal role of intersected cracks in fortifying gas and water management capabilities.

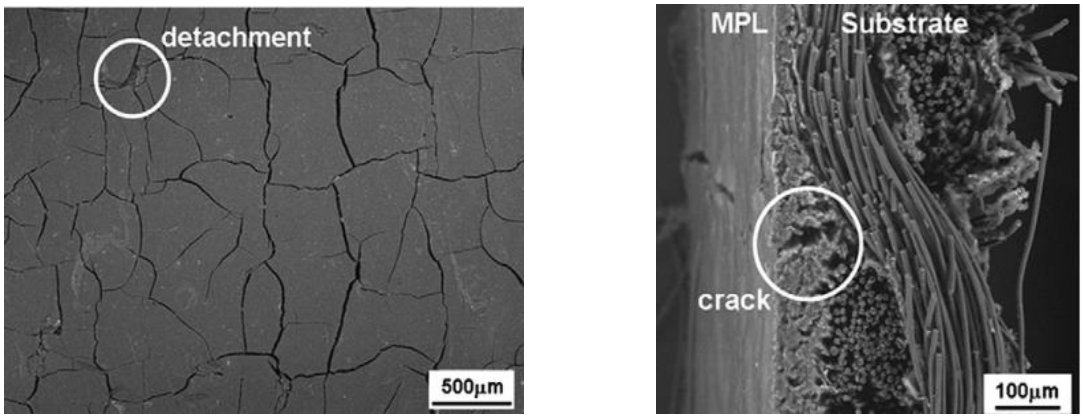

(a) The MPL surface. (b) The cross-sectional image of the GDL.

Figure 1.28 Micro-CT image of (a) the MPL surface and (b) the cross-sectional image of the GDL [140].

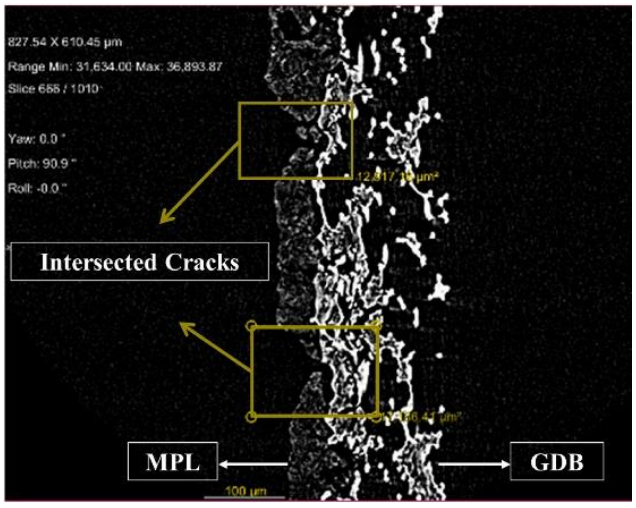

Figure 1.29 Micro-CT cross-section image of MPL with intersected cracks [141].

Niblett et al. employed CFD simulations with a segmented X-ray CT image of Toray material to explore the impact of MPL crack dilation on GDL water cluster formation, as shown in Figure 1.30 [142]. Increased MPL crack dilation led to extensive GDL water flooding, enhancing connected water pathways and in-plane water movement. The presence of an MPL established primary water cluster pathways, absent in GDLs without an MPL, emphasizing the

need to minimize MPL cracking to reduce saturation levels, reducing the effect of local oxygen distribution.

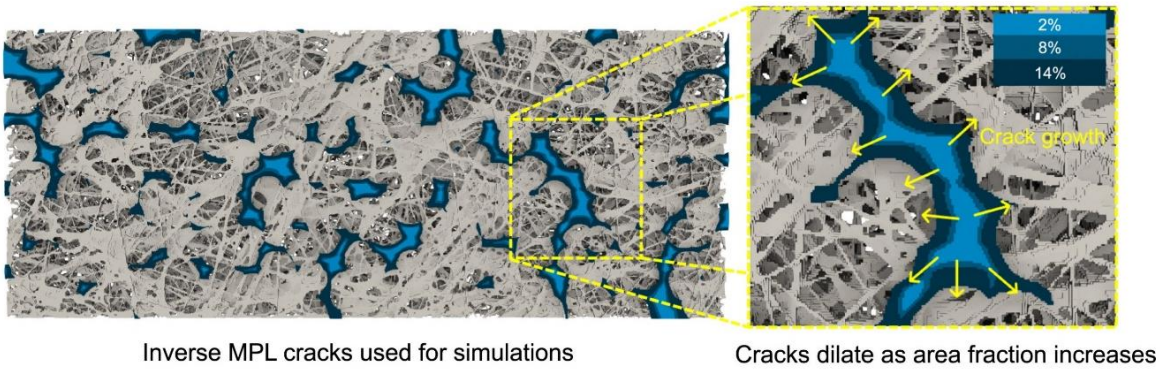

Figure 1.30 GDL microstructure with crack positions and specific crack growth shown from light to dark blue and final MPL crack boundary conditions for water injection into the GDL [142].

1.5 The Design Objectives of MPL Coated GDL

The present commercial hydrophobic MPL-coated GDL always have cracks on the surface, as SGL 39BC is shown in Figure 1.31(a) [143]. As described in the previous section, the cracks cause more severe flooding and water saturation in the MPL coated GDL and deteriorate oxygen diffusion. Besides, a rough surface will also reduce the contact area and cause higher contact resistance. Therefore, preventing crack generation during the preparation process is required for the in-house MPL-coated GDL, and a smooth surface should be created to avoid the above problems, as shown in Figure 1.31(b).

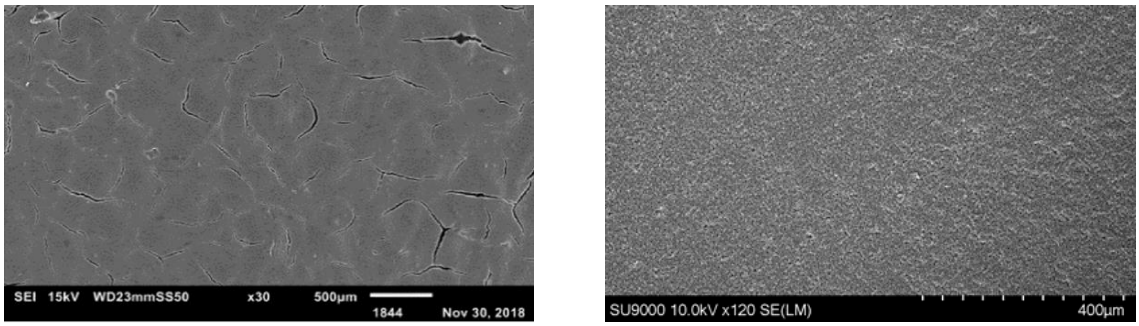

(a) SGL39BC with cracks. (b) In-house hydrophobic MPL without cracks.

Figure 1.31 The SEM photos of the (a) SGL 39BC without cracks [143] and (b) in-house hydrophobic MPL without cracks.

To enhance the output power of PEFC systems and broaden their scope of utilization, it has become increasingly crucial to focus on advancing GDL coated with MPL. From previous sections, the hydrophobic MPL, in Figure 1.32(a), cannot improve its performance due to the flooding always happening under high current density and humid conditions because the hydrophobic MPL cannot afford sufficient water pathways. Introducing hydrophilic structures into the hydrophobic MPL is a feasible solution to create water pathways and guarantee hydrophobic structures as gas pathways, which is an ideal adjustment method for MPL dual-function modification. In summary, incorporating hydrophilicity into the MPL coated GDL results in elevated water saturation within the MPL, primarily due to the low p_c rather than increased water at the CL/MPL interface. The substantial water retention in the hydrophilic MPL, in Figure 1.32(c), protects against MEA dehydration in dry conditions. However, this increased water occupancy comes at a cost: the proportion of empty pores available for oxygen transport diminishes, reducing oxygen diffusion to the CL and consequently negatively

impacting cell performance. Therefore, the hydrophilicity and hydrophobicity combination is changed from the different MPL configurations and utilized materials, so it is important to investigate the appropriate compositions in the novel MPL coated GDLs.

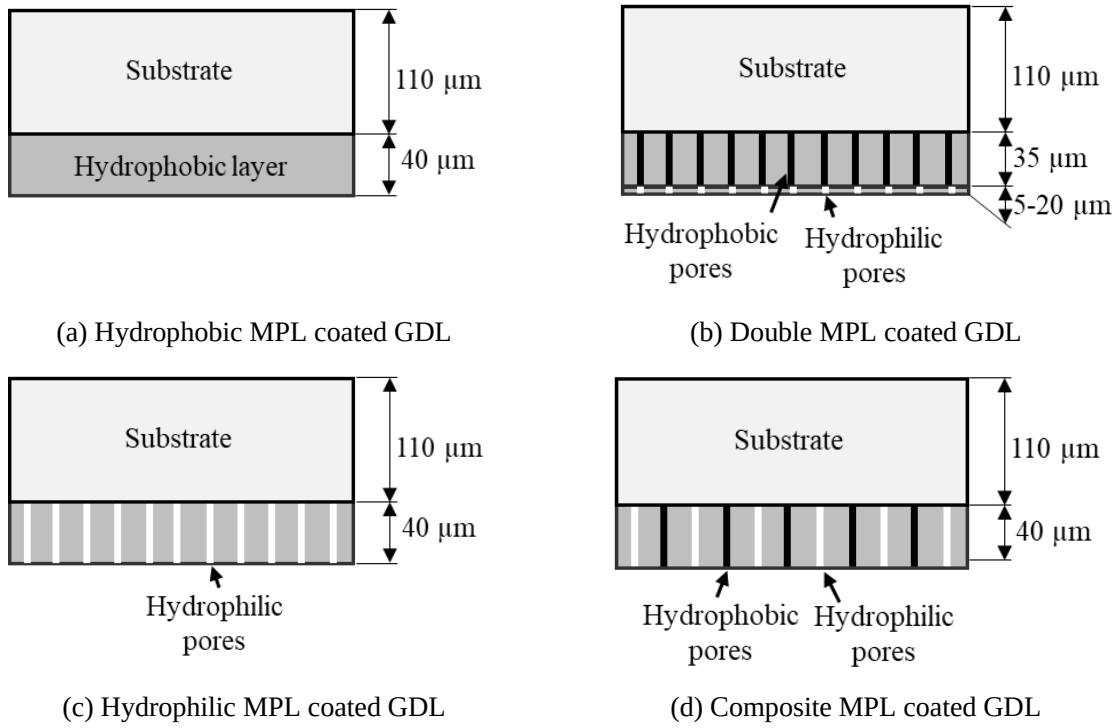

(a) Hydrophobic MPL coated GDL

(b) Double MPL coated GDL

(c) Hydrophilic MPL coated GDL

(d) Composite MPL coated GDL

Figure 1.32 The schematic diagrams of (a) hydrophobic MPL coated GDL, (b) double MPL coated GDL, (c) hydrophilic MPL coated GDL, and(d) composite MPL coated GDL.

While numerous researchers have examined modifications to the MPL by incorporating hydrophilic features, the specific design parameters for optimizing double MPLs to improve PEFC performance have yet to be established in the existing literature. Therefore, this study emphasized enhancing the performance of PEFCs in low and high-humidity environments by introducing a suitable hydrophilic layer into the double MPL coated GDL, as shown in Figure 1.32(b), and revealing the relevant design parameter effects. The effectiveness of MPL in preventing flooding was evaluated by measuring the oxygen transport resistance from the flow channel through the GDL to the catalyst layer using the limiting current density in polarization curves. The improved performance proved that the hydrophilic layer promoted the introduction of liquid water into the hydrophobic pores in the double MPL, enhancing the ability of the MPL to discharge water from the catalyst layer.

Even though the double MPL design reduced the oxygen transport resistance under high humidity conditions, further reduction in the oxygen transport resistance was essential for

enhancing the performance of heavy-duty PEFCs. Thus, a novel composite MPL design that differs from the conventional method of creating an artificially selected hydrophilic area but incorporates hydrophobic and hydrophilic pore structures distributed randomly within the same layer was proposed, as shown in Figure 1.32(d). This enhanced the ability of the MPL to expel excess water at the catalyst layer through hydrophilic pores while maintaining oxygen diffusion pathways by hydrophobic pores. The effects of combinations of hydrophobic and hydrophilic binders used in the composite MPL were evaluated to reduce the oxygen transport resistance under high humidity conditions.

1.6 Structure of Dissertation

This dissertation explores various configurations of MPL coated GDLs to improve cell performance by addressing limitations from liquid water flooding and decreasing oxygen transport resistance to meet the demands of the next generation of MPLs. To understand the MPL design, the causes of flooding were analyzed, and different types of microporous layers were considered, including double MPL and composite MPL. These various MPLs, when combined with different substrates, exhibit distinct performance characteristics.

With the structure of the novel MPL defined, the MPL slurry preparation, slurry coating, sample drying, and sintering processes were designed to produce a crack-free microporous layer for the tests. Subsequent experiments analyzed the properties of MPL samples with different ingredients, comparing their performance with traditional hydrophobic MPL samples to identify the most effective MPL composition.

The double MPL coated GDL research revealed the potential benefits of adding hydrophilicity to MPL for performance enhancement. Initially, a double MPL coated GDL was explored, which featured a hydrophilic layer containing Nafion and TiO_2 coated on a hydrophobic MPL. This hydrophilic layer facilitated the introduction of liquid water into the hydrophobic pores in the double MPL, aiding in water removal from the catalyst layer. Although the double MPL design reduced oxygen transport resistance under low and high humidity conditions compared to the commercial hydrophobic MPL coated GDL and close to the target evaluation standard from NEDO, further reduction was necessary to improve the performance of PEFCs.

Subsequently, a novel composite MPL design was proposed, which deviated from the conventional method of creating a selected hydrophilic area and instead incorporated randomly distributed hydrophobic and hydrophilic pore structures within the same layer. This design improved the ability to expel excess water while maintaining oxygen diffusion pathways in the MPL. The appropriate combination of hydrophobic and hydrophilic binders in the composite MPL reduced oxygen transport resistance under high saturated and normal conditions.

The detailed structure of this dissertation is as follows:

Chapter 1 is the introduction section, revealing the target performance request and the challenge of MPL coated GDL development in improving performance by ameliorating water management. According to various research studies, developing the novel MPL coated GDL is a reasonable solution to building appropriate water management to improve PEFC performance.

Chapter 2 indicates all the experimental methods to evaluate the MPL properties and performance. Different experimental methods were designed for MPL coated GDLs possessed different structures.

Chapter 3 demonstrates an MPL configuration of double MPL coated GDL. The double MPL coated GDL properties were obtained through the SEM images, surface pore and in-pore contact angles, water breakthrough pressure, and water vapor permeance. The best double MPL coated GDL ingredient was evaluated by measuring total oxygen transport resistance. Finally, the oxygen transport resistance separation test was conducted to determine the effect of double MPL coated GDL on alleviating flooding under high saturated conditions (200%RH, T_{cell} =35°C).

Chapter 4 shows a novel design of composite MPL coated GDL. Firstly, the composite MPL coated GDL preparation method was developed, and different MPL preparation methods were evaluated through the water permeability test. Then, the properties of the different candidate material combinations were evaluated by surface contact angles, and the performance tests were finished to determine the most suitable combination. Still, the oxygen transport resistance separation test was conducted to indicate the ability of composite MPL coated GDL to alleviate flooding when applied to high saturated conditions (200%RH, T_{cell} =35°C).

In Chapter 5, the evaluation of oxygen transmission impedance includes normal (80%RH, T_{cell} =80°C) conditions with high temperature and low humidity. A comparative analysis is conducted on the total diffusion resistance, pressure-dependent and pressure-independent transmission impedance of the two novel microporous layers under both high saturated (200%RH, T_{cell} =35°C) and normal conditions, juxtaposed with the performance of the commercial SGL 22BB. Additionally, the pressure-related transmission resistance of the new

microporous layer under normal conditions is compared with the target values set by NEDO, indicating that the new microporous layer satisfies the specified target requirements.

Chapter 6 summarizes each chapter and concludes that the newly developed microporous layer has better water management capabilities under both high saturated and normal conditions and is highly robust to changes in humidity within the cell, thus bringing about low oxygen diffusion resistance and high performance. Finally, the prospective directions for future research and development focus on the self-standing MPL containing composite microporous layers coated carbon mesh with thin thickness.

2. The Experimental and Analytical Methods

2.1 The Surface Contact Angle Measurement

Surface wettability is a physical parameter that reflects the inclination of liquid to interact with a solid material. When a liquid contacts a solid surface, it creates a solid-liquid interface, often displacing another substance (typically a vapor in ambient air experiments). The shape of the resulting liquid droplet is determined by the interplay between cohesive forces among like molecules in the liquid and adhesive forces between the solid and liquid phases. Essentially, a solid surface with a strong affinity for the liquid phase tends to have a larger solid-liquid contact area [144]. Conversely, in the presence of strong, cohesive forces within the liquid, the liquid seeks to minimize its interaction with the solid surface to resist separation between its molecules. To accurately evaluate the surface wettability of the MPL coated GDLs, the sessile droplet contact angle (CA) has become a widely adopted indicator of wettability characteristics. In this method, a liquid water droplet is placed on the surface of interest and allowed to spread, and the CA is determined by capturing the side-view profile of the droplet. Figure 2.1 depicts the CA as the angle between the tangent lines at the solid-liquid and liquid-air interfaces near the three-phase contact line. According to traditional wettability criteria, materials with static CAs less than 90° are considered hydrophilic (attracting water), while those with CAs exceeding 90° are deemed hydrophobic (repelling water). However, the CA accuracy was always influenced by the sample surface roughness, and the measurement is normally conducted with dry samples, so it is unsuitable for all conditions.

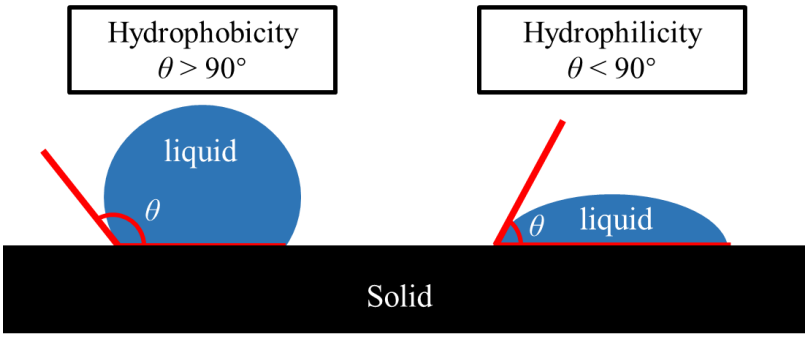

Figure 2.1 Classification of surface wettability based on the contact angle (θ) of a sessile droplet.

2.2 Maximum Pore Diameter

Figure 2.2(a) illustrates the schematic diagram of the test apparatus used to measure the maximum pore diameter d_{max} of MPL coated GDLs. The GDL sample with a diameter of 13 mm was set between cylinder plates and sealing gaskets. To ensure that the sample remains in a state similar to that during the I-V characteristic test after being extruded by the metal plate, a sealing gasket is used to adjust the thickness of the sample after compression. Usually, the thickness of the sample after compression is about 80% of the original thickness. Specimens of different thicknesses were combined with different spacers to achieve fixed compression ratios. This method is followed to adjust the compression ratio in the subsequent assembly of the sample seal.

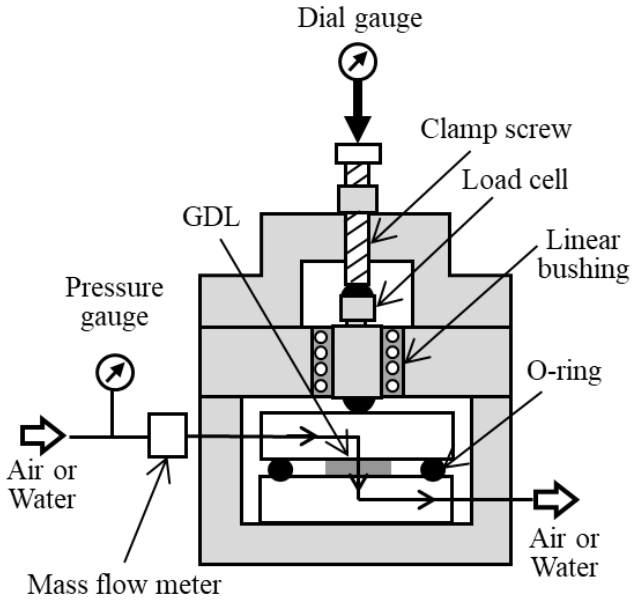

(a) The test apparatus used to measure the maximum pore diameter of the MPL.

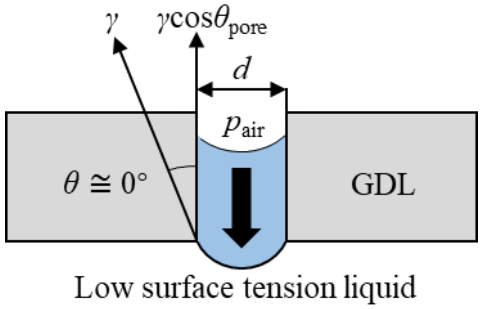

(b) The equilibrium relationship between the low surface tension liquid and the air pressure.

Figure 2.2 The schematic diagram of the (a) test apparatus used to measure the maximum pore diameter of the MPL and (b) the equilibrium relationship between the low surface tension liquid and the air pressure.

According to the ASTM (F316-86) standard test method, the tested sample was immersed in a wetting liquid with low surface tension (0.0159 N m^{-1}) and a contact angle of 0° under vacuum conditions to fill out the pores. The mass flow controller (MFC) regulated the air flow rate and supplied to the sample surface. As the pores were blocked by liquid, the air pressure gradually increased. The minimum air pressure could be obtained when the liquid in the maximum pore was blown out by supplying a through-plane air flow to the saturated sample. The maximum pore diameter d_{max} could be calculated by the following equilibrium relationship in Eq.(2.1) between the liquid surface tension and the air pressure, and the equilibrium relationship is shown in Figure 2.2(b).

$$d_{max} = \frac{-4\gamma \cos \theta_{pore}}{p_c} \cong \frac{4\gamma}{p} \tag{2.1}$$

where d_{max} was the maximum pore diameter, p was the air pressure, γ was the surface tension of wetting liquid (γ=0.0159 N m^{-1}), and θ_{pore} was the in-pore contact angle (θ_{pore} =0°).

2.3 The Water Permeability and Water Breakthrough Pressure Measurement

The water permeability test employed the identical apparatus depicted in Figure 2.2(a), with the distinction that a dry sample was utilized instead of one containing a liquid with low surface tension. This test assesses the liquid water transport capability under varying supply pressures applied to the samples. When liquid water was introduced to the sample surface, penetration was impossible at lower pressures. With the increasing pressure, the point at which water emerges on the lower surface is denoted as the water breakthrough pressure p_{water}, describing the pressure at which water successfully permeates the sample, as shown in Figure 2.3. The water permeability Q_{water} was defined as the Eq. (2.2).

$$Q_{water} = \frac{q_{water}}{A} \tag{2.2}$$

where Q_{water} is the water permeability (cm min^{-1}), q_{water} is the water flow rate (cm^3 min^{-1}), and A is the cross-sectional area of the tested sample (cm^2).

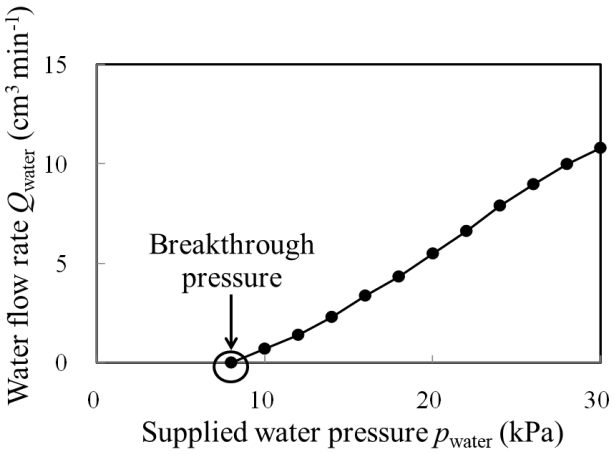

Figure 2.3 The schematic diagram of the equilibrium relationship between the supply water pressure and water permeability.

2.4 The In-pore Contact Angle Measurement

Measuring the CA encounters complexity due to the impact of surface roughness on dry samples, posing a challenge to precisely characterizing material properties in dry conditions. This becomes particularly critical when dealing with substances showcasing distinct behaviors in dry and humid environments. To tackle this issue, an in-pore contact angle measurement θ_{pore} was developed to determine the angle between the solid pore walls and the liquid surface.

After establishing the maximum pore diameter measurement, the θ_{pore} measurement process was initiated, transitioning from air to liquid water on the sample surface. The in-pore contact angle measurement apparatus was the same as the schematic diagram in Figure 2.2(a), where controlled airflow to propel liquid water from a tank through the sample. While assessing the maximum pore diameter, a low surface tension liquid was selectively expelled from the largest pore, with the remaining pores remaining filled. Subsequently, incoming water can only traverse through the largest vacant pore, as shown in Figure 2.4. The water pressure at the appearance of water on the lower side surface was recorded, and the pore diameter was deduced from previous measurements to calculate the contact angle based on Eq. (2.3).

$$p_{water} = \frac{-4\gamma_{water}\cos\theta_{pore}}{d_{max}} \tag{2.3}$$

where p_{water} is the water pressure (equal to capillary pressure) (kPa), water tension γ_{water}=0.0720 N m^{-1}, and the θ_{pore} is the in-pore contact angle with water.

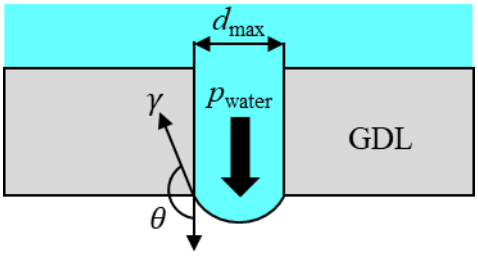

Figure 2.4 The schematic diagram of the equilibrium relationship between the liquid water and the capillary pressure.

2.5 Water Vapor Permeance Measurements

Figure 2.5(a) depicts the water vapor permeance test apparatus. The MPL coated GDL was placed between two stainless steel plates, each plate with a flow channel 1 mm wide, 20 mm long, and 1 mm deep. Dry air and water were supplied to the upper and lower flow channels. Liquid water was supplied from a water tank, where air pressure pushed the water surface and maintained at 2 kPa by a pressure control valve. To prevent liquid water from passing through the MPL coated GDL, the water supply pressure should be lower than the water breakthrough pressure of the MPL. Thus, liquid water could not permeate the MPL coated GDL, allowing only water vapor to reach the upper flow channel. The test was conducted at a constant temperature of 35°C using a water circulation system. The amount of water vapor permeance could be determined from relative humidity (RH) values at the inlet and outlet air measured by dew point meters (Daiichi Kagaku - chilled mirror hygrometers), as shown in Figure 2.5(b). The water vapor mass flow rate varied depending on the difference in the gas-liquid interface in the MPL pores caused by the water supply pressure, pore diameter, and contact angle values of the MPL. Evaluating how much water vapor can diffuse from the lower channel to the upper channel is necessary. Therefore, the water vapor permeance q_{vapor} was defined as the water vapor mass flow rate divided by the flow channel cross-sectional area of the MPL coated GDL as Eq. (2.4). The relationship between the water vapor permeance and air velocity of the hydrophobic MPL coated GDL is shown in Figure 2.6, which the measurement error was less than 5%, and the error bar will not be presented in the comparison of the results to keep the concise image.

$$q_{vapor} = \frac{Q_{vapor}}{A} \tag{2.4}$$

where Q_{vapor} is the water vapor flow rate (mg min^{-1}), q_{vapor} is the water vapor permeance (mg min^{-1} cm^{-2}).

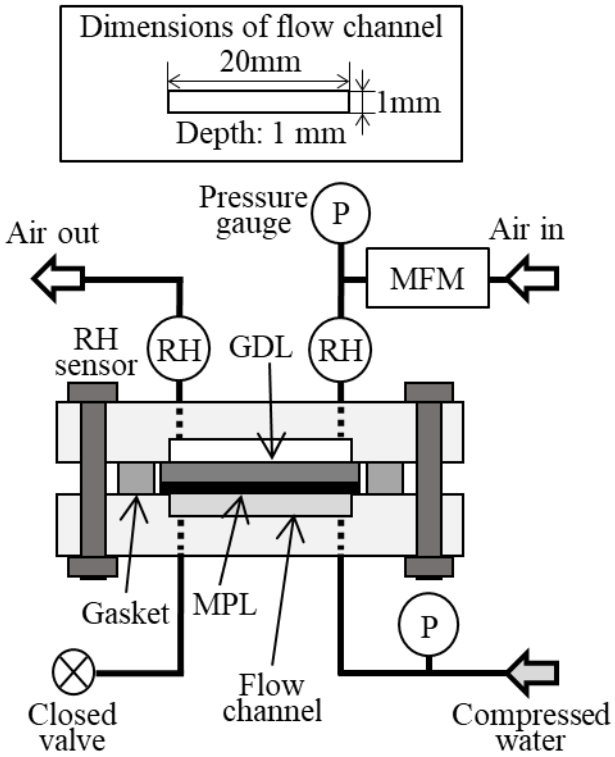

(a) Schematic diagram of vapor permeance test apparatus.

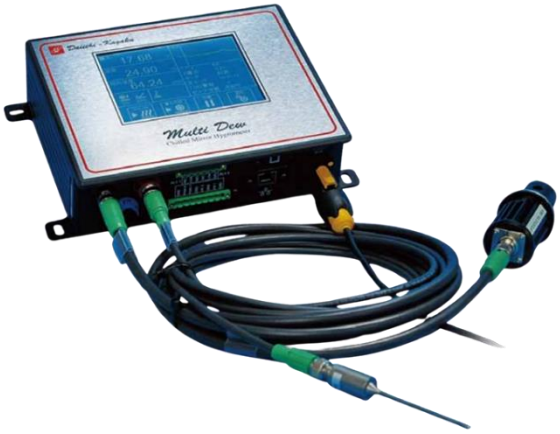

(b) Dew point meters.

Figure 2.5 The (a) schematic diagram of vapor permeance test apparatus and (b) dew point meters.

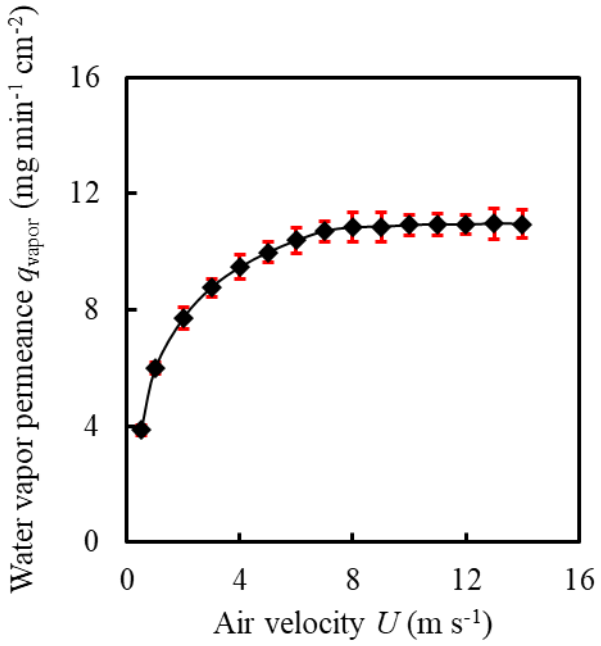

Figure 2.6 The relationship between the water vapor permeance and air velocity of the hydrophobic MPL coated GDL.

2.6 Relative Oxygen Permeance Measurements

Figure 2.7(a) illustrates the schematic diagram of the test apparatus for assessing relative oxygen permeance. The MPL coated GDL was placed between two stainless steel plates with a flow channel measuring 1 mm in width, 20 mm in length, and 1 mm in depth. The temperature was maintained at 35 °C using a cooling water system. The dry air and nitrogen were supplied to the upper and lower flow channels at the same pressure of 1.0 kPa using a differential pressure gauge. The gas chromatography (GC) apparatus (J-SCIENCE LAB, GC7100T) was employed to determine the oxygen permeance from the upper air flow channel to the lower nitrogen flow channel, as shown in Figure 2.7(b).

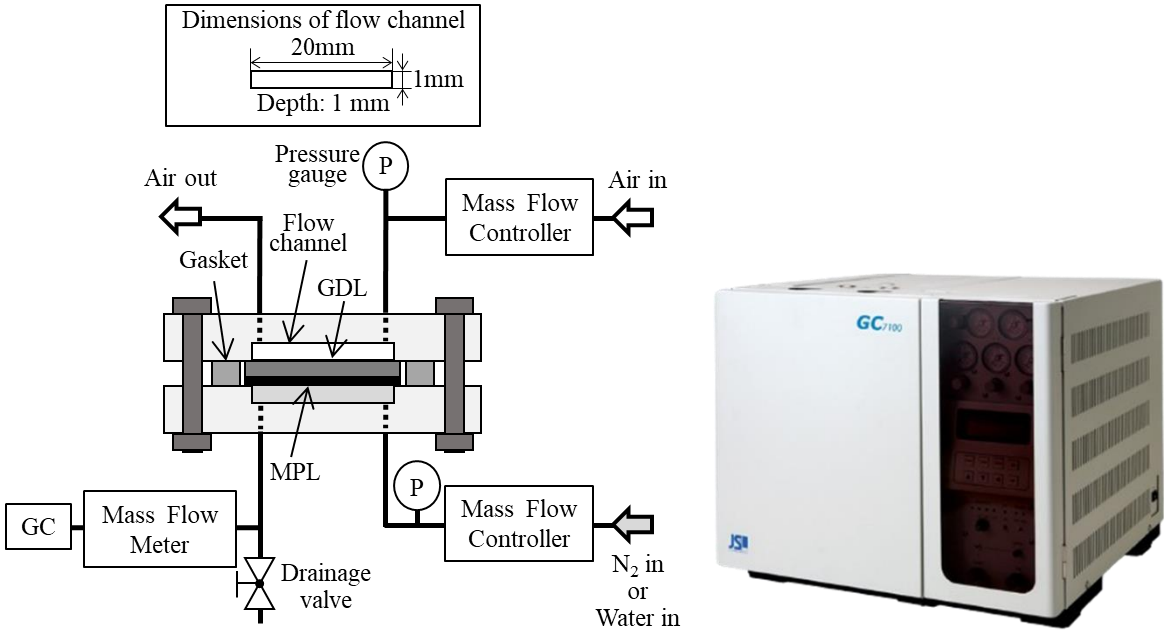

(a) Schematic of relative oxygen permeance test apparatus. (b) Gas chromatography apparatus.

Figure 2.7 The (a) schematic diagram of the relative oxygen permeance test apparatus and (b) gas chromatography apparatus.

Figure 2.8 illustrates the evaluation method of the oxygen permeance through the wetted MPL coated GDL. The water permeability test, in which liquid water was supplied to the lower flow channels at a steady pressure of 30 kPa, was conducted for 30 minutes in Figure 2.8(b). Then, all remaining water in the flow channels was removed using dry nitrogen purge gas. Finally, dry air and nitrogen were again provided to the upper and lower flow channels at a constant pressure of 1.0 kPa. Oxygen permeance through the wetted MPL coated GDL was

measured using the GC apparatus in Figure 2.8(c). The relative oxygen permeance k_{O2} was calculated using Eq. (2.5).

$$k_{O2} = \frac{q_{O2,wet}}{q_{O2,dry}} \tag{2.5}$$

where $q_{O2,dry}$ is the oxygen permeance of the completely dry GDL, and $q_{O2,wet}$ is the oxygen permeance immediately after the water permeability test.

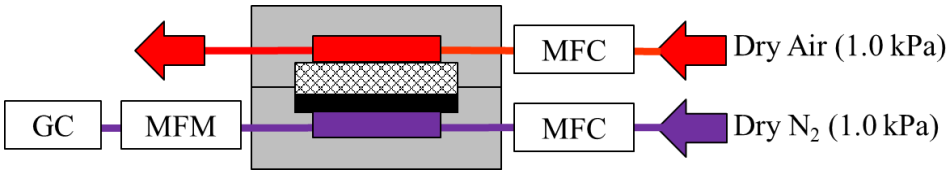

(a) Oxygen permeance under dry conditions $q_{O2,\,dry}$.

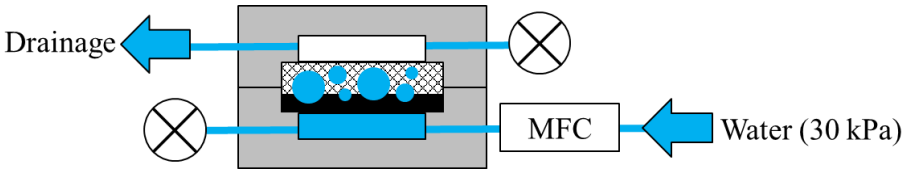

(b) Water permeability test to increase water saturation in the sample.

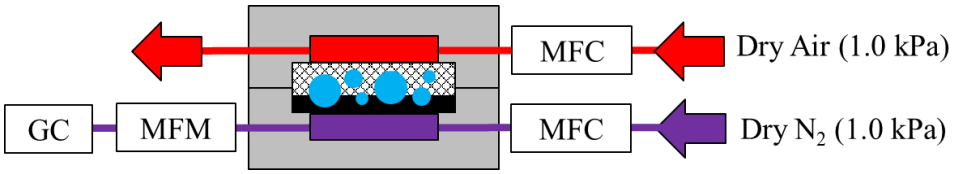

(c) Oxygen permeance under wet conditions $q_{O2,\,wet}$.

Figure 2.8 The relative oxygen permeance measurement method.

2.7 Oxygen Transport Resistance Evaluation

Efficient oxygen transport plays a crucial role in the overall performance of a PEFC because oxygen serves as a fundamental reactant in the electrochemical process responsible for generating electrical energy. When there is elevated oxygen transport resistance, it can impede reaction rates, subsequently affecting the overall efficiency. Oxygen transport resistance delineates the challenges and hurdles oxygen molecules encounter as they traverse through the diverse components of the fuel cell. Therefore, understanding and optimizing this resistance becomes imperative for improving cell efficiency.

2.7.1 The Experimental Cell Assemble

Figure 2.8 indicates the experimental cell assembly used in the performance measurement. The commercial MEA (GORE PRIMEA® MEAs A580.4/M815.15/C580.4) with 15 μm membrane thickness and Pt loading of 0.4 mg cm^{-2} was used to measure polarization curves. The active area of the cell was 1.0 cm^2. The separator had 17 parallel flow channels, each with a width of 0.4 mm, depth of 0.5 mm, and 0.2 mm of rib width. The cell assembly sandwiching the MEA, MPL coated GDLs, separators, and end plates tightened using eight bolts with adjusting the length of the springs, which the final length should be 11 mm to meet the suitable fixing torque.

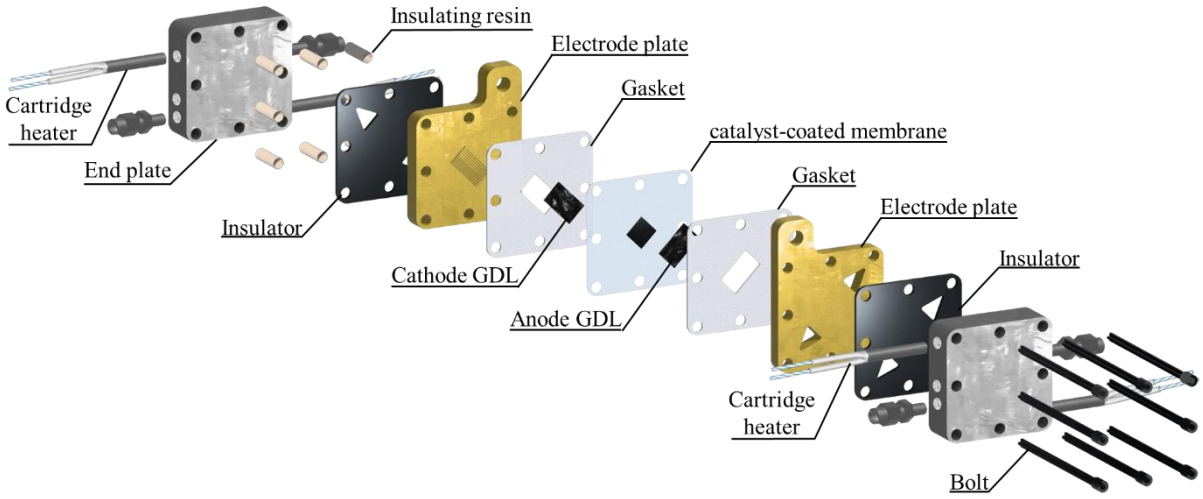

Figure 2.8 The experimental assembly cell with parallel channels.

The surface contact angles could help comprehensively understand the wettability of CL, MPL, GDL, and separator flow channels. The whole separators with flow channels were plated by the aurum, and the coating layer indicated high wettability, as shown in Figure 2.9(b), which helped reduce water droplet accumulation in the channels. Meanwhile, accompanied by a high supply flow rate, the oxygen transport resistance in the flow channel caused by accumulated water was eliminated.

(a) CL surface (b) Separator coating (c) Substrate (Toray® TGP-H-030) (d) Hydrophobic MPL (20%PTFE)

Figure 2.9 The wettability of the (a) CL surface, (b) separator coating, (c) Substrate (Toray® TGP-H-030), and (d) Hydrophobic MPL(20%PTFE).

In the tests, the sample compression ratio significantly influenced the ohmic resistance and porosity in the MPL. A sealing gasket was used to adjust the thickness of the sample in assembly to ensure that the samples remained in a similar compression state during the I-V measurements. The thickness of the sample after compression is set at 80% of the original thickness. The cell temperature was maintained at 35°C using a wind cooling system and 80°C by cartridge heater.

2.7.2 The PEFC Performance Evaluation Apparatus

In Figure 2.10, the gas supply setup is presented, where the air, H_2, and N_2 flow rates are regulated by the mass flow controller (MFC). Dry gases are directed to the cell and undergo humidification controlled by the bubblers. Backpressure valves manage piping pressure. Manipulating the mixing N_2 flow rate allows for controlling different oxygen concentrations, enabling the evaluation of oxygen transport resistance. Figure 2.11(a) illustrates the PEFC performance test apparatus, encompassing components such as the gas supply, gas pressure control, and humidity adjustment of the bubbler. The heater covers all piping to prevent water condensation, maintaining a temperature higher than the bubblers. The constant current (CC) method, depicted in Figure 2.11(b), was employed for measurements using the external electronic load (KIKUSUI PLZ164WA). The determination of IR overpotential relied on high-frequency resistance (HFR) measurements conducted with a resistance meter (TSURUGA MODEL 356E), as shown in Figure 2.11(c). Pure hydrogen and diluted oxygen gases were supplied at the anode and cathode in a cross-flow orientation. The flow rates were set at 1000 $cm^3\ min^{-1}$ to prevent water accumulation in the channels, so the effect of the R_{CH} on the R_{total} was negligible.

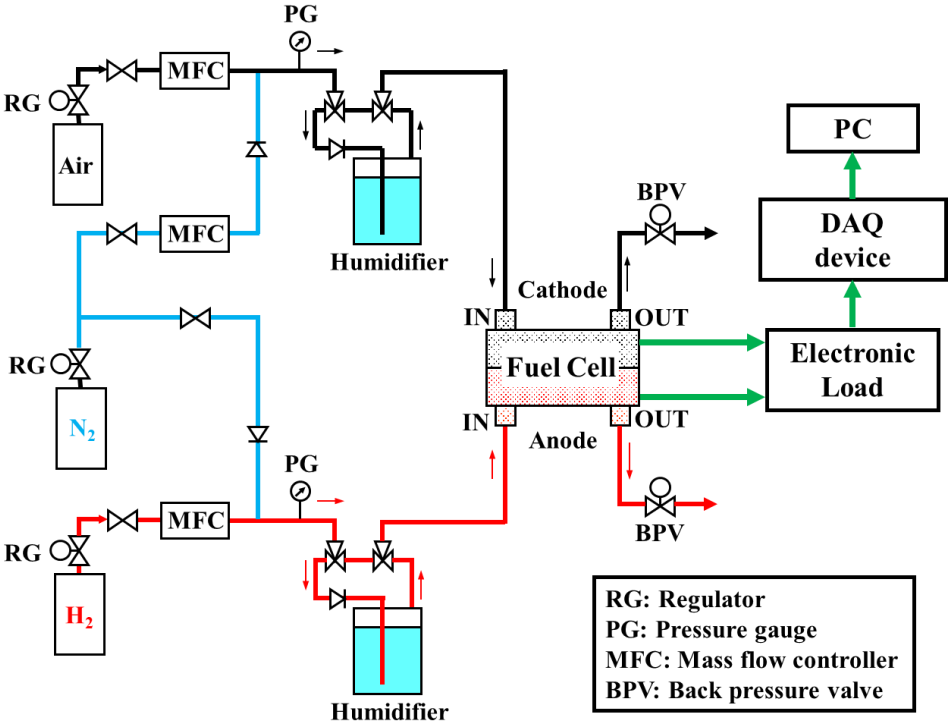

Figure 2.10 The schematic diagram of the PEFC test apparatus.

(a) The PEFC performance test apparatus.

(b) The electronic load.

(c) High-frequency resistance apparatus.

Figure 2.11 The (a) PEFC performance test apparatus, (b) electronic load for constant current (CC) measurement, and (c) high-frequency resistance (HFR) measurement apparatus.

2.7.3 The Total Oxygen Transport Resistance from Limiting Current Density in Polarization Curves and IR Overpotential

In PEFC operations, several parts affect oxygen transport within the fuel cell system, which includes the diffusion of oxygen through porous materials, the electrochemical reactions at the electrodes, and any constraints in the mass transport of oxygen to the reaction sites. In order to isolate the impact of the MPL, each component was kept the same during the experiment, which can highlight the impact of the MPL on cell performance.

The total oxygen transport resistance under specific conditions R_{O2} can be calculated by Eq. (2.6) based on limiting the current density i_{lim} from the polarization curve, as shown in Figure 2.12(a). Within the polarization curve of an electrochemical system, the i_{lim} denotes the highest current density attainable by the cell under specific conditions. When the system reaches the i_{lim}, it indicates a limitation imposed by mass concentration. At this point, the concentration of reactants near CL is considered zero, which implies that the oxygen concentration in the cathode catalyst layer has reached zero in PEFC. Meanwhile, the IR overpotential was measured when conducting the polarization measurement, as shown in Figure 2.12(b), which was influenced by the sample thickness and humidity in the cell.

$$R_{O2} = \frac{4F}{RT}\frac{p_{O2}}{i_{lim}} \tag{2.6}$$

where R_{O2} is the total oxygen transport resistance under specific oxygen concentration and pressure conditions, and p_{O2} is the average oxygen partial pressure of the inlet and outlet gases.

In those studies concerning GDL, the effectiveness of GDL in mitigating flooding was assessed under conditions simulating relatively dry operations in a PEFC, with a supplied gas relative humidity (RH) of 80% and a cell temperature of 80°C. However, in the case of fuel cell vehicles, it was anticipated that RH levels may exceed 100% at high current densities under relatively low-temperature conditions before reaching a steady state. Therefore, it was also necessary to evaluate the ability of the MPL to reduce flooding under high saturated conditions close to ambient temperature (35°C) with 200%RH and normal operation temperature (80°C) with 80%RH close to the steady state. During the tests, the measurement error was less than 5%. The small fuel cell from NEDO was used in the experiments, and the small active area

indicates homogenous current density and temperature distributions. The hydrophilic coating in the channel helped expel water. Meanwhile, accompanied by a high supply flow rate, it eliminates the oxygen transmission resistance in the flow channel caused by accumulated water and guarantees stable results. The rest of the graphs did not indicate the error bar when involving I-V characteristic curves and IR overpotentials for ease of reading.

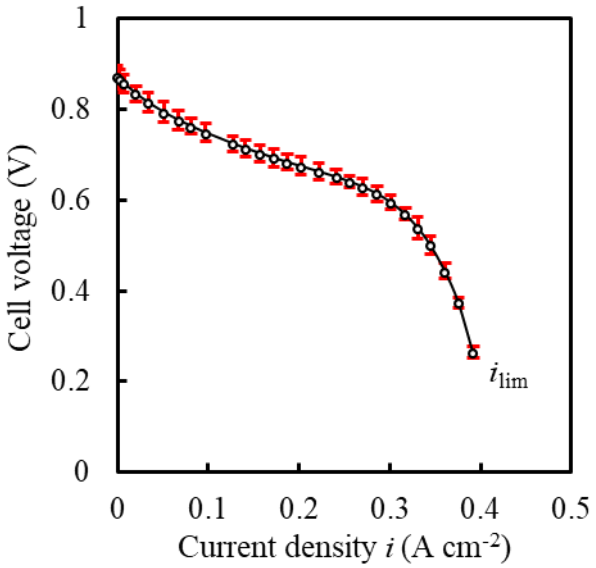

(a) The limiting current density from the polarization curve.

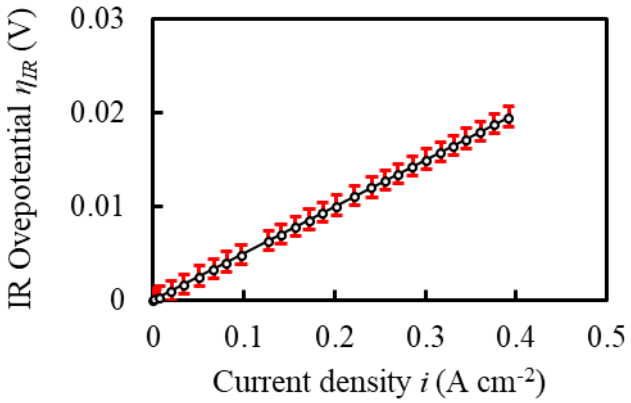

(b) The IR overpotential.

Figure 2.12 The limiting current density of the double MPL coated GDL from the polarization curve measurement.

The limiting current density measurement is usually used to evaluate the oxygen transport resistance in PEFCs. In this study, we employed a low oxygen concentration from 0.5% to 2.5% to measure the i_{lim} caused by the mass transport resistance. When the oxygen concentration increased, the limiting current densities significantly rose, accompanied by more

complex mass transport effects and ohmic and activation overpotentials. Thus, this low oxygen concentration strategy with relatively small i_{lim} was better for isolating the impact of mass transport resistance. This strategy reduced the influence of the activation overpotential, and cell performance was dominated by the mass transport resistance, which aligns with the oxygen transport resistance measurements conducted by Nonoyama et al. [58]. Both the experimental conditions are shown in Table 2.1.

Table 2.1 Test conditions of oxygen transport resistance measurements.

Parameters	Anode	Cathode
Active area (cm^2)	1.0	
Supply gas	H_2	O_2/N_2
Gas concentration (%)	100	O_2: 0.5~2.5
Flow rate ($cm^3\ min^{-1}$)	1000	1000
Supplied gas humidity (%RH)	200, 80	
Cell temperature (˚C)	35, 80	
Back pressure (kPa abs)	101, 150, 200, 300	

2.7.4 Pressure-dependent and Pressure-independent Diffusion Resistances

After obtaining the R_{total}, an essential evaluation of the performance of the microporous layer can be made. However, the extent to which the microporous layer contributes to flooding in the fuel cell cannot be assessed directly from the total oxygen diffusion resistance. Therefore, further oxygen diffusion impedance separation is necessary.

Figure 2.13(a) summarizes the relationship between the oxygen partial pressure p_{O2} and the limiting current density i_{lim} under various back pressure conditions within the measurement error of less than 5% [145]. Based on the linear relationship, the average total oxygen transport resistance R_{total} could be deformed to the following Eq. (2.7) [30,58].

$$R_{total} = \frac{1}{b}\frac{4F}{RT} \tag{2.7}$$

where b is the fitting line slope of the proportional relationship between i_{lim} and p_{O2}.

Figure 2.13(b) shows the correlation between the total oxygen transport resistance R_{total} and the gas pressure p_{gas} measured under various back pressure conditions. The total oxygen transport resistance R_{total} was governed by two distinct diffusion mechanisms: molecular gas diffusion, which influenced the pressure-dependent resistance R_p, and Knudsen diffusion, which dominated the pressure-independent resistance R_{np}. When the gas pressure was set to zero, R_p was also expected to be zero. Consequently, the R_{np} value corresponded to the intercept on the Y-axis of the total oxygen transport resistance, and the R_p value was determined by subtracting the R_{np} value from the R_{total} value.

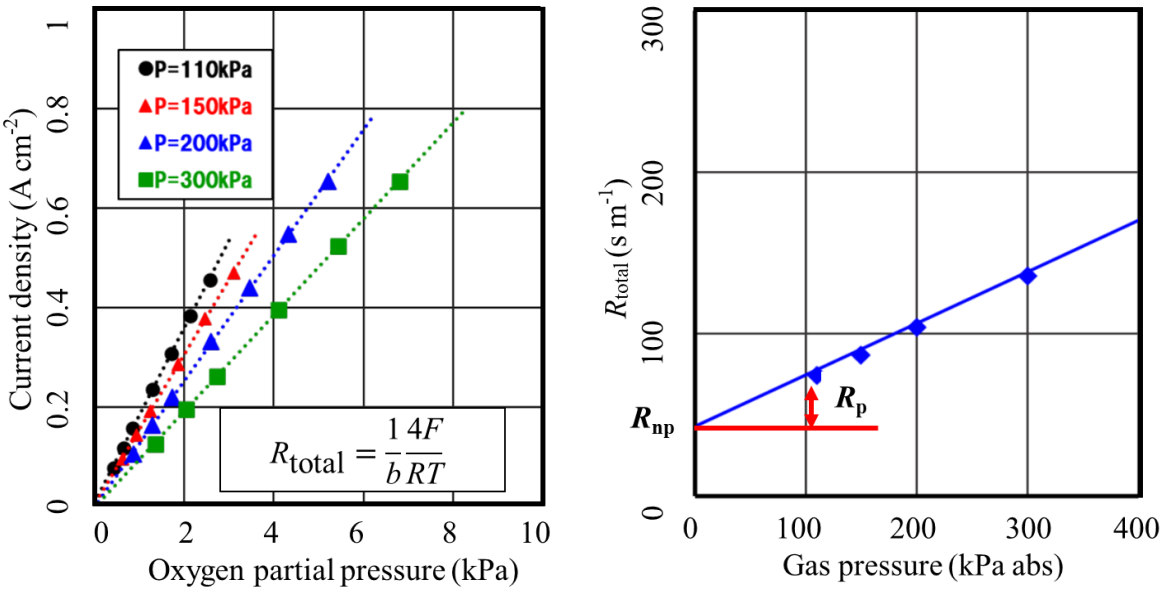

(a) Relationship between the limiting current density and oxygen partial pressure.

(b) The pressure-dependent and pressure-independent resistances separated from the total oxygen transport resistance.

Figure 2.13 The pressure-dependent and pressure-independent oxygen transport resistance separation method from the NEDO PEFC evaluation protocol [145].

3. Effect of Hydrophilic Layer in Double Microporous Layer Coated Gas Diffusion Layer on Performance of Polymer Electrolyte Fuel Cell

3.1 Double Microporous Layer Coated Gas Diffusion Layer

In the development of the double MPL coated GDL study, all MPLs were coated on a GDL substrate. The carbon paper (Toray® TGP-H-030) loaded with 5 mass% polytetrafluoroethylene (PTFE) (DAIKIN POLYFLON D-210C) to impart hydrophobicity was used as a GDL substrate with 110 μm thickness and 80 % porosity. In Figure 3.1(a), a conventional single hydrophobic MPL with a thickness of 35 μm consisting of carbon black (DENKA BLACK® HS-100, average particle diameter of 48 nm) and PTFE as the binder. The double MPL in Figure 3.1(b) was developed by introducing a 5 μm hydrophilic layer onto the single MPL coated GDL, in which the TiO_2 (SAKAI CHEMICAL INDUSTRY STR-100N) with a 15 nm average diameter was introduced as a hydrophilicity complement and Nafion (ALDRICH Nafion 1100EW) as the binder.

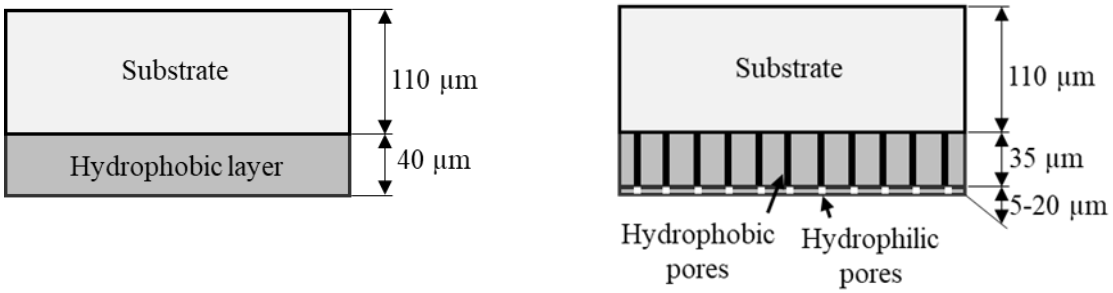

(a) Single MPL coated GDL. (b) Double MPL coated GDL.

Figure 3.1 The schematic diagrams of MPL coated GDLs.

To comprehensively evaluate the double MPL coated GDL, the formulation of the hydrophilic layer was determined by preparing both double and single MPL coated GDLs with different ingredients for surface contact angle, water breakthrough pressure, and in-pore contact angle tests, and the details are outlined in Table 3.1.

Table 3.1 Tested MPL coated GDL.

Sample Name	Hydrophobic layer	Hydrophilic layer
Single MPL (20%PTFE)	20 mass% PTFE 80 mass% CB	—
Double MPL (1%PVA)	20 mass% PTFE 80 mass% CB	1 mass % PVA 99 mass% CB
Double MPL (30%Nafion)	20 mass% PTFE 80 mass% CB	30 mass% Nafion 70 mass% CB
Double MPL (25%Nafion-5%TiO_2)	20 mass% PTFE 80 mass% CB	25 mass% Nafion 5 mass% TiO_2 70 mass% CB
Double MPL (15%Nafion-15%TiO_2)	20 mass% PTFE 80 mass% CB	15 mass% Nafion 15 mass% TiO_2 70 mass% CB
Double MPL (5%Nafion-25%TiO_2)	20 mass% PTFE 80 mass% CB	5 mass% Nafion 25 mass% TiO_2 70 mass% CB

3.2 The Double MPL Coated GDL Preparation Method

The preparation method of the single and double MPL coated GDL is demonstrated in Figure 3.2. A slurry containing PTFE, carbon black, distilled water, and a surface active agent was mixed using an impeller blade-type mixer (AS ONE Cell Master CM-100) and then coated on the substrate using an auto film coater machine (TESTER SANGYO PI-1210), as shown in Figure 3.3(a) and (b). The MPL was dried and then heated at 350 °C for 30 min to sinter the PTFE and carbon black on the substrate. The hydrophobic single MPL comprised 20 mass% PTFE and 80 mass% carbon black. All double MPLs consisted of a hydrophobic MPL and an extra hydrophilic MPL with a thickness of 5 μm, which sintered at 140 °C for 30 min. The double MPL contained 30 mass% of hydrophilic materials in different ratios but the same 70 mass% carbon black.

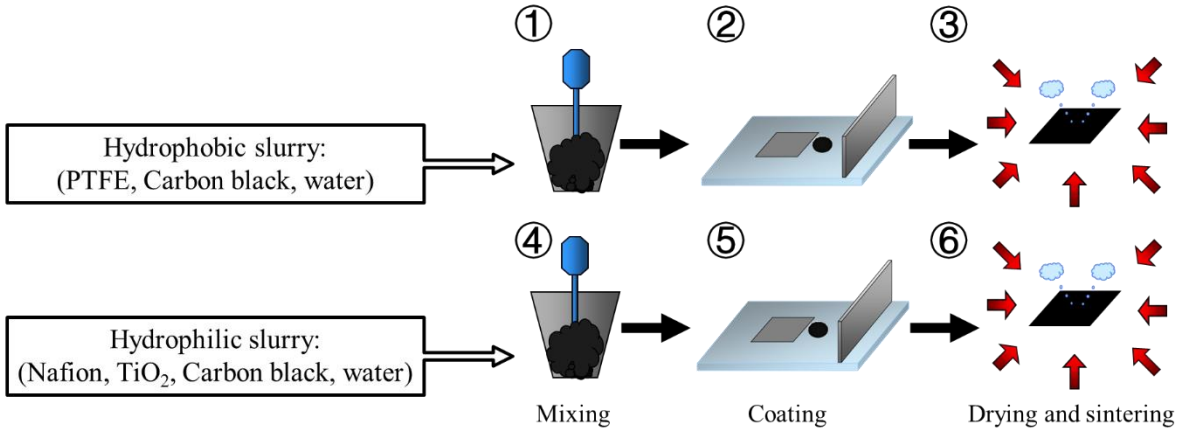

Figure 3.2 The single and double MPL coated GDLs preparation method.

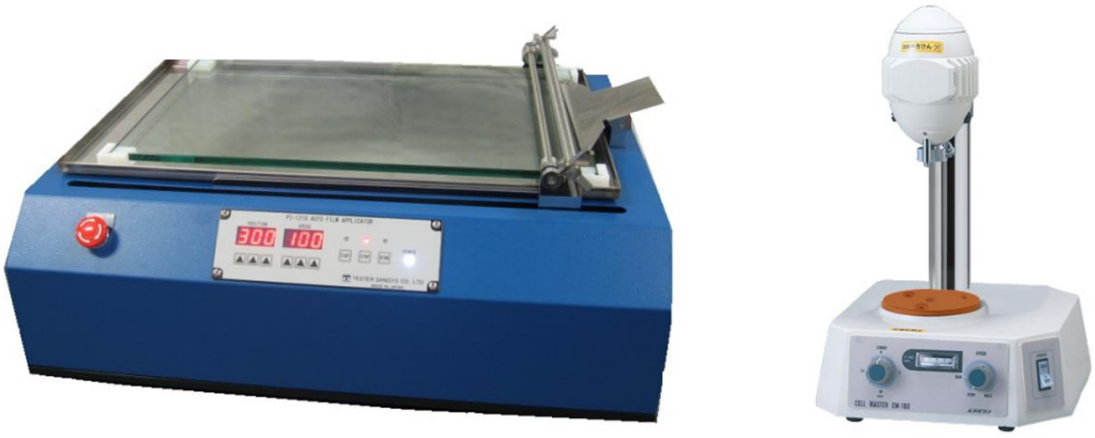

(a) The bar coating machine. (b) The impeller blade-type mixer.

Figure 3.3 The MPL coated GDL preparation apparatus.

3.3 Results and Discussion

3.3.1 The Surface Morphology of Carbon paper, Single MPL Coated GDL, and Double MPL Coated GDL

Figure 3.4 illustrates scanning electron microscope (SEM) surface images of the carbon paper substrate, hydrophobic and hydrophilic MPLs. In Figure 3.4(a), the carbon paper exhibited an uneven surface with excessively large pore sizes. Conversely, in Figure 3.4(b), applying an MPL resulted in a smoother surface as it covered the hollow carbon paper and significantly reduced the pore size. Furthermore, Figure 3.4(c) demonstrates that the surface roughness decreased after adding an extra hydrophilic layer. Consequently, the MPL effectively reduced the contact resistance between the GDL and the catalyst layer. In the hydrophobic MPL, the maximum pore was around 15 μm, and the pore structure consisted of carbon black as the main backbone, with an average particle diameter of 48 nm. The PTFE was a hydrophobic binder that bonded the particles and provided hydrophobicity. In hydrophilic MPL, the TiO_2 with a 15 nm average diameter was introduced as a hydrophilicity complement. Instead of using a hydrophobic PTFE binder, the hydrophilic Nafion binder was used to bond the carbon black and TiO_2 particles. This design allowed structurally stable samples that can be used for long-term experiments.

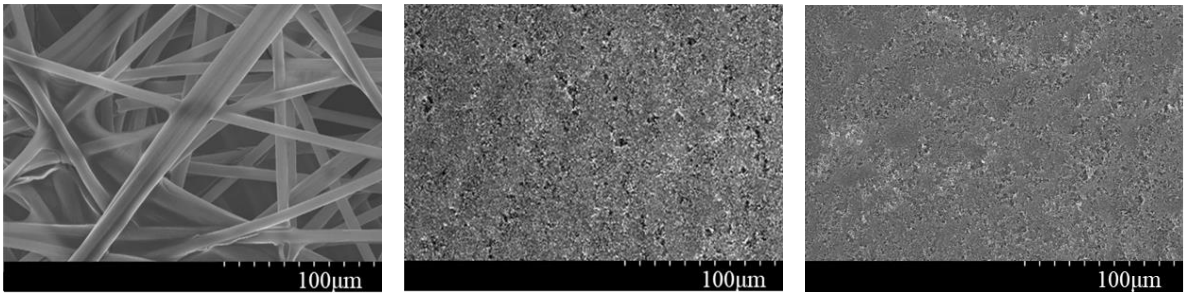

(a) Carbon paper (Toray® TGP-H-030).

(b) Single MPL coated GDL (20%PTFE).

(c) Double MPL coated GDL (5%Nafion-25%TiO_2).

Figure 3.4 Surface SEM micrographs of carbon paper, hydrophobic MPL, and hydrophilic MPL in a double MPL coated GDL.

The cross-sectional SEM photos are essential in describing the configurations of the MPL structures. However, the present cutting methods damaged the thin MPL, so it was difficult to

observe the structural differences, and this work will be rechallenged in future research to make the structural distribution display more straightforward.

3.3.2 Surface Contact Angles of MPLs

The property of the top hydrophilic layer in the double MPL was a fundamental parameter that must be clarified. Before the tests, the single MPL coated GDLs, holding the same compositions as the top hydrophilic layer of the double MPLs, as shown in Table 3.1, were explicitly prepared to conduct the surface contact angle, water breakthrough pressure, and in-pore contact angle measurements. The surface contact angle θ was measured using the sessile drop method. Figure 3.5 reveals that the hydrophobic MPL (20% PTFE) exhibited the highest contact angle value, indicating strong hydrophobicity. The MPL with 30% Nafion also displayed strong hydrophobic characteristics due to the effect of PTFE-backbone structures in Nafion. However, as the TiO_2 content increased in the MPL containing Nafion and TiO_2, the surface contact angles decreased from 134° to 58°, signifying a transition from hydrophobicity to hydrophilicity. The MPL with 1% PVA showed the most pronounced hydrophilicity. Despite providing valuable insights into MPL properties, an accurate contact angle measurement was challenging due to surface roughness. Consequently, meticulous measurement of the in-pore contact angle θ_{pore} for the MPL was necessary, as described in the following section.

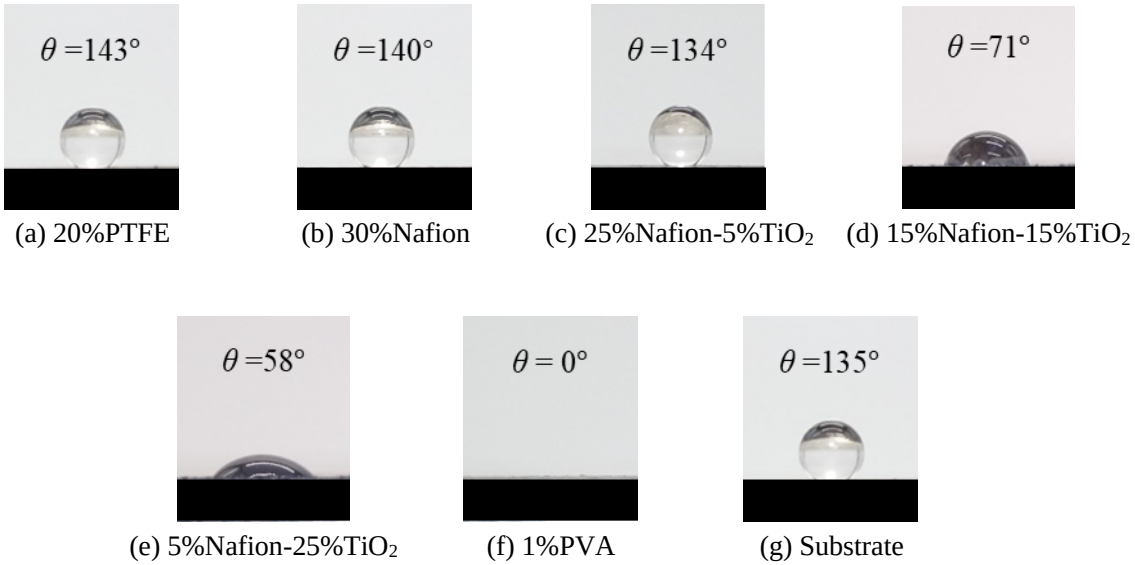

(a) 20%PTFE (b) 30%Nafion (c) 25%Nafion-5%TiO_2 (d) 15%Nafion-15%TiO_2

(e) 5%Nafion-25%TiO_2 (f) 1%PVA (g) Substrate

Figure 3.5 Surface contact angles of single MPL coated GDLs.

3.3.3 Water Breakthrough Pressures and In-Pore Contact Angles of MPLs

The water breakthrough pressure p_{water} was employed to assess the in-pore contact angle θ_{pore} of the MPL. Measuring p_{water} solely under dry conditions proved insufficient, as water molecules absorbed in sulphonic acid clusters in Nafion were evaporated when the sintering temperature of MPL was set at 140°C. Therefore, water treatment became essential to recreate water pathways and observe the actual properties of Nafion structures. The MPL coated GDL was immersed under vacuum conditions for 1 hour for water treatment. Figure 3.6 illustrates the water breakthrough pressures p_{water} obtained with and without water treatment for various MPL coated GDLs, and the maximum measurement error was less than 5%. The p_{water} of MPLs containing Nafion exhibited higher pressure values under dry conditions than after water treatment. The distinction in breakthrough pressure before and after water treatment was also evident in other hydrophilic MPLs incorporating Nafion and TiO_2. The p_{water} gradually decreased as the TiO_2 content increased. After water treatment, the MPL (5% Nafion - 25% TiO_2) achieved a p_{water} of 4 kPa.

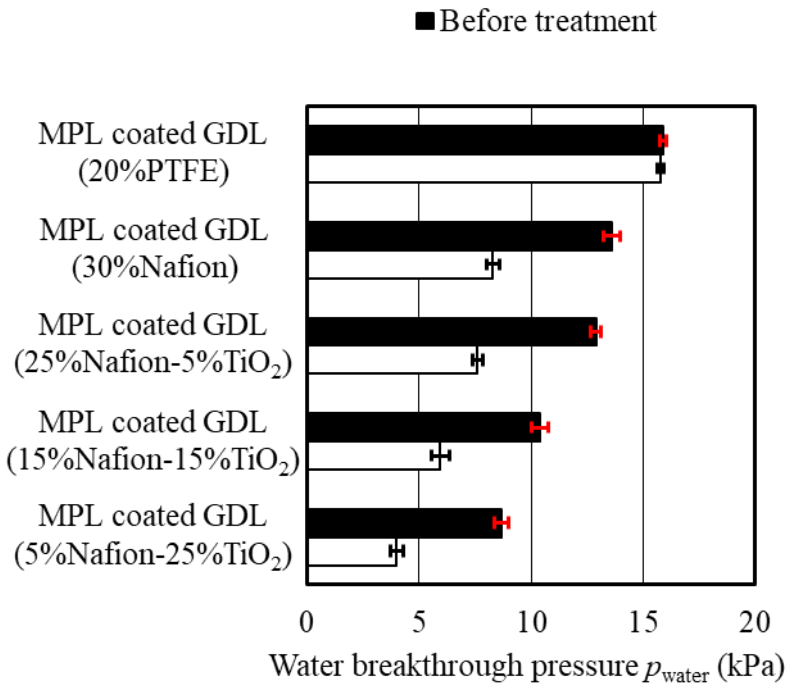

Figure 3.6 Water breakthrough pressures of MPL coated GDLs before and after water treatment.

Figure 3.7 indicates the in-pore contact angle θ_{pore} calculated from Eq. (2.3) based on the p_{water} measurements after water treatment, in which the measurement was also less than 5%.

The θ_{pore} obtained with the hydrophilic MPL containing Nafion was much lower than that with the MPL (20%PTFE). The θ_{pore} value of the MPL containing Nafion and TiO_2 decreased with increasing the TiO_2 content.

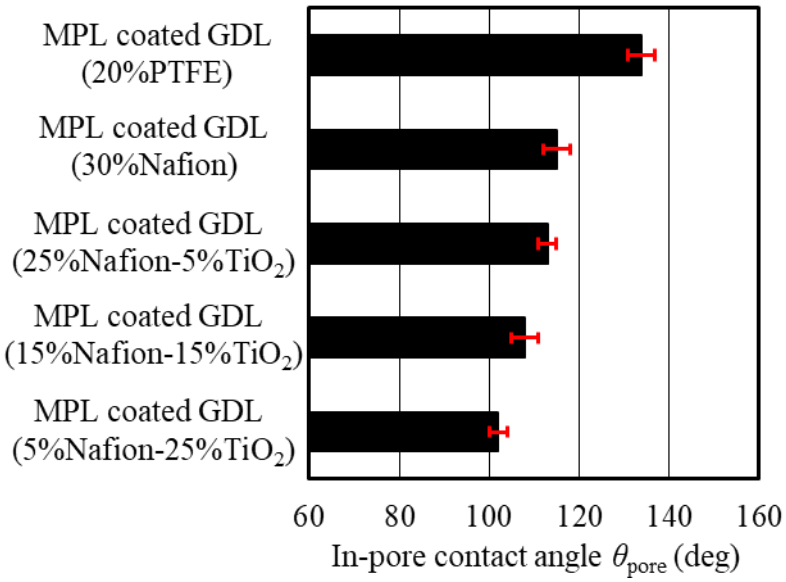

Figure 3.7 In-pore contact angles of MPL coated GDLs after water treatment.

3.3.4 Water Vapor Permeances of MPLs

Figure 3.8 illustrates the variations in the water vapor permeance q_{vapor} with increasing air velocity for single and double MPL coated GDLs. The air velocity U was defined as the flow rate divided by the cross-sectional area of the flow channel. The different MPL configurations will change the gas-liquid interface in the pore structures, so it is necessary to define the water vapor diffusion from the lower channel to the upper channel. It was defined as the water vapor permeance, the diffused amount of water vapor divided by the flow channel cross-section. The results obtained with the double MPL (1% PVA) were omitted in the figure as its water vapor permeance was exceptionally higher than the double MPL (5% Nafion-25% TiO_2). Under low-velocity conditions, the water vapor transport resistance at the GDL/air interface was significantly high, resulting in relatively low values of water vapor permeance. However, as the air velocity increased, the water vapor transport resistance decreased, leading to enhanced water vapor permeance. The water vapor permeance values finally stabilized beyond an air velocity of 10 m s^{-1}. The single hydrophobic MPL (20% PTFE) struggled to introduce water into its small hydrophobic pores, resulting in lower water vapor permeance. For the double MPL, the hydrophilic MPL facilitated the introduction of water into the pores of the hydrophobic MPL. Due to the liquid water supply pressure being maintained below the water breakthrough pressure, the liquid water would not penetrate the hydrophobic pores to the upper flow channel. The water vapor permeance varied depending on the degree of water introduction in the hydrophobic pores. Thus, the difference in the wettability of the hydrophilic MPL influenced the water vapor permeance, and the appropriate double MPL (5% Nafion-25% TiO_2) led to a higher water vapor permeance than the single hydrophobic MPL.

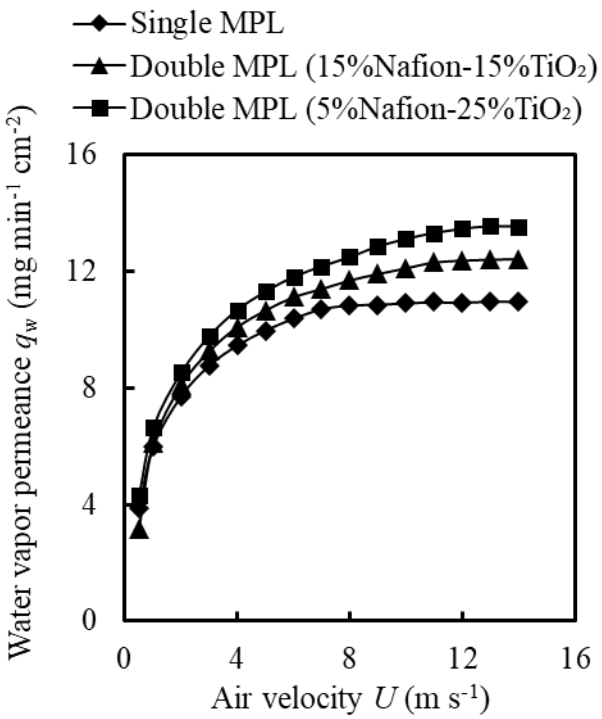

Figure 3.8 The water vapor permeance obtained with single and double MPL coated GDLs at a 35 °C cell temperature.

3.3.5 Effect of Hydrophilic Layer Thickness

Before evaluating the double MPL coated properties, it is necessary to determine the suitable hydrophilic layer thickness in advance. Here, the composition of the hydrophilic MPL was fixed as 5% Nafion-25% TiO_2. According to a comparison of the R_{total} values, Figure 3.9 shows the appropriate hydrophilic thickness as 5 μm, which was also the minimum thickness that can be prepared.

As mentioned in Chapter 1, the hydrophilic structure positively reduces CL/MPL interface accumulation water to alleviate flooding. However, the hydrophilic structure also increases the water saturation in the MPL, which hampers oxygen transport. From the results, when the hydrophilic MPL thickness was built thicker, the oxygen transport became challenging to pass through this high water saturation barrier to the CL reaction sites. Therefore, a thin hydrophilic layer is helpful to minimize adverse effects due to the barrier of the hydrophilic layer. A similar conclusion was also obtained by Shrestha et al. [134].

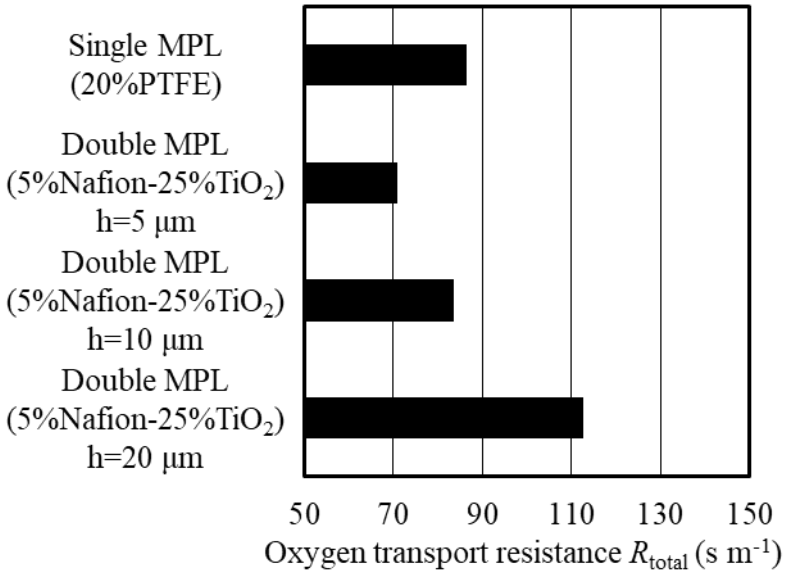

Figure 3.9 The total oxygen transport resistances obtained with double MPL coated GDLs with different hydrophilic layer thicknesses under conditions of 200%RH, a back pressure of 101 kPa abs, a supplied gas flow rate of 1000 cm^3 min^{-1}, and a 35 °C cell temperature.

3.3.6 Effect of Hydrophilic Layer Compositions on Total Oxygen Transport Resistance

Figure 3.10 demonstrates the polarization curves and IR overpotentials of single and double MPL coated GDLs. The limiting current density i_{lim} was directly obtained from the polarization curves, and the R_{total} can be calculated based on Eq. (2.7) to obtain the average value under all conditions.

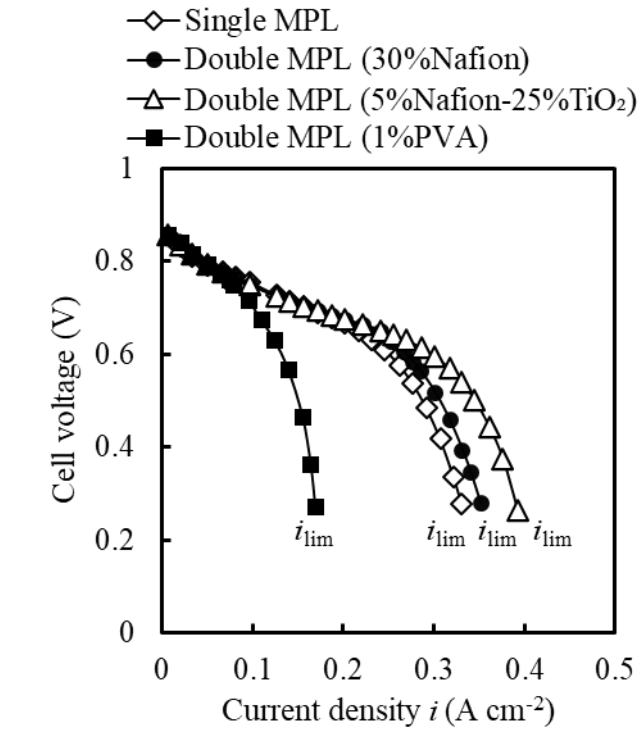

(a) Polarization curves

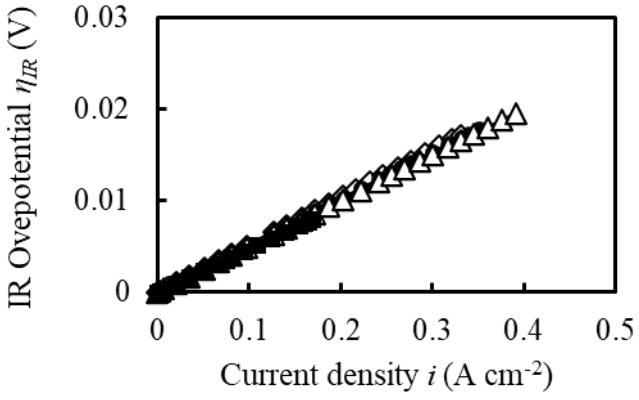

(b) IR overpotentials

Figure 3.10 Polarization curves and IR overpotentials obtained with single MPL and double MPL coated GDLs under conditions of 200%RH, a back pressure of 101 kPa abs, a supplied gas flow rate of 1000 cm^3 min^{-1}, and a 35 °C cell temperature.

In this study, we employed a low oxygen concentration from 0.5% to 2.5% to measure the i_{lim} caused by the mass transport resistance. When the oxygen concentration changed from 1% to 28%, the limiting current densities significantly rose from 0.2 to 4 A cm^{-2}, accompanied by more complex mass transport effects and overpotential losses [146]. In the I-V character measurement, the humidity was set at 200%RH, and the oxygen concentration was controlled in a low range, leading to a small current range that the activation overpotential would not change much to influence cell performance. Therefore, only the mass concentration overpotential impacted the cell performance under high humidity and low oxygen concentration conditions. This low oxygen concentration strategy with relatively small i_{lim} was better for isolating the impact of oxygen transport resistance, aligning with the measurements conducted by Nonoyama et al. [58]. Because the hydrophilic MPL thickness was set at 5μm, the effect of adding the hydrophilic layer on the ohmic resistance was negligible. Therefore, single and double MPL coated GDLs indicated similar IR overpotentials. Owejan et al. reported ohmic resistance values of approximately 0.07 Ω cm^2 at 80°C and 0.4 A cm^{-2} when the cell was under high humidity [147]. We observed similar ohmic resistance values of approximately 0.05 Ω cm^2 obtained with single and double MPL coated GDLs under high humidity conditions.

The composition of the hydrophilic layer was a critical design parameter for the double MPL. Figure 3.11 presents the R_{total} obtained with single and double MPL coated GDLs. The R_{total} of the hydrophobic MPL (20% PTFE) was 86.5 s m^{-1}. The R_{total} of the double MPL (30% Nafion) was close to that of the hydrophobic MPL (20% PTFE). Upon considering the water breakthrough pressure and in-pore contact angle depicted in Figures 3.6 and 3.7, the hydrophilic layer without TiO_2 had insufficient hydrophilicity, leading to an unsatisfactory reduction in oxygen transport resistance.

The R_{total} of double MPLs containing Nafion and TiO_2 decreased progressively with increased hydrophilicity. Among the double MPLs, the most outstanding performance was observed with the double MPL (5% Nafion-25% TiO_2), which achieved about a 20% reduction in oxygen transport resistance compared to the single hydrophobic MPL. Adding an appropriate hydrophilic layer in the double MPL configuration brought high water vapor permeance, considerably improving water-expelling ability. This characteristic efficiently facilitated water discharge from the catalyst layer to the flow channels, achieving the lowest

R_{total}. However, in the case of the double MPL using PVA, the hydrophilicity was too strong, causing an imbalance in water-gas transport and resulting in a significantly higher R_{total}.

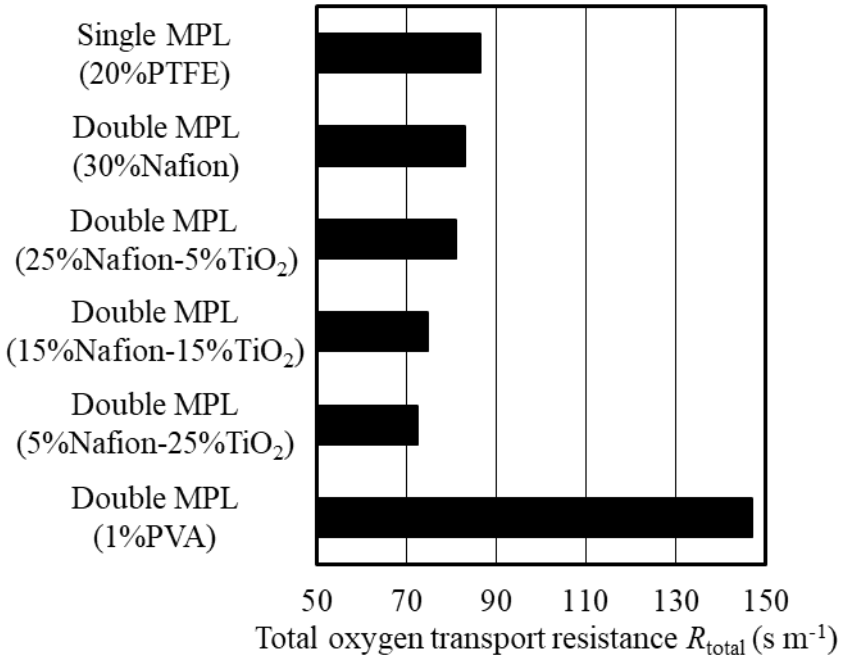

Figure 3.11 The total oxygen transport resistances obtained with single MPL and double MPL coated GDLs with different hydrophilic layer compositions under conditions of 200%RH, a back pressure of 101 kPa abs, a supplied gas flow rate of 1000 cm^3 min^{-1}, and a 35 °C cell temperature.

3.3.7 Effect of Double MPL Coated GDL on Pressure-dependent and Pressure-independent Resistances

The effectiveness of the double MPL coated GDL was considered by the pressure-independent resistance R_{np} and the pressure-dependent resistance R_p, which were separated from the R_{total} described in Eq. (2.7). Figure 3.12 summarizes the relationship between the oxygen partial pressure p_{O2} and the limiting current density i_{lim} under various back pressure conditions [57,59].

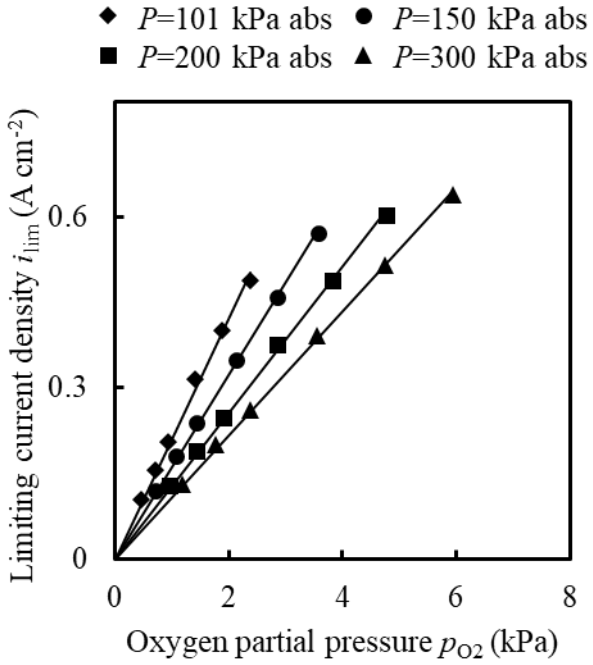

Figure 3.12 Relationship between the limiting current density and oxygen partial pressure obtained with a double MPL coated GDL (5%Nafion-25%TiO_2) at different back pressures under 200 %RH, a supplied gas flow rate of 1000 cm^3 min^{-1}, and a 35 °C cell temperature.

Figure 3.13 shows the correlation between the R_{total} and the gas pressure p_{gas} measured under various back pressure conditions. Owejan et al. measured the oxygen transport resistance of a hydrophobic MPL coated GDL under a 70°C cell temperature, 77%RH, a back pressure of 300 kPa, and various oxygen concentrations. From low to high water saturation, the oxygen transport resistance values increased from about 150 s m^{-1} to 260 s m^{-1} [147]. In this study, the oxygen transport resistance values under high saturated conditions of a 35°C cell temperature, 200%RH and a back pressure of 300 kPa obtained with single and double MPL coated GDLs were 174 s m^{-1} and 159 s m^{-1}, respectively. The R_{total} was governed by two distinct diffusion

mechanisms: molecular gas diffusion, which influenced the pressure-dependent resistance R_p, and Knudsen diffusion, which dominated the pressure-independent resistance R_{np}. When the gas pressure was set to zero, R_p was also expected to be zero. Therefore, the R_{np} value corresponded to the intercept on the Y-axis of the R_{total}, and the R_p value was determined by subtracting the R_{np} value from the R_{total} value.

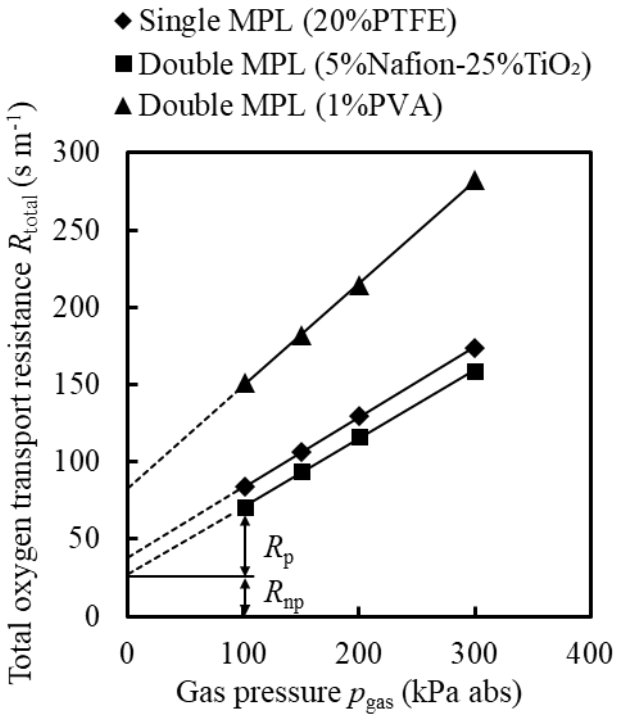

Figure 3.13 The pressure-dependent and pressure-independent resistances separated from the total oxygen transport resistance obtained with single MPL and double MPL coated GDLs at different back pressures under 200 %RH, a supplied gas flow rate of 1000 cm^3 min^{-1}, and a 35 °C cell temperature.

Figure 3.14 presents the total and separated values obtained with single and double MPL coated GDLs. For single hydrophobic MPL coated GDL, the excess liquid water mainly passed through the large pores generated in the hydrophobic MPL with relatively low capillary pressures. However, the water expelling ability could not meet the demand to further reduce the amount of the accumulated liquid water at the interface between the catalyst layer and the MPL, which hindered oxygen supply to the catalyst layer and increased the R_{np}. The appropriate double MPL (5% Nafion-25% TiO_2) demonstrated improved water discharge ability while maintaining efficient gas pathways. The hydrophilic MPL enabled water to spread in the in-plane direction, promoting the introduction of water into hydrophobic MPL pores. This created suitable pathways to alleviate liquid water at the catalyst layer. The enhanced

water transport was supported by the water vapor permeance results in Figure 3.8, which showed that the double MPL allowed more water vapor to pass through compared to the single hydrophobic MPL. As a result, the double MPL effectively reduced water accumulation at the interface between the catalyst layer and the MPL, which lowered the R_{total} caused by the considerable reduction in the R_{np}.

Conversely, double MPL (1% PVA) did not enhance performance. Despite exhibiting extremely high water vapor permeance due to its strong hydrophilicity, the hydrophilic layer suffered from excessive water absorption. Consequently, the accumulation of excess water in the hydrophilic layer caused severe flooding, resulting in significantly higher R_{np} and R_p values.

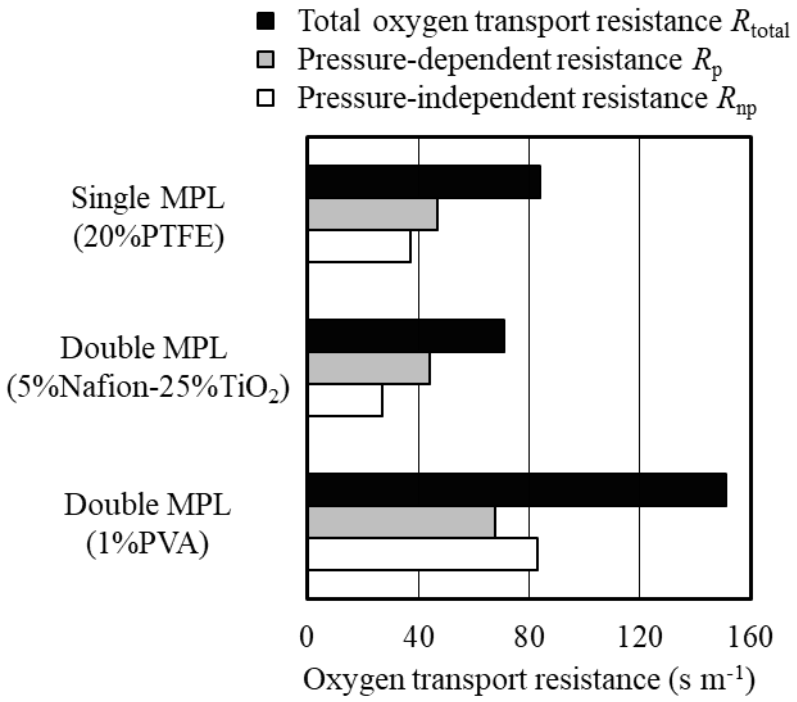

Figure 3.14 The pressure-dependent and pressure-independent oxygen transport resistances in the total oxygen transport resistance obtained from single MPL and double MPL coated GDLs under conditions of 200 %RH, a supplied gas flow rate of 1000 cm^3 min^{-1}, and a 35 °C cell temperature.

Comprehensively, the above results emphasized that both water vapor permeance and oxygen transport resistance were important properties in the double MPL design. Compared to the single MPL in Figure 3.15(a), an appropriate double MPL effectively improved the ability to discharge water from the catalyst layer, as shown in Figure 3.15(b), but the saturated hydrophilic MPL partially blocked the oxygen transport in the hydrophobic pores because the

hydrophilic pores only connected the CL and hydrophobic layer. Thus, a further performance enhancement could not be obtained.

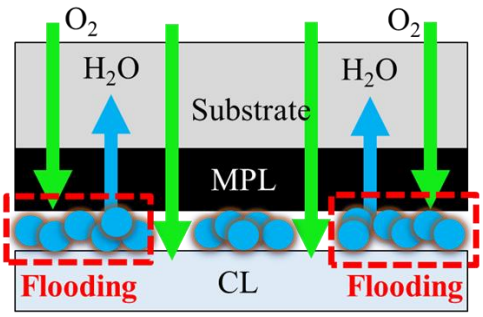

(a) Single MPL coated GDL

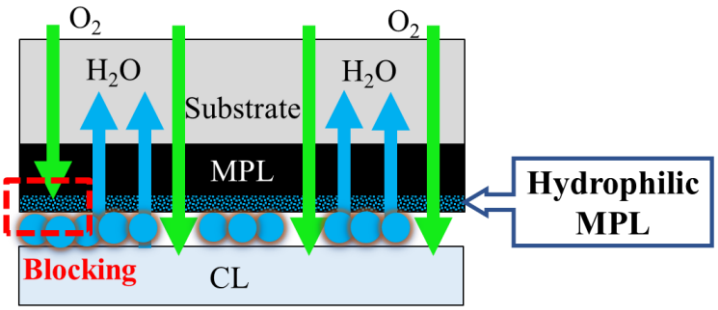

(b) Double MPL coated GDL

Figure 3.15 The schematic diagram of the water transport from the substrate to the CL in the cathode when applied (a) single MPL coated GDL and (b) double MPL coated GDL.

4. Hydrophilic and Hydrophobic Composite Microporous Layer Coated Gas Diffusion Layers for Performance Enhancement of Polymer Electrolyte Fuel Cells

4.1 Composite Microporous Layer Coated Gas Diffusion Layer

In this study, all MPLs were coated on a GDL substrate. The carbon paper (Toray® TGP-H-030) was loaded with 5 mass% PTFE. Figure 4.1 illustrates the schematic diagrams of conventional hydrophobic, hydrophilic, and composite MPLs. The concept of the composite MPL requires the generation of separate hydrophobic and hydrophilic pores in the same layer, so it is essential to investigate the miscibility of MPL slurries containing hydrophilic and hydrophobic materials, then develop an appropriate preparation method to ensure the creation of distinct hydrophobic and hydrophilic pores within the composite MPL after sintering the slurries. The hydrophobic binders selected the PTFE and PVDF (KISHIDA Chemical LBG-00968), and NMP (N-Methyl-2-pyrrolidone) (KISHIDA Chemical) was chosen as the PVDF binder solvent.

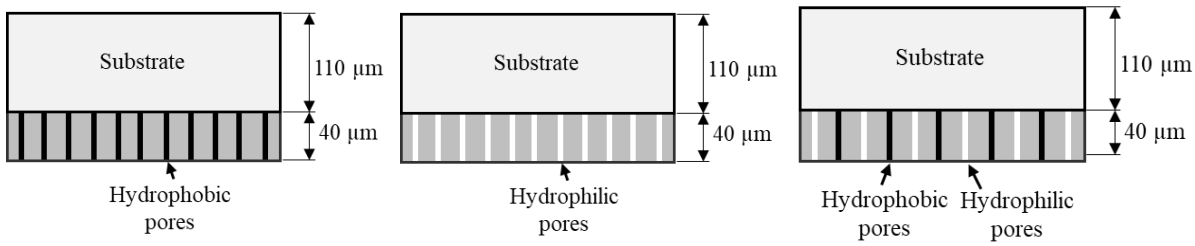

(a) Hydrophobic MPL (b) Hydrophilic MPL (c) Composite MPL

Figure 4.1 The schematic diagrams of hydrophobic, hydrophilic, and composite MPL coated GDLs.

Before preparing the composite MPL, it was necessary to check the miscibility of the hydrophilic and hydrophobic materials to keep the un-interfering hydrophilic and hydrophobic pores generated. Since the TiO_2 particles could be thoroughly mixed with the hydrophobic slurry, the TiO_2 particles would be evenly distributed in the entire MPL, forming a homogeneous pore structure rather than separate hydrophilic and hydrophobic pore structures. Thus, it was necessary to use Nafion as a hydrophilic solution to hold TiO_2 and guarantee that

it was not thoroughly mixed with hydrophobic slurry within a short period. The immiscibility between the water-soluble Nafion binder and water-insoluble PVDF binders was initially examined. Figure 4.2 demonstrates a clear boundary under static conditions. This lack of miscibility was advantageous for creating the composite MPL to guarantee the separate formation of hydrophobic and hydrophilic pores. The samples used in the performance test are summarized in Table 4.1.

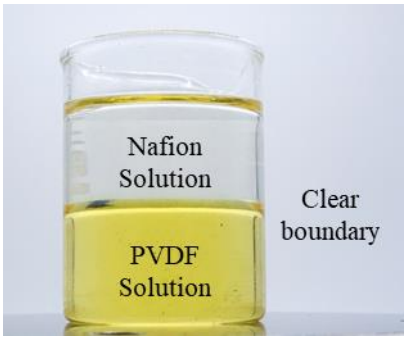

Figure 4.2 The immiscible phenomenon between Nafion and PVDF solutions.

Table 4.1 The tested MPL coated GDLs.

MPL coated GDL (d_{max}=20μm)	Hydrophobic material (mass%)	Hydrophilic material (mass%)	Carbon black (mass%)
Hydrophobic MPL (20%PTFE)	20% PTFE	—	80%
Composite MPL (15%PTFE-5%PVA)	15% PTFE	5% PVA	80%
Hydrophobic MPL (20%PVDF)	20% PVDF	—	80%
Composite MPL (15%PVDF-5%PVA)	15% PVDF	5% PVA	80%
Composite MPL (10%PVDF-10%Nafion)	10% PVDF	10% Nafion	80%
Composite MPL (10%PVDF-7.5%Nafion-2.5%TiO_2)	10% PVDF	7.5% Nafion 2.5% TiO_2	80%
Composite MPL (10%PVDF-5%Nafion-5%TiO_2)	10% PVDF	5% Nafion 5% TiO_2	80%
Composite MPL (10%PVDF-2.5%Nafion-7.5%TiO_2)	10% PVDF	2.5% Nafion 7.5s% TiO_2	80%
Hydrophilic MPL (7.5%Nafion-2.5%TiO_2)	—	7.5% Nafion 2.5% TiO_2	90%

4.2 The Composite MPL Coated GDL Preparation Methods

As for the MPL preparation, a separate mixing method was applied to prevent excessive mixing of the hydrophobic and hydrophilic binders, as shown in Figure 4.3(a). The impeller blade-type mixer was employed to mix the hydrophilic and hydrophobic slurries for 1 hour. Subsequently, the hydrophobic and hydrophilic slurries were mixed and coated on the substrate using an auto film coater machine. The MPLs were dried at 35°C and then sintered at 150°C. To evaluate the preparation methods, the composite MPL was also prepared with the premixing method, in which all hydrophilic and hydrophobic materials were mixed together for 1 hour, then dried and sintered in the same manner, as shown in Figure 4.3(b). In the results and discussion section, we elucidate the performance difference between the separate mixing and premixing methods to distinguish the hydrophobic and hydrophilic pores based on water permeability and relative oxygen permeance test results.

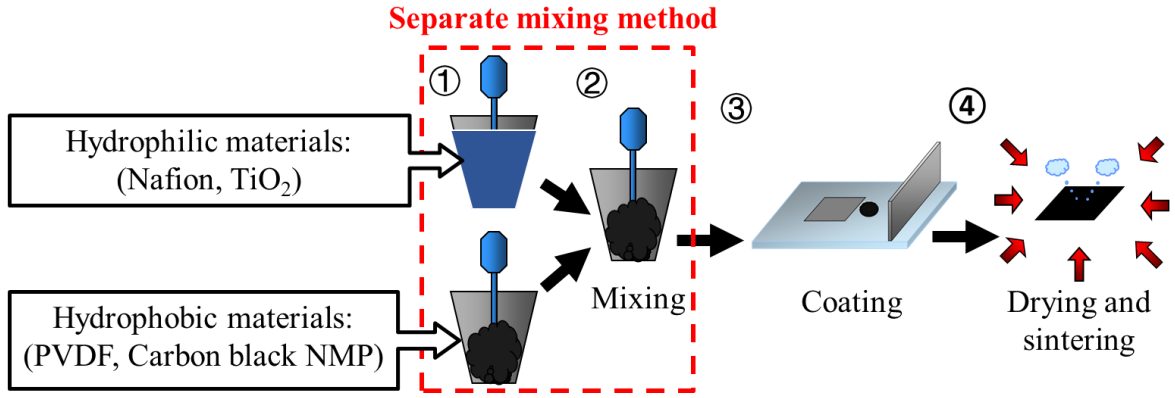

(a) Separate mixing method.

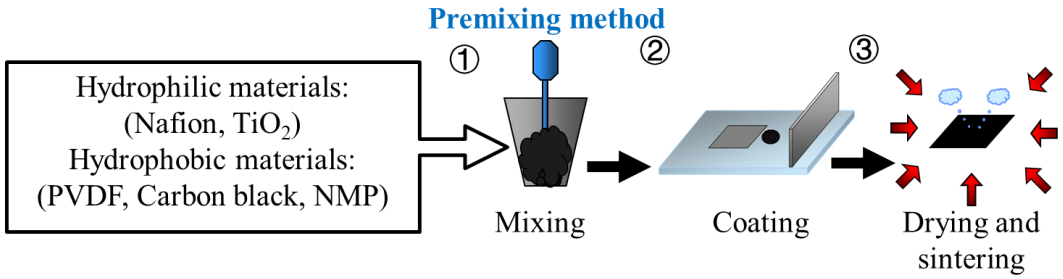

(b) Premixing method.

Figure 4.3 The separate mixing and premixing methods for composite MPL coated GDL preparation.

4.3 Results and Discussion

4.3.1 The Surface Morphology of Carbon Paper, Single and Composite MPL Coated GDLs

Figure 4.4 provides SEM surface images of the carbon paper substrate, hydrophobic MPL, and composite MPLs. In Figure 4.4(a), the carbon paper surface appears uneven with huge pore sizes. Contrastingly, Figure 4.4(b) shows that applying hydrophobic MPL results in a smoother surface, covering the hollow carbon paper and significantly reducing pore sizes. Figure 4.4(c) also displays the composite MPL surface, indicating a smooth texture. As a result, the MPL proves effective in reducing contact resistance between the GDL and the catalyst layer.

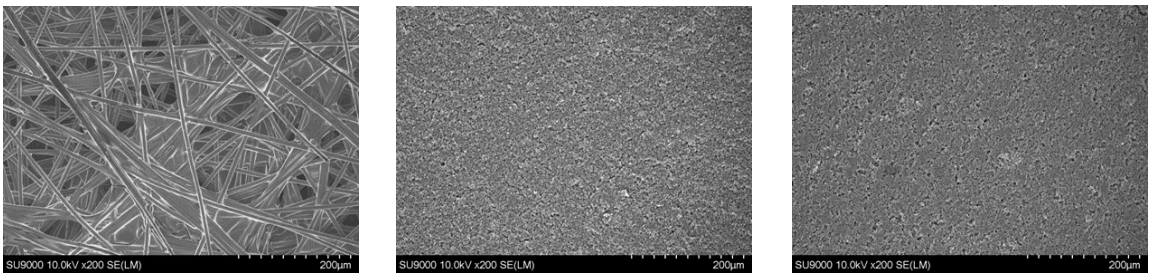

(a) Carbon paper (Toray® TGP-H-030)

(b) Single MPL (20%PVDF)

(c) Composite MPL (10%PVDF-5%Nafion-25%TiO_2)

Figure 4.4 Surface SEM micrographs of carbon paper, hydrophobic MPL, and composite MPL coated GDLs.

4.3.2 Effect of PTFE and PVA Composite MPL

To determine the appropriate hydrophobic and hydrophilic compositions, we evaluated the commonly used PTFE as a hydrophobic binder and polyvinyl alcohol (PVA) as a hydrophilic binder. However, there was a noticeable difference in sintering temperatures between PTFE (350°C) and PVA (150°C). To assess the impact of sintering temperature on composite MPL property, we prepared a composite slurry containing PTFE, PVA, carbon black, deionized water, and a hydrophilic surface active agent and coated it on the GDL substrate. Then, the sintering temperature was set at 350°C or 150°C to produce the MPLs. Figure 4.5 indicates the surface contact angle θ of the hydrophobic, hydrophilic, and composite MPLs measured using the sessile drop method. When the composite MPL (15%PTFE-5%PVA) was sintered at 350°C, the PVA binder was utterly burned off, transforming the composite MPL into a hydrophobic MPL with the same contact angle value as the pure hydrophobic MPL. In contrast, when the sintering temperature was reduced to 150°C, the composite MPL (15%PTFE-5%PVA) displayed strong hydrophilicity with a contact angle of 0°, similar to the hydrophilic MPL (5%PVA). Under 150°C sintering conditions, the PTFE lost hydrophobic properties due to the inability to eradicate the surface active agent.

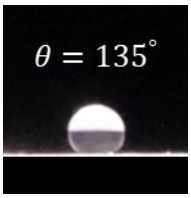

(a) Hydrophobic MPL (20%PTFE)

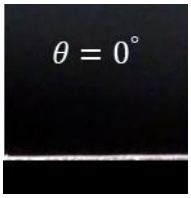

(b) Hydrophilic MPL (5%PVA)

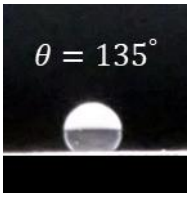

(c) Composite MPL(15%PTFE-5%PVA) (Sintering at 350°C)

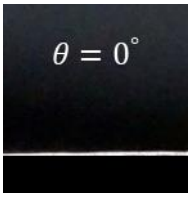

(d) Composite MPL(15%PTFE-5%PVA) (Sintering at 150°C)

Figure 4.5 The surface contact angles of hydrophobic, hydrophilic, and composite MPLs.

Figure 4.6 shows the oxygen transport resistance R_{total} of the hydrophobic, hydrophilic, and composite MPLs. The composite MPL sintered at 350°C exhibited a similar R_{total} value as that

obtained with the hydrophobic MPL (20%PTFE). The composite MPL (15%PTFE-5%PVA) sintered at 150°C, indicating strong hydrophilicity and a tremendous increase in R_{total}.

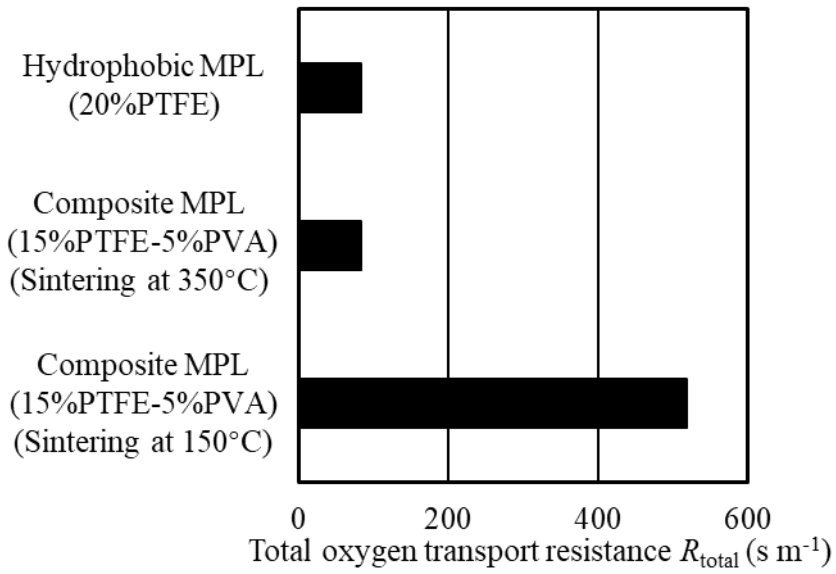

Figure 4.6 The total oxygen transport resistances obtained with hydrophobic MPL (20%PTFE) and composite MPL (15%PTFE-5%PVA) coated GDLs at different sintering temperatures under conditions of 200%RH, supplied gas flow rate of 1000 cm^3 min^{-1} and cell temperature of 35 °C.

4.3.3 Effect of the Mixing Methods of Hydrophobic and Hydrophilic Slurries

4.3.3.1 The Water Permeability Test to Determine the Properties of Pore Structures

Figure 4.7 indicates the water permeability test results obtained with the hydrophobic MPL (20%PVDF), hydrophilic MPL (7.5%Nafion-2.5%TiO_2), and composite MPLs (10%PVDF-7.5%Nafion-2.5%TiO_2) prepared with the separate mixing and premixing methods. The reason for selecting this ingredients ratio in composite MPL will be verified in the following section, as described in Figure 4.14.

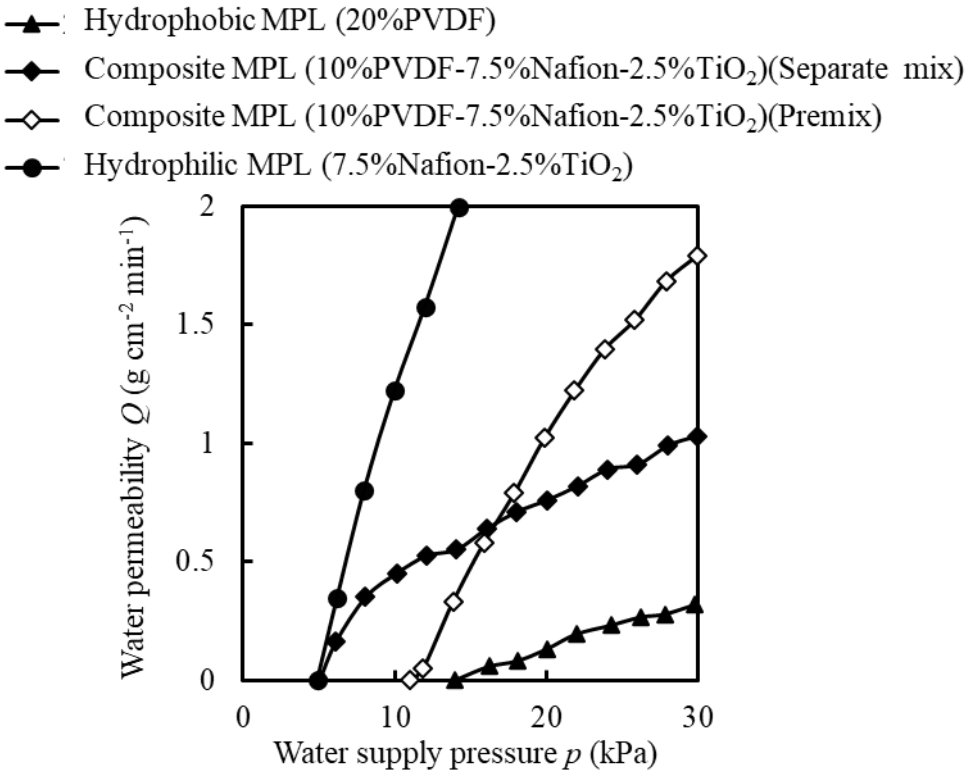

Figure 4.7 The water permeability results of the hydrophobic MPL (20%PVDF), hydrophilic MPL (7.5%Nafion-2.5%TiO_2), and composite MPL (10%PVDF-7.5%Nafion-2.5%TiO_2) prepared with separate mixing and premixing methods.

The water breakthrough pressure obtained with the composite MPL with the separate mixing method was similar to that obtained with hydrophilic MPL. The composite MPL with the separate mixing method demonstrated two different rising slopes of the water flow rate. The hydrophilic pores caused the initial slope, which followed the tendency of hydrophilic MPL because water could readily pass through the hydrophilic pores. The following slope changed when the water supply pressure was high enough to pass the hydrophobic pores, and the slope was close to the pure hydrophobic MPL. The water flow rate obtained with the

composite MPL with the separate mixing method was much higher than that obtained with the hydrophobic MPL. Based on the water permeability characteristics, it is considered that the hydrophobic and hydrophilic pores were separately generated in the composite MPL.

The composite MPL with the premixing method did not present clear and different water permeability slopes, which means the hydrophobic and hydrophilic materials simultaneously existed in the same pore, so the pure hydrophilic and hydrophobic pores were not generated. The premixing composite MPL lowered the hydrophobicity of pores, and the water breakthrough pressure was the intermediate value between the hydrophobic MPL and hydrophilic MPL.

4.3.3.2 The Water Permeability Simulation Analyze

After obtaining the water permeability test results, a simple pore distribution assumption was raised to evaluate whether the results were reasonable. Using Hagen-Poiseuille's law, the tube model of MPL coated GDL was assumed as Figure 4.8(a), with the water flow rate per unit area can be calculated by Eq. (4.1). Here, the hydrophobic MPL, hydrophilic, and composite MPL applied the same discrete pore distribution, which the pore distribution model with a maximum pore diameter of 20 μm, mean pore diameter of 5 μm, and porosity of about 65%, as shown in Figure 4.8(b) [87].

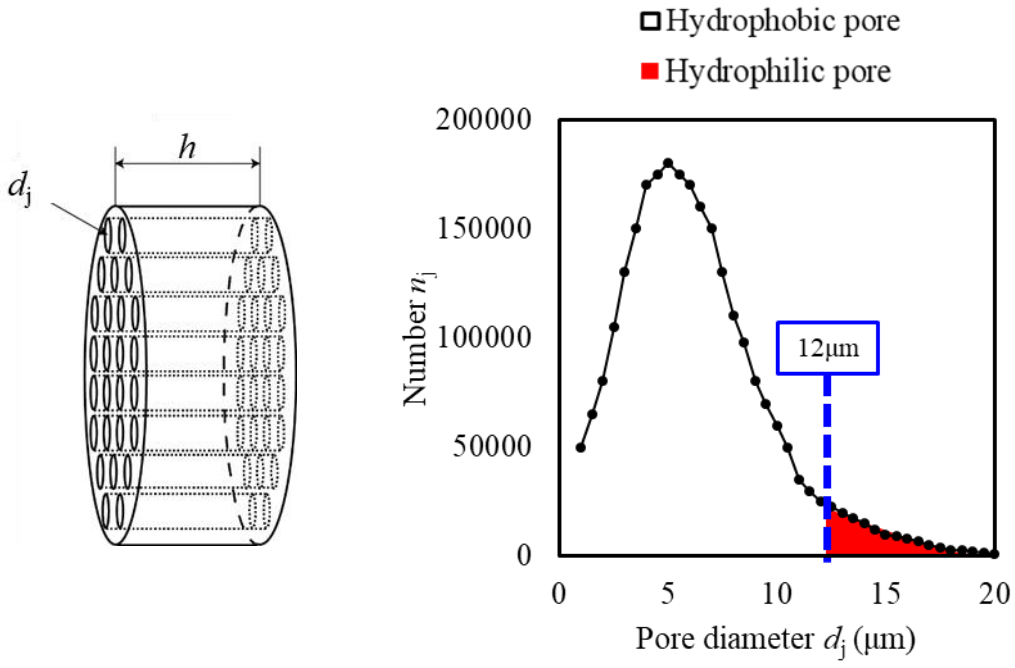

(a) Tube model. (b) Discrete pore distribution model.

Figure 4.8 The (a) tube model and (b) discrete pore distribution model of MPL for calculation, pore diameter d_j is from 1-20 μm, and porosity is 65%.

For composite MPL, the large pores were assumed to possess hydrophilicity, and the pore distribution was sharply divided into hydrophobic parts with relatively small pore sizes and hydrophilic parts from 12 μm, as indicated in Figure 4.8(b). The in-pore contact angles were calculated from the experimental water breakthrough pressure, 135° for hydrophobic and 110° for hydrophilic pores from the previous chapter of the double MPL evaluation. Based on Eq. (4.2), the pores that can be permeated are determined by comparing the water supply pressure p to the capillary force of the pores. The water permeability simulation resultsa are shown in Figure 4.9.

$$q_j = \frac{n_j p \pi d_j^4}{128 \mu h} \tag{4.1}$$

where dj is the pore diameter, j is the serial number corresponding to the pore size in the range of 1-20 μm, q_j is the water flow rate corresponding to specific pore diameter ($cm^3\ min^{-1}$), n_j is the number of permeable pores at specific pore diameter, μ is the viscosity coefficient, μ_{water}=0.00001822 (Pa s), and h is the length of the pore (m).

$$p_j = \frac{-4\gamma \cos \theta_{pore}}{d_j} \tag{4.2}$$

where p_j is the capillary pressure corresponding to specific pore diameter (kPa), θ_{pore} is the in-pore contact angle (deg), γ is the surface tension of wetting liquid (γ_{water}=0.072 N m^{-1}).

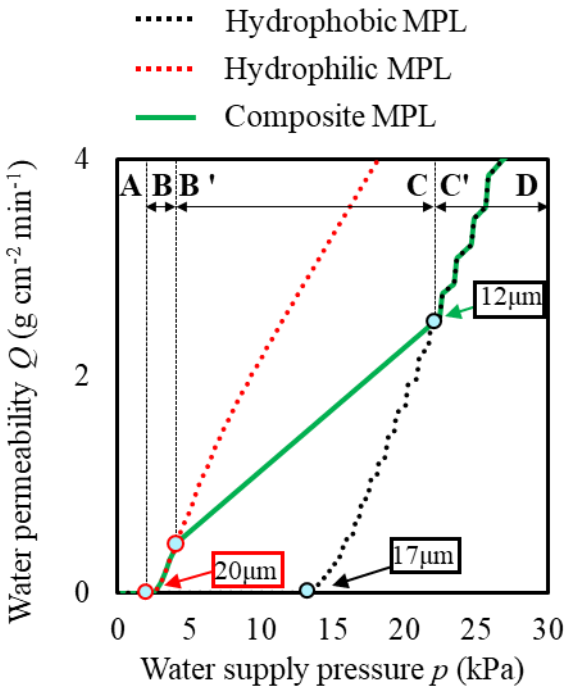

(a) Water permeability simulation results from 0 to 30 kPa.

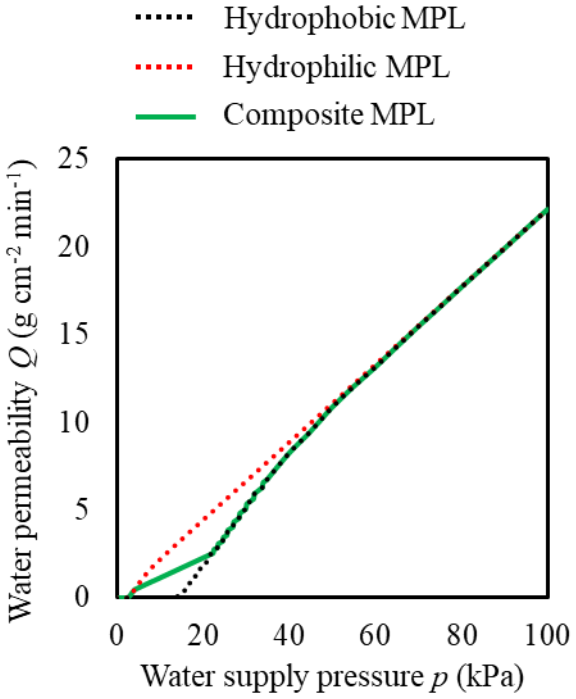

(b) Water permeability simulation results from 0 to 100 kPa.

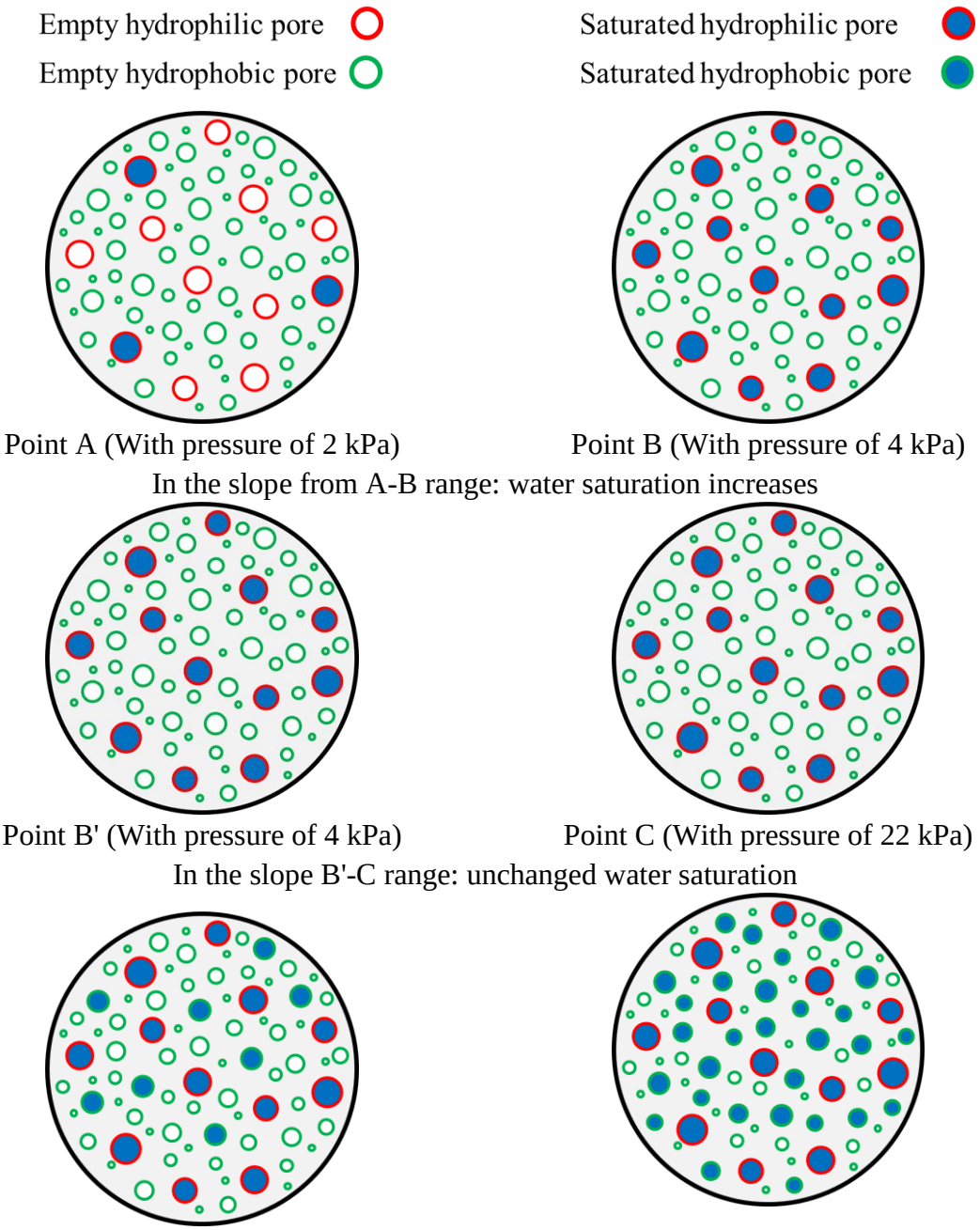

(c) The schematic diagram of the cross-sectional area of the hydrophilic and hydrophobic pores participate in water transport at the slope change points.

Figure 4.9 The (a) water permeability simulation results from 0 to 30 kPa, (b) water permeability simulation results from 0 to 100 kPa, and (c) The schematic diagram of the cross-sectional area of the hydrophilic and hydrophobic pores participate to water transport at the slope change points.

During the simulation process, as shown in Figure 4.8(b), since the pore size distribution model was a discrete data model, the pores in each MPL were progressively occupied by water as the pressure gradually increased. The supply pressure continues to grow, but no more holes

will be added to the water transfer until the supply pressure reaches the capillary pressure corresponding to the next hole size. At this moment, all pores that already participated in water transfer reached a saturated state. Therefore, the water permeability simulation results followed Hagen-Poiseuille's equation, so the simulation results showed a step-like shape.

In the results, the water permeability corresponding to all samples increased rapidly at the relatively low-pressure stage, as shown in Figure 4.9(a). This is because the permeated pore diameter increased as the pressure was raised. Under the joint action of the corresponding pore number and pressure, showing a growth slope greater than 1, the water permeability curve was concave downward.

Here, the explanation focused on the composite MPL. For composite MPL, as described previously, the initial slope range corresponding to water saturation of the hydrophilic pores gradually increased with supply pressure and the number of pores, generating a water permeability curve downward concave, as shown in Figure 4.9(a)-A to B, relating to water saturation of the pores is shown in Figure 4.9(c)-A and B. After the limited hydrophilic pores reached saturation in Figure 4.9(a)-B', the hydrophobic pores had not yet participated in water transport as in Figure 4.9(c)-B'. Hence, the water permeability at this transient period in Figure 4.9(a)-B' to C increased with the supply pressure, resulting in a lower second slope. When the supply pressure was larger enough than 22 kPa in Figure 4.9(a)-C', hydrophobic pores with a maximum pore diameter of 12um began to participate in water transmission as Figure 4.9(c)-C', and as the supply pressure continued to increase, more small hydrophobic pores joined in water transmission as Figure 4.9(c)-D. At this time, the water transport of the composite sample was shared through all hydrophilic pores, and some hydrophobic pores, thus forming the third slope, as shown in Figure 4.9(a)-C' to D.

The simulation with the expanded supply pressure range is shown in Figure 4.9(b). Eventually, when the supply pressure was larger than 50 kPa, most pores in each sample reached a saturated state. At this point, the water permeability only changed with pressure, so all samples indicated similar water permeability by applying the same pore distribution. Therefore, comparing the calculation results and experimental data, the decreased water permeability slopes are reasonable in the experiment because the experimental data only indicated the initial and transient slopes, which resulted from the distribution of the hydrophilic

and hydrophobic pores in the composite MPL. If the water supply pressure could be increased as high as possible, the third slop of water permeability would be obtained.

While the above results have identified the best method for making composite MPLs, whether there is a difference in the actual internal pore structure cannot be further confirmed. However, it is believed that the separate hydrophilic and hydrophobic pore structure generation mainly causes the difference in performance. However, exploring the internal pore structure should be supplemented in future test plans using FIB-SEM to explain the factors affecting performance more comprehensively.

Therefore, comparing the calculation results and experimental data, the decreased water permeability slopes are reasonable in the experiment because the experimental data only indicated the initial and transient slopes, which resulted from the distribution of the hydrophilic and hydrophobic pores in the composite MPL. If the water supply pressure could be increased as high as possible, the third slop of water permeability would be obtained.

While the above results have identified the best method for making composite MPLs, whether there is a difference in the actual internal pore structure cannot be further confirmed. However, it is believed that the separate hydrophilic and hydrophobic pore structure generation mainly causes the difference in performance. However, exploring the internal pore structure should be supplemented in future test plans using FIB-SEM to explain comprehensively the factors affecting performance.

4.3.3.3 The Relative Oxygen Permeance of MPLs with Different Mixing Methods

Figure 4.10 illustrates the relative oxygen permeance k_{O2} values obtained with the hydrophobic MPL (20%PVDF), hydrophilic MPL (7.5%Nafion-2.5%TiO_2), and composite MPLs (10%PVDF-7.5%Nafion-2.5%TiO_2) prepared with the separate mixing and premixing methods. The k_{O2} parameter effectively characterizes the ratio of pores with accumulated liquid water to the total pores. The hydrophobic MPL (20%PVDF) maintained nearly half of the entire pore space for oxygen diffusion. The hydrophilic MPL (7.5%Nafion-2.5TiO_2) absorbed water into almost all available pores due to its relatively strong hydrophilicity, leaving no pores for gas diffusion. Consequently, the k_{O2} was nearly zero. In the case of the composite MPL (10%PVDF-7.5%Nafion-2.5%TiO_2) with a separate mixing method, hydrophilic pores retained most liquid water while maintaining the hydrophobic pores for oxygen pathways. In the case of the composite MPL with the premixing method, weak hydrophobic pores increased liquid water pathways, resulting in a comparatively lower k_{O2} value.

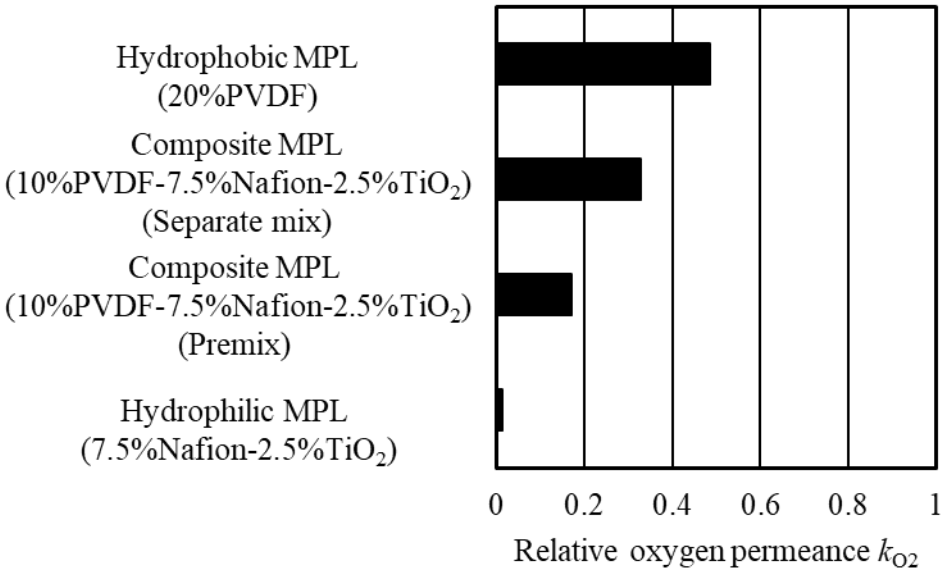

Figure 4.10 The relative oxygen permeance after the water permeability test for the hydrophobic MPL (20%PVDF), hydrophilic MPL (7.5%Nafion-2.5%TiO_2), and composite MPL (10%PVDF-7.5%Nafion-2.5%TiO_2) prepared with separate mixing and premixing methods.

4.3.3.4 The Oxygen Transport Resistance of MPLs with Different Mixing Methods

Figure 4.11 shows the R_{total} obtained with the hydrophobic MPL (20%PVDF), hydrophilic MPL (7.5%Nafion-2.5%TiO_2), and composite MPLs (10%PVDF-7.5%Nafion-2.5%TiO_2) prepared with separate mixing and premixing methods. In the case of the composite MPL with the separate mixing method, the hydrophilic pores were responsible for liquid water transportation from the catalyst layer to the GDL substrate. In contrast, the hydrophobic pores were kept for oxygen diffusion, significantly reducing the oxygen transport resistance. In the case of the composite MPL prepared with the premixing method, hydrophobic and hydrophilic pores were not separately generated. Thus, the R_{total} obtained for the composite MPL with the premixing method was higher than that for the hydrophobic MPL (20%PVDF).

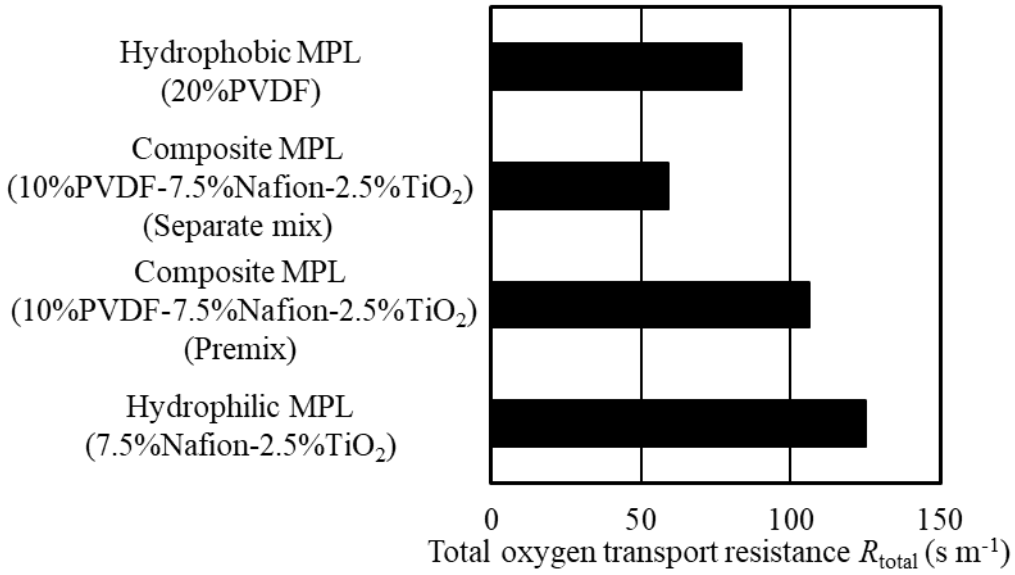

Figure 4.11 The total oxygen transport resistances obtained with hydrophobic MPL (20%PVDF), hydrophilic MPL (7.5%Nafion-2.5%TiO_2), and composite MPL (10%PVDF-7.5%Nafion-2.5%TiO_2) prepared with separate mixing and premixing methods under conditions of 200%RH, supplied gas flow rate of 1000 cm^3 min^{-1} and cell temperature of 35 °C.

4.3.4 Effect of TiO_2 Content in Composite MPL with PVDF, Nafion and TiO_2

Figure 4.12 shows the surface contact angles of the hydrophobic MPLs, hydrophilic MPLs, and composite MPLs with different ingredients. Single MPLs were explicitly prepared to assess the impact of the hydrophobicity and hydrophilicity in the composite MPLs on the surface contact angle. These hydrophilic MPLs were formulated using the same hydrophilic compositions of the composite MPLs described in Table 4.1.

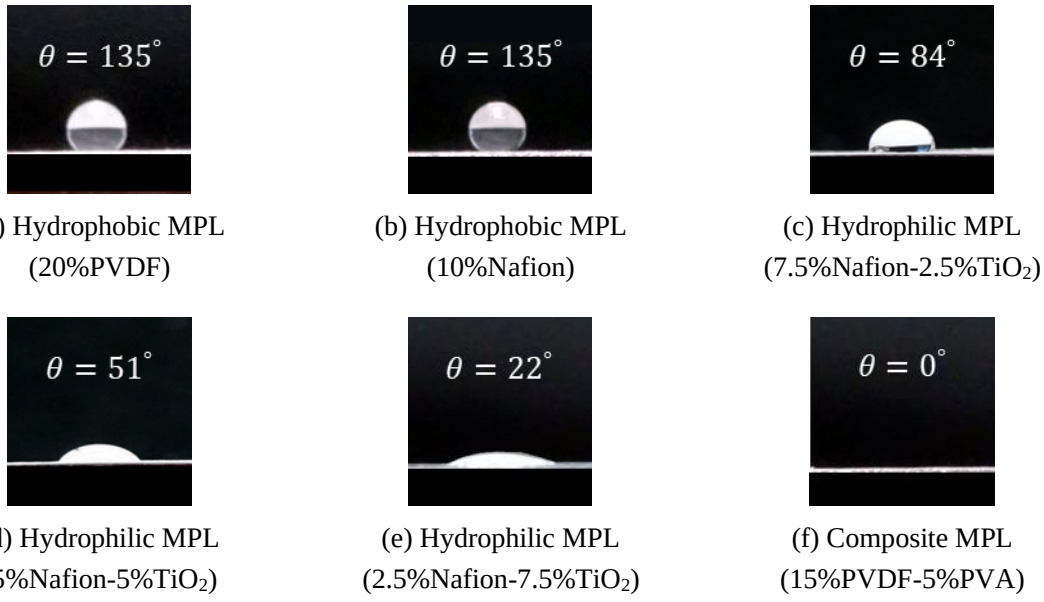

(a) Hydrophobic MPL (20%PVDF)
(b) Hydrophobic MPL (10%Nafion)
(c) Hydrophilic MPL (7.5%Nafion-2.5%TiO_2)
(d) Hydrophilic MPL (5%Nafion-5%TiO_2)
(e) Hydrophilic MPL (2.5%Nafion-7.5%TiO_2)
(f) Composite MPL (15%PVDF-5%PVA)

Figure 4.12 Surface contact angles of hydrophobic MPLs, hydrophilic MPLs, and composite MPLs with different ingredients.

The PVDF was selected as a hydrophobic binder to coordinate the same sintering temperature of 150°C as that of the PVA binder. The MPL (20%PVDF) presented the same θ value as that of MPL (20%PTFE) shown in Figure 4.1(a). The composite MPL (15%PVDF-5%PVA) exhibited strong hydrophilicity, which presented hydrophilicity similar to the hydrophilic MPL (5%PVA) shown in Figure 4.12(b). Therefore, PEFC performance was not enhanced due to the aggravating liquid water accumulation at the CL and MPL. Thus, the PVA was not an appropriate hydrophilic binder for the composite MPL design.

The Nafion binder, having a 150°C sintering temperature, was chosen as the weak hydrophobic binder. As for Nafion, the MPL (10%Nafion) exhibited a high contact angle value, which revealed the same contact angle as that observed for the hydrophobic MPL (20%PVDF). The MPL with Nafion displayed strong hydrophobic characteristics due to the effect of PTFE-

backbone structures in Nafion, as shown in Chapter 2. To further modify the hydrophilicity of the composite MPL, the hydrophilic TiO_2 particles were introduced into the PVDF-Nafion composite MPL. When the TiO_2 content increased from 2.5% to 7.5%, the surface contact angle decreased from 84° to 22°, signifying a gradual transition toward hydrophilicity.

Figure 4.13 indicates the I-V curves and IR overpotentials of several tested samples.

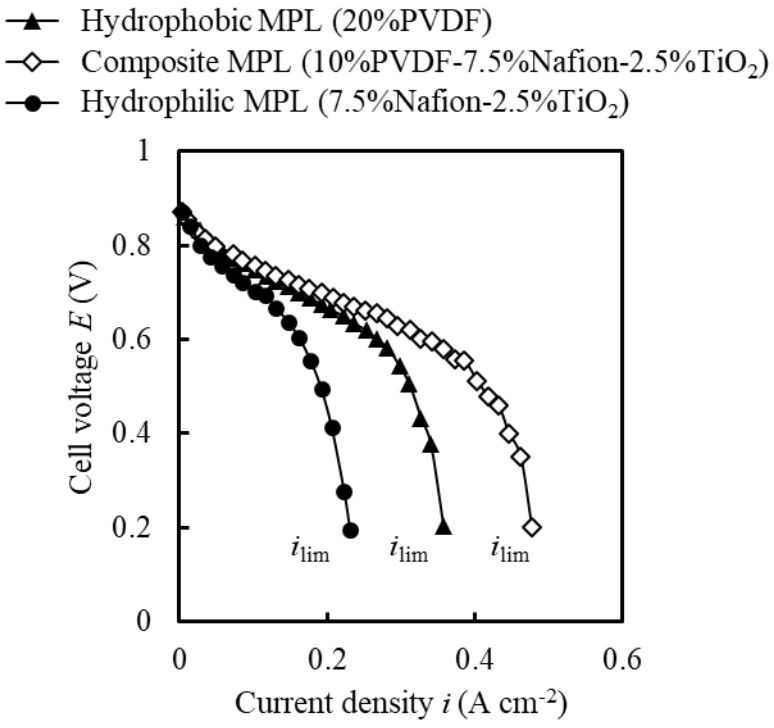

(a) Polarization curves

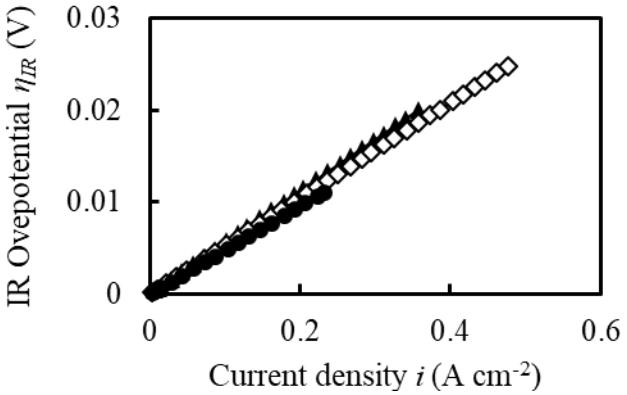

(b) IR overpotentials.

Figure 4.13 Polarization curves and IR overpotentials obtained with single MPL and composite MPL coated GDLs with different preparation methods under conditions of 2% oxygen concentration, 200%RH, a back pressure of 101 kPa abs, a supplied gas flow rate of 1000 cm^3 min^{-1}, and a 35 °C cell temperature.

According to the i_{lim}, Figure 4.14 indicates the effects of the TiO_2 content in the composite MPL containing PVDF, Nafion, and TiO_2 on the R_{total} value based on the Eq. (2.7). The

composite MPL (10%PVDF-10%Nafion) without TiO_2 could not improve the performance compared with hydrophobic MPL (20%PVDF). Adding the hydrophilic TiO_2 to the composite MPL effectively reduced the R_{total}. The lowest R_{total} was obtained with the composite MPL (10%PVDF-7.5%Nafion-2.5%TiO_2). Consequently, implementing an appropriate composite MPL coated GDL effectively reduced oxygen transport resistance under high humidity conditions. This composite MPL contained distinct hydrophobic and hydrophilic pores, synergistically facilitating efficient gas diffusion and water transportation. Specifically, appropriate hydrophilic pores facilitated water discharge from the catalyst layer. As a result, water accumulation was alleviated, enhancing gas diffusion toward the catalyst layer. However, when excessive TiO_2 was added to the composite MPL, the gradually reinforced hydrophilicity led to worse performance and presented the highest R_{total} for the composite MPL (10%PVDF-2.5%Nafion-7.5%TiO_2). Strong or weak hydrophilicity could not provide the appropriate water transport ability to expel water from the interface between the catalyst layer and MPL to reduce oxygen transport resistance.

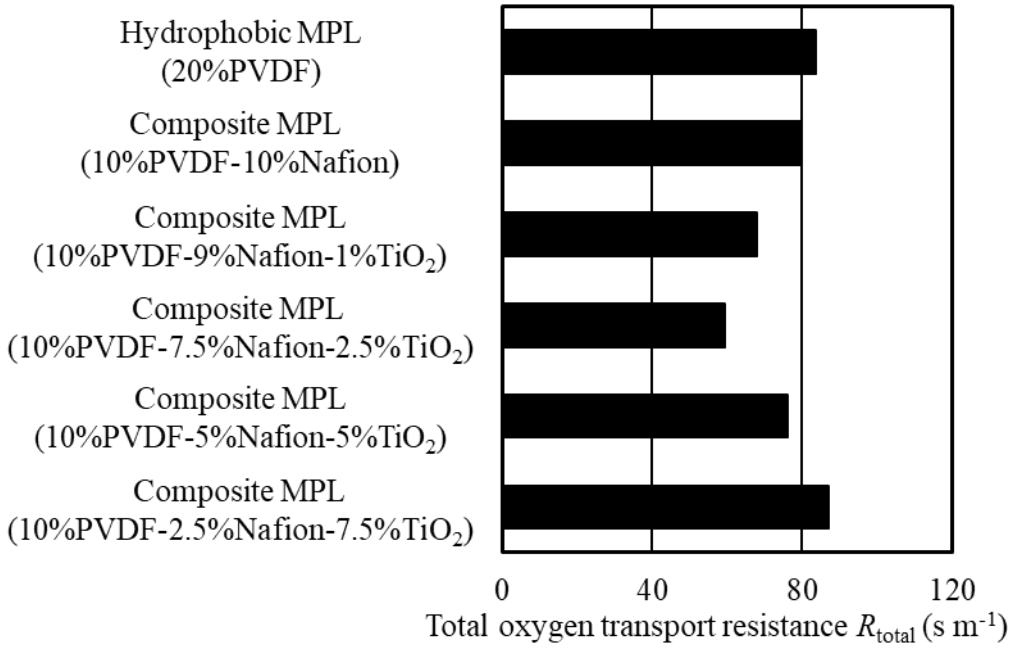

Figure 4.14 The total oxygen transport resistances obtained with hydrophobic MPL (20%PVDF) and composite MPL (PVDF-Nafion-TiO_2) with different hydrophilic compositions under conditions of 200%RH, supplied gas flow rate of 1000 cm^3 min^{-1} and cell temperature of 35 °C.

4.3.5 Effect of Composite MPL Coated GDL on Pressure-dependent and Pressure-independent Resistances

Figure 4.15 summarizes the relationship between the oxygen partial pressure p_{O2} and the limiting current density i_{lim} under various back pressure conditions when composite MPL coated GDL was applied to obtain the average R_{total} [57,59]. The assessment of the composite MPL coated GDL effectiveness involved the examination of R_p and R_{np}, both components separated from the R_{total} as defined in Eq. (2.7) and is shown in Figure 4.16. Performance enhancement obtained with the composite MPL coated GDL was considered by the pressure-independent resistance R_{np}, and the pressure-dependent resistance R_p was separated from the total oxygen transport resistance R_{total}.

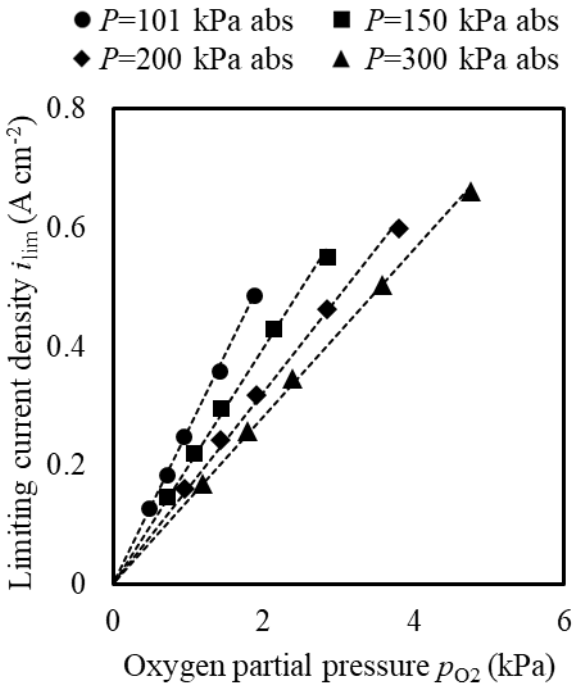

Figure 4.15 Relationship between the limiting current density and oxygen partial pressure obtained with a composite MPL coated GDL (10%PVDF-7.5%Nafion-2.5%TiO_2) at different back pressures under 200 %RH, supplied gas flow rate of 1000 cm^3 min^{-1} and cell temperature of 35 °C.

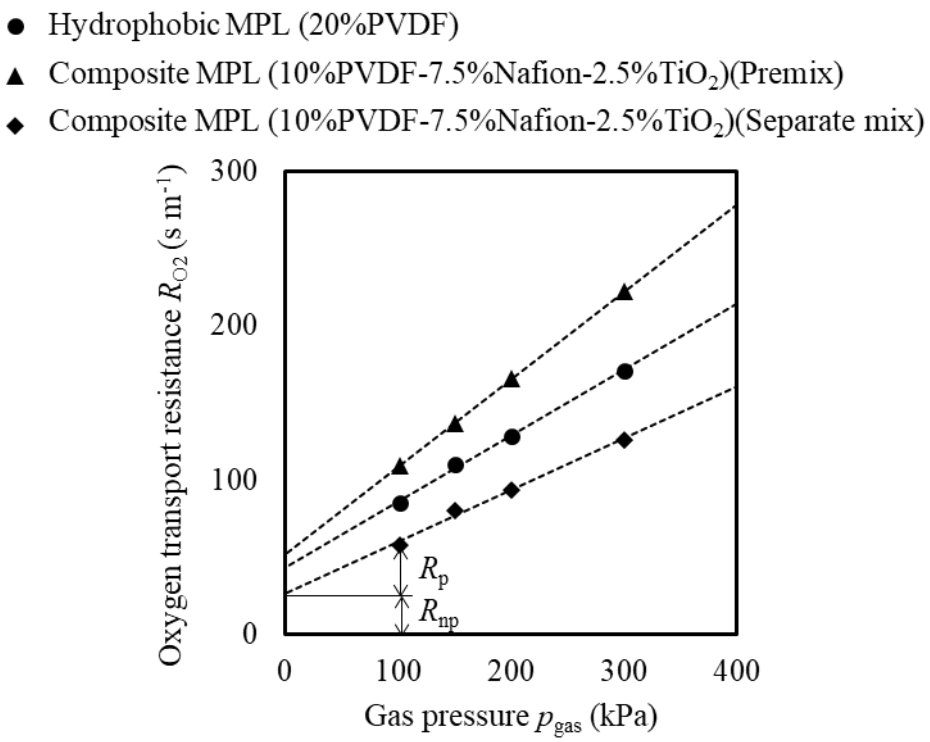

Figure 4.16 The pressure-dependent and pressure-independent resistances separated from the total oxygen transport resistance obtained with hydrophobic MPL (20%PVDF) and composite MPL (10%PVDF-7.5%Nafion-2.5%TiO_2) prepared with separate mixing and premixing methods at different back pressures under 200 %RH, supplied gas flow rate of 1000 cm^3 min^{-1} and cell temperature of 35 °C.

Figure 4.17 presents these values obtained with the hydrophobic MPL (20%PVDF) and composite MPLs (10%PVDF-7.5%Nafion-2.5%TiO_2) prepared with separate mixing methods were analyzed under various pressure p_{gas} conditions at 200%RH and 35°C cell temperature. When the cell operated near the i_{lim}, the flooding became severe, and liquid water transport ability significantly varied through the properties. For the hydrophobic MPL (20% PVDF) coated GDL, the excess liquid water mainly passes through the large pores generated in the hydrophobic MPL with relatively low capillary pressures. However, the water expelling ability could not meet the demand to further reduce the amount of the accumulated liquid water at the interface between the catalyst layer and the MPL, which reduced oxygen supply to the catalyst layer and increased the R_{np}.

The composite MPL with the separate mixing method exhibited a noteworthy reduction in the R_{np} and R_n values compared to those obtained with the hydrophobic MPL (20%PVDF). The hydrophilic pores enhanced the ability of the MPL to discharge excess water at the catalyst layer while maintaining oxygen pathways in the hydrophobic pores. Conversely, the composite

MPL with the premixing method did not enhance performance due to the uniform formation of mild hydrophobic pores. The reduced hydrophobicity increased the number of pores as potential water pathways, allowing excessive water accumulation in the catalyst layer and the MPL. Meanwhile, the limited empty pores were insufficient to supply abundant oxygen to the catalyst layer. Consequently, this disrupted the delicate balance between water and oxygen diffusion, elevating the R_{np} and R_n values under low and high humidity conditions.

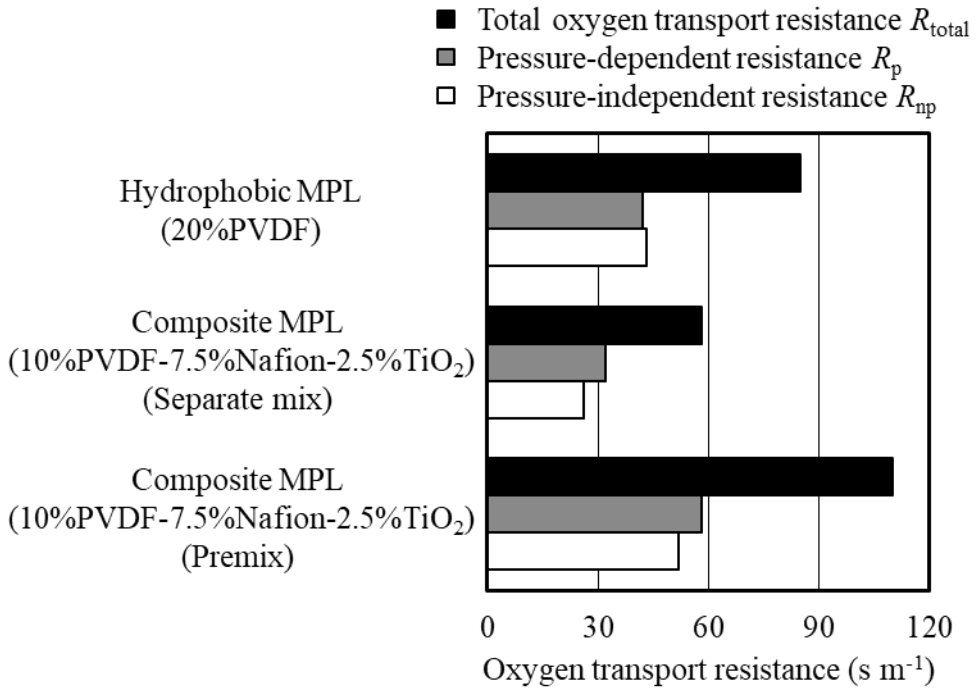

Figure 4.17 The pressure-dependent and pressure-independent oxygen transport resistances in the total oxygen transport resistance obtained with hydrophobic MPL (20%PVDF) and composite MPL (10%PVDF-7.5%Nafion-2.5%TiO_2) prepared with separate mixing and premixing methods under conditions of 200 %RH, a back pressure of 101 kPa, supplied gas flow rate of 1000 cm^3 min^{-1} and cell temperature of 35 °C.

The previous work demonstrated that a double MPL in Figure 4.18(a), in which a hydrophilic MPL (5%Nafion-25%TiO_2) was coated on the hydrophobic MPL coated GDL, decreased the R_{total} to 70 s m^{-1} in Chapter 3. An appropriate composite MPL could form a more balanced distribution of hydrophilic and hydrophobic pores within the MPL by connecting CL and substrate, which enhanced the ability of the MPL to expel excess water from the catalyst layer and without oxygen transport blockage in Figure 4.18(b), further reducing the R_{total} below 60 s m^{-1} under high humidity conditions.

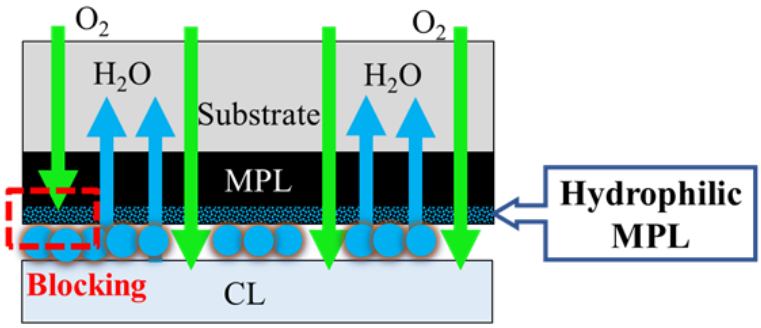

(a) Double MPL coated GDL

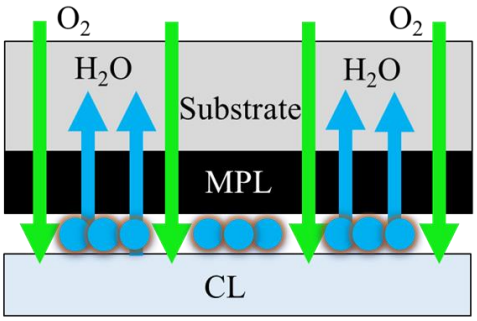

(b) Composite MPL coated GDL

Figure 4.18 The schematic diagram of the water transport from the substrate to the CL in the cathode when applied (a) double MPL coated GDL and (b) composite MPL coated GDL.

5. The Comparison Between Commercial, Double, and Composite MPL coated GDLs

After assessing both double MPL and composite MPL coated GDLs, it becomes imperative to ascertain their capability to meet the performance requirements. Equally crucial is determining whether our in-house novel MPL coated GDLs can outperform the standard commercial MPL coated GDL, represented by the SGL 22BB (SIGRACET®), a widely used product in industries. The schematic diagrams of the SGL 22BB, double MPL, and composite MPL coated GDLs are shown in Figure 5.1 to help readers easily understand the configurations of these samples. The SGL 22BB, with a thickness of 215 μm, incorporates a hydrophobic MPL containing 20% PTFE and 5% PTFE-treated carbon paper. Notably, the maximum pore size of the SGL 22BB was measured to be larger than 40 μm. Besides, it is also necessary to compare the R_p of tested MPLs to NEDO demanded target value of 18 s m^{-1} in 2030 under 100 kPa abs, 80%RH with a cell temperature of 80°C.

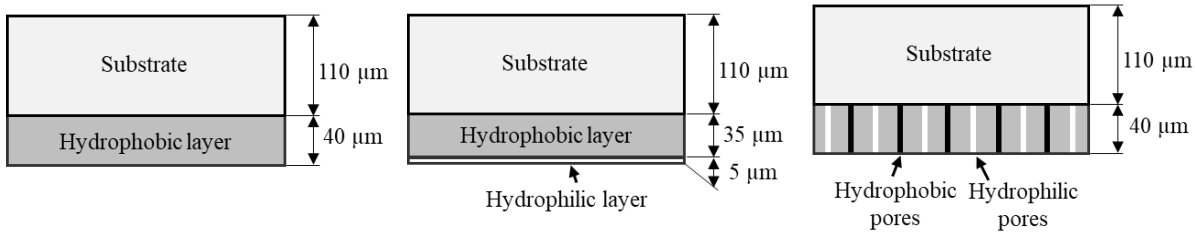

(a) SGL 22BB (b) Double MPL (c) Composite MPL

Figure 5.1 The schematic diagrams of the SGL 22BB, double MPL, and composite MPL.

5.1 The Oxygen Transport Resistances Comparison with Low Oxygen Concentration under High Water Saturation Conditions and Normal Conditions

In this context, the separation tests were broadened to encompass normal conditions (80%RH, T_{cell} =80°C) for the novel MPL coated GDLs. Simultaneously, measurements were conducted under highly saturated conditions (200%RH, T_{cell} =35°C) and normal conditions for the SGL 22BB. The comparative results for all gas pressure conditions across the three samples

are outlined in the detailed breakdown of R_p, R_{np}, and R_{total} for the three samples under high saturated and normal conditions, presented in Figure 5.2(a) and (b).

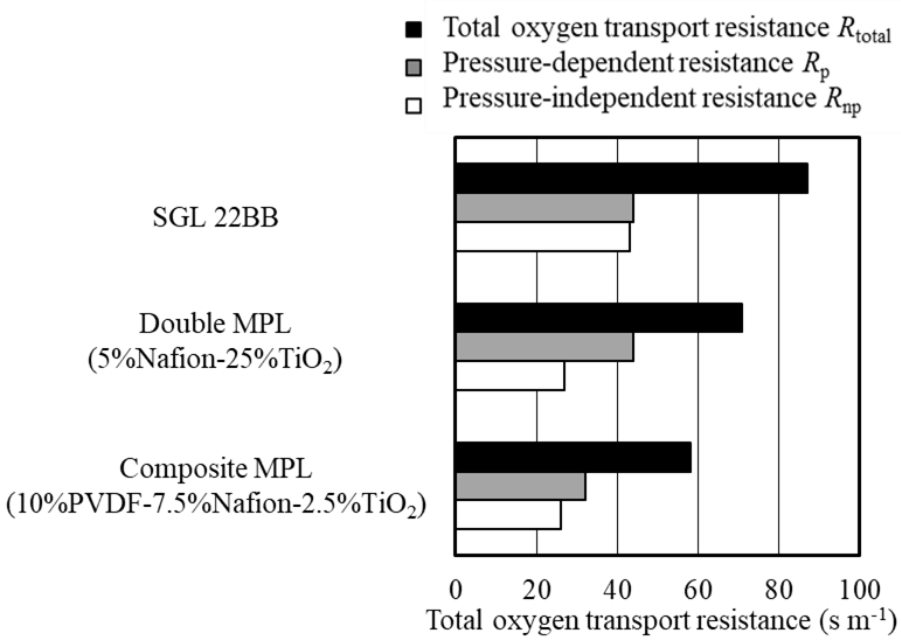

(a) Under 200 %RH and a 35 °C cell temperature.

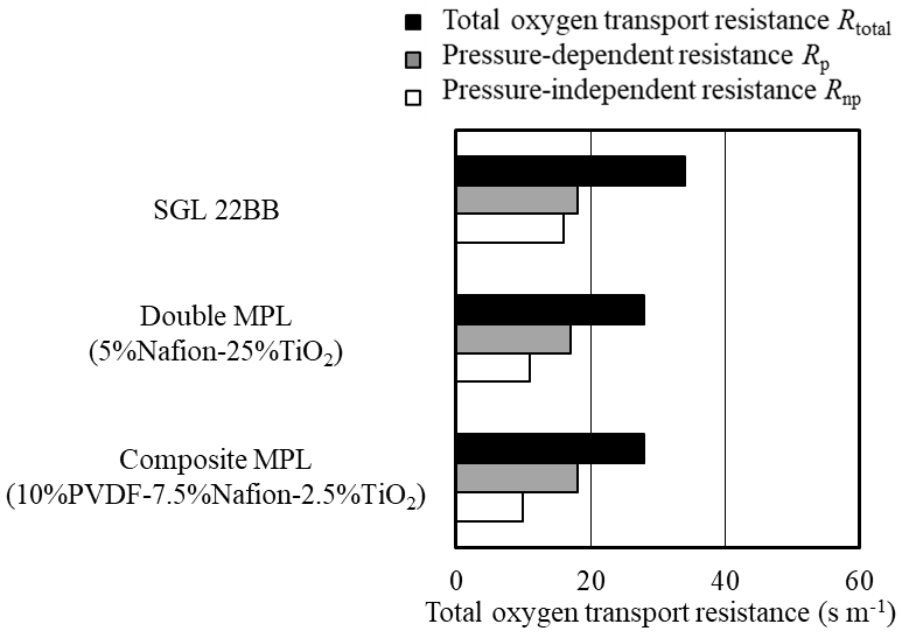

(b) Under 80%RH and an 80 °C cell temperature.

Figure 5.2 The pressure-dependent and pressure-independent oxygen transport resistances in the total oxygen transport resistance obtained from single MPL, double MPL, and composite MPL coated GDLs with a supplied gas flow rate of 1000 cm^3 min^{-1}, under (a) 200 %RH and a 35 °C cell temperature, and (b) 80%RH and an 80 °C cell temperature, respectively.

In both high saturated and normal conditions depicted in Figure 5.2(a) and (b), SGL 22BB consistently exhibited high values of R_{np} and R_p. This high resistance is attributed to its strong

hydrophobicity, which hinders liquid water transport from the CL and MPL interface to the channels during flooding incidents. Introducing a thin hydrophilic MPL in the double MPL coated GDL resulted in lower R_{np} and R_p than the 22BB. The hydrophilic layer played a role in transporting water into the hydrophobic pores, enhancing the expulsion of water to the channels. However, despite the improved water expulsion compared to the hydrophobic 22BB, the hydrophilic layer could not directly transport water to the substrate. The uniform hydrophilicity in the hydrophilic layer inevitably partially impeded oxygen transport in some hydrophobic pores after water absorption, preventing a further reduction in the R_{total}.

In contrast to the double MPL, the performance improvement was achieved by reorganizing the hydrophilic and hydrophobic structures in the composite MPL coated GDL, resulting in a similar R_{np} but significantly lower R_p than the double MPL. This enhancement can be attributed to a more effective arrangement of hydrophilic and hydrophobic structures. Hydrophilic pores directly connect the CL and MPL interface and the substrate rather than connect the CL/MPL interface to the hydrophobic layer in the double MPL. Consequently, the composite MPL coated GDL achieved more efficient water transport by utilizing connected pores to mitigate flooding, as evidenced by lower R_p values under all conditions. Furthermore, the introduction of artificially constructed water transport pathways ensured that water transport did not impede gas transport in hydrophobic pores. Once an optimal balance between gas and water transport was established, the composite MPL coated GDL exhibited significantly improved performance compared to the double MPL coated GDL.

After evaluating the performance of the SGL 22BB, double MPL, and composite MPL, a detailed analysis of R_p and R_{np} under 101 kPa absolute pressure, as well as under high saturated and normal conditions, under high saturated conditions (200%RH, T_{cell}=35°C), the R_p and R_{np} of 22BB were 44 s m^{-1} and 43 s m^{-1}, respectively. The double MPL showed the same R_p as 22BB but a lower R_{np} of 27 s m^{-1}, while the composite MPL exhibited the lowest R_p of 32 s m^{-1} and R_{np} of 26 s m^{-1}.

Under normal conditions (80%RH, T_{cell} =80°C), the R_{np} of 22BB was 18 s m^{-1}, and R_p was 16 s m^{-1}. The double MPL indicated a slightly lower R_p of 17 s m^{-1} and significantly reduced R_{np} to 11 s m^{-1} than the SGL 22BB [86]. The composite MPL coated GDL showed an R_p of 18 s m^{-1} and a further reduction in R_{np} of 10 s m^{-1}.

Hence, when comparing the two types of novel MPL coated GDLs, it becomes evident that the composite MPL coated GDL outperforms the double MPL coated GDL, showcasing notably superior performance to the widely utilized commercial SGL 22BB. This observation underscores the effectiveness of the developed composite MPL in mitigating flooding under both highly saturated and normal conditions, achieved through its specially designed structure. Simultaneously, the newly designed double layer and composite MPL exhibit low molecular diffusion resistance under normal conditions, aligning with the anticipated molecular diffusion indicators outlined in the NEDO roadmap. Furthermore, compared to the 22BB, the novel MPL significantly reduces Knudsen diffusion resistance, further enhancing overall performance.

5.2 The I-V Characteristic Curves Comparison with High Oxygen Concentration under Normal Conditions

Following an evaluation conducted under low oxygen concentration conditions, Figure 5.3 illustrates the results of the I-V characteristic test carried out by NEDO under high cell temperature and full air supply conditions. A comparison is made between the I-V curves of Toray MPL (XGL) used in the commercial fuel cell vehicle and an in-house composite MPL coated GDL. The experiments were conducted under 150 kPa abs, with the flow rate set at 400 cm^3 min^{-1} for both the anode and cathode. The oxygen concentration was maintained at 21%, and relative humidities were controlled at 80%RH when the cell temperature was set at 80°C.

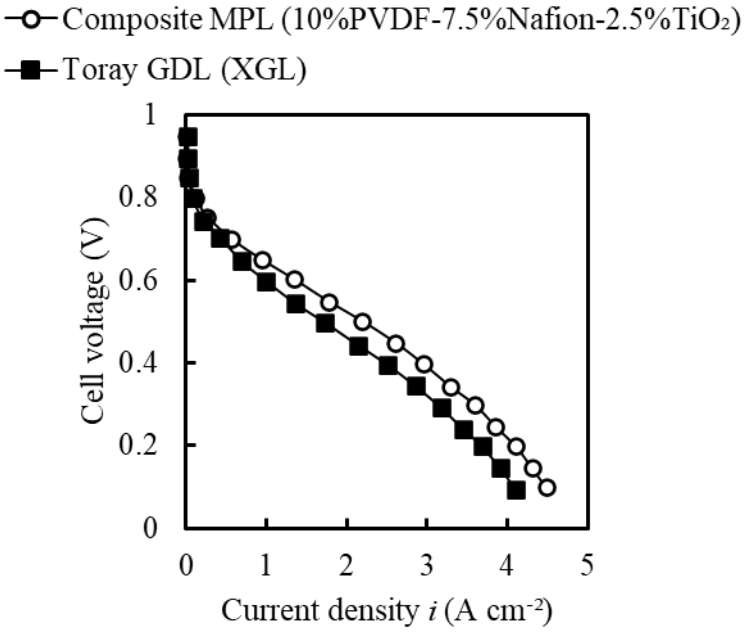

Figure 5.3 The I-V characteristic curves tests of Toray MPL (XGL) and composite MPL coated GDLs with a supplied gas flow rate of 400 cm^3 min^{-1} with 21% O_2, under (a) 40 %RH and an 80 °C cell temperature and (b) 80%RH and an 80 °C cell temperature, respectively.

Figure 5.3 shows that the composite MPL presented higher performance than the hydrophobic MPL (Toray XGL), particularly at 3 A cm^{-2} from the NEDO target requirement. At this evaluation point, the cell voltage of the composite MPL was at around 0.4 V, indicating an approximately 27% improvement over the hydrophobic MPL (Toray XGL).

In summary, whether under supersaturated conditions or normal humidity conditions, the composite MPL achieves enhanced performance, effectively strengthening the robustness regardless of the humidity variations.

6. Conclusion and Future Prospects

An effective water management strategy in the PEFC should have the dual objectives of preventing dehydration of the MEA by utilizing water generated by electrochemical reactions in normal conditions while also expelling excess water from the CL. This approach helps maintain gas diffusion, thus reducing concentration overpotential during high humidity and normal conditions.[1-5] The MPLs are crucial in promoting water removal from the catalyst layer under high humidity conditions and preventing membrane dehydration under low humidity conditions. The transmission of liquid water and oxygen can be effectively improved by improving the hydrophilic and hydrophobic behavior and design parameters of the MPL. This dissertation comprehensively overviews the development stages, design parameter testing, and performance evaluation methods and outcomes for MPL coated GDL. The study primarily focuses on designing and developing two novel MPL coated GDL structures: a double MPL and a composite MPL. Extensive characteristic tests and performance assessments revealed that the double layer and composite MPL coated GDLs outperform traditional hydrophobic MPL and commercial SGL 22BB. The ensuing conclusions are drawn based on the obtained test results.

Chapter 1 mainly describes the background of the hydrogen-utilized PEFC system and elaborates on the working principle and overpotentials. Moreover, the different MPL modification methods were compared, and the visualization and simulation proved the importance of water management in the cell.

Chapter 2 elucidated the design parameter testing and performance evaluation methods and apparatuses.

Chapter 3 focused on the double MPL coated GDL development. The double MPL incorporated a thin hydrophilic MPL and hydrophobic MPL coated GDL. Initially, the hydrophilic and hydrophobic properties of the double MPL were assessed using the sessile drop method. This allowed for adjusting the hydrophilic MPL characteristics based on the measured surface contact angle, ensuring a tuning of hydrophilic and hydrophobic properties. According to the surface contact angle, the hydrophilic layer employing a Nafion binder initially exhibited unexpected hydrophobicity, necessitating the addition of TiO_2 to enhance its

hydrophilic properties. Water treatment became imperative for accurately determining the water breakthrough pressure in the MPL containing Nafion post-sintering at high temperatures. Because the Nafion binder lost water molecules during the preparation, water treatment can rebuild the water pathways, evaluating the real property of Nafion. After water treatment, the resulting in-pore contact angle, derived from the water breakthrough pressure, depicted the difference before and after water treatment and also found a decrease as the TiO_2 content in the hydrophilic layer increased. In the context of the double MPL, the hydrophilic layer played a crucial role in facilitating the introduction of liquid water into the hydrophobic MPL pores. This enhancement improved the capacity to expel excess water from the catalyst layer, thereby reducing pressure-independent oxygen transport resistance. Specifically, the optimal hydrophilic MPL composition (5% Nafion-25% TiO_2) within the double MPL demonstrated a noteworthy 20% reduction in oxygen transport resistance compared to a conventional hydrophobic MPL under high saturated conditions. Conversely, in the scenario of the hydrophilic layer utilizing a PVA binder, the robust hydrophilicity resulted in significant water accumulation in both the catalyst layer and the MPL. This accumulation obstructed oxygen transport, leading to elevated pressure-independent and pressure-dependent resistances, substantially increasing the total oxygen transport resistance.

Chapter 4 delves into developing the innovative composite MPL coated GDL. Unlike the hydrophobic and hydrophilic MPL configurations in the double MPL, the composite MPL seamlessly integrates hydrophilic and hydrophobic pores within the same layer, necessitating distinctive preparation methods. The composite MPL, crafted by mixing hydrophilic and hydrophobic slurries, effectively generates both pores. Water permeability was a crucial metric to ascertain the separate generation of hydrophobic and hydrophilic pores. The meticulously crafted composite MPL, characterized by a low water breakthrough pressure, exhibited two distinct increasing slopes of water permeability, a departure from the single slope of the conventional single MPL. The relative oxygen permeance is employed to assess oxygen transportability when the sample absorbs liquid water under specific pressure conditions, demonstrating the desired dual function of gas-liquid transport balance in the assembled composite MPL. Sintering the composite MPL at 350°C with PTFE and PVA binders results in PVA burning, yielding performance akin to the hydrophobic MPL. Conversely, a lower

sintering temperature of 150°C induces strong hydrophilicity in the MPL, causing a significant degradation in performance. The composite MPL using PVDF and Nafion binders at a sintering temperature of 150°C fails to achieve performance enhancement due to Nafion exhibiting hydrophobicity influenced by PTFE-backbone structures. To introduce hydrophilicity, it becomes imperative to incorporate hydrophilic TiO_2 particles into the Nafion binder. Through the adjustment of the proportion of hydrophilic material ingredients and extensive performance testing, the optimal composite MPL, comprising 10% PVDF, 7.5% Nafion, and 2.5% TiO_2, demonstrates a substantial reduction in total oxygen transport resistance under high saturated conditions, notably lowering pressure-independent oxygen transport resistance compared to that obtained with the hydrophobic MPL.

In Chapter 5, the test conditions for oxygen diffusion resistance were expanded to include high-temperature normal conditions. The primary focus was comparing the oxygen transport resistance of the two novel samples and a commercial hydrophobic sample, along with evaluating Knudsen diffusion and molecular diffusion resistances after separation. The double MPL and composite MPL demonstrated the ability to reduce total oxygen diffusion resistance under both high saturated and normal conditions compared to the commercial sample SGL 22BB. These novel MPLs effectively mitigated Knudsen diffusion and molecular diffusion resistance, indicating their efficacy in reducing flooding compared to the hydrophobic SGL 22BB. Further analysis revealed that, under high saturated and normal conditions, although the composite MPL exhibited a Knudsen diffusion resistance similar to the double MPL, it further reduced molecular diffusion resistance. Consequently, it effectively alleviated flooding at the interface of the CL and MPL, resulting in a lower total oxygen diffusion resistance. This outcome highlighted that the composite MPL brought a more rational gas-liquid transport function with its hydrophilic and hydrophobic pore structure settings. Under normal conditions, SGL 22BB demonstrated a molecular diffusion resistance value comparable to the expected value. At the same time, both the double MPL and the composite MPL exhibited resistance values below the commercial SGL 22BB.

In summary, whether under highly saturated or normal conditions, the design of the microporous layer plays a crucial role in mitigating the flooding phenomenon in PEFC. Reasonable microporous layer design can effectively promote the elimination of liquid water

while ensuring the transmission of reactant gases, thereby reducing the power output limitations caused by overflow. Proper introduction of hydrophilic properties in an appropriate manner into traditionally hydrophobic samples can facilitate liquid water transport. In this study, a new composite microporous layer with excellent performance, the composite MPL, emerges as a promising design with significant potential, suggesting that future developments in MPL coated GDL should build upon this innovative design.

After identifying composite samples with excellent performance, future research can focus on developing new MPL coated GDL based on the substrate. It is important to note that this dissertation did not delve into modifications involving different types of substrates. Thus, future studies, especially those exploring the self-standing microporous layer (SSMPL), should be introduced to address this gap. Figure 6.1 illustrates the present composite MPL and the future design plan for the SSMPL. The current composite MPL was coated on carbon paper with a thickness of 110 μm. Presently available commercial carbon mesh can significantly reduce the thickness to 40 μm. In the envisioned application of carbon mesh as the backbones for the composite MPL, the composite slurry would adhere to the carbon mesh, creating a smooth surface with an estimated thickness lower than 100 μm. The SSMPL holds the potential to effectively mitigate ohmic overpotential and high thermal conductivity issues associated with substrate thickness, given its capability to be produced in extremely thin dimensions [93,112-115]. Therefore, the cell performance could be further improved when the composite MPL coated carbon mesh is applied.

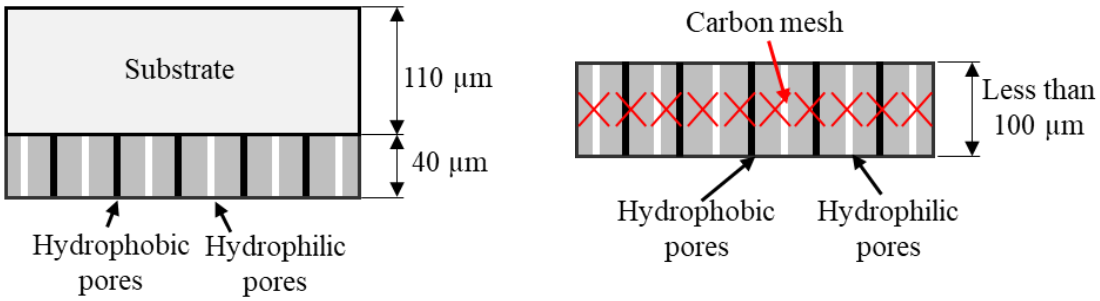

(a) Composite MPL coated GDL (b) Self-standing composite MPL

Figure 6.1 The schematic diagram of the (a) present composite MPL coated GDL and (b) future design self-standing composite MPL.

Reference

[1] E. Kötter, L. Schneider, F. Sehnke, K. Ohnmeiss, R. Schröer, The future electric power system: Impact of Power-to-Gas by interacting with other renewable energy components, Journal of Energy Storage. 5 (2016) 113–119. https://doi.org/10.1016/j.est.2015.11.012.

[2] D. Gielen, F. Boshell, D. Saygin, M.D. Bazilian, N. Wagner, R. Gorini, The role of renewable energy in the global energy transformation, Energy Strategy Reviews. 24 (2019) 38–50. https://doi.org/10.1016/j.esr.2019.01.006.

[3] B.G. Pollet, I. Staffell, J.L. Shang, Current status of hybrid, battery and fuel cell electric vehicles: From electrochemistry to market prospects, Electrochimica Acta. 84 (2012) 235–249. https://doi.org/10.1016/j.electacta.2012.03.172.

[4] L. Mihet-Popa, S. Saponara, Toward Green Vehicles Digitalization for the Next Generation of Connected and Electrified Transport Systems, Energies. 11 (2018) 3124. https://doi.org/10.3390/en11113124.

[5] G. Avgouropoulos, T. Ioannides, J.K. Kallitsis, S. Neophytides, Development of an internal reforming alcohol fuel cell: Concept, challenges and opportunities, Chemical Engineering Journal. 176–177 (2011) 95–101. https://doi.org/10.1016/j.cej.2011.05.094.

[6] A.N. Fatsikostas, Dimitris.I. Kondarides, X.E. Verykios, Production of hydrogen for fuel cells by reformation of biomass-derived ethanol, Catalysis Today. 75 (2002) 145–155. https://doi.org/10.1016/S0920-5861(02)00057-3.

[7] P. Moriarty, D. Honnery, Intermittent renewable energy: The only future source of hydrogen?, International Journal of Hydrogen Energy. 32 (2007) 1616–1624. https://doi.org/10.1016/j.ijhydene.2006.12.008.

[8] J. Andrews, B. Shabani, Re-envisioning the role of hydrogen in a sustainable energy economy, International Journal of Hydrogen Energy. 37 (2012) 1184–1203. https://doi.org/10.1016/j.ijhydene.2011.09.137.

[9] H. Heidary, A. El-Kharouf, R. Steinberger-Wilckens, S. Bozorgmehri, M. Salimi, M. Golmohammad, Life cycle assessment of solid oxide fuel cell vehicles in a natural gas producing country; comparison with proton electrolyte fuel cell, battery and gasoline vehicles, Sustainable Energy Technologies and Assessments. 59 (2023) 103396. https://doi.org/10.1016/j.seta.2023.103396.

[10] I.-S. Sorlei, N. Bizon, P. Thounthong, M. Varlam, E. Carcadea, M. Culcer, M. Iliescu, M. Raceanu, Fuel Cell Electric Vehicles—A Brief Review of Current Topologies and Energy Management Strategies, Energies. 14 (2021) 252. https://doi.org/10.3390/en14010252.

[11] R. O'Hayre, S. W. Cha, W. Colella, and F. B. Prinz, Fuel Cell Fundamentals, p. 256, John Wiley & Sons, New York, (2016).

[12] S. T. Thompson, B. D. James, J. M. Huya-Kouadio, C. Houchins, D. A. DeSantis, R. Ahluwalia, A. R. Wilson, G. Kleen, and D. Papageorgopoulos, Direct hydrogen fuel cell electric vehicle cost analysis: System and high-volume manufacturing description, validation, and outlook, J. Power Sources, 399, (2018). https://doi.org/10.1016/j.jpowsour.2018.07.100.

[13] Y. Li, F. Taghizadeh-Hesary, The economic feasibility of green hydrogen and fuel cell electric vehicles for road transport in China, Energy Policy, 160, (2022). https://doi.org/10.1016/j.enpol.2021.112703

[14] X. Liu, K. Reddi, A. Elgowainy, H. Lohse-Busch, M. Wang, N. Rustagi, Comparison of well-to-wheels energy use and emissions of a hydrogen fuel cell electric vehicle relative to a conventional gasoline-powered internal combustion engine vehicle, International Journal of Hydrogen Energy. 45 (2020) 972–983. https://doi.org/10.1016/j.ijhydene.2019.10.192.

[15] T. Yoshida, and K. Kojima, Toyota MIRAI fuel cell vehicle and progress toward a future hydrogen society. Electrochem. Soc. Interface, 24(2), 2015. https://iopscience.iop.org/article/10.1149/2.F03152if

[16] J. P. Braaten, N. N. Kariuki, and D. J. Myers, S. Blackburn, G. Brown, A. Park, and S. Litster, Integration of a high oxygen permeability ionomer into polymer electrolyte membrane fuel cell cathodes for high efficiency and power density, J. Power Sources, 522, (2022). https://doi.org/10.1016/j.jpowsour.2021.230821.

[17] D. A. Cullen, K. C. Neyerlin, R. K. Ahluwalia, R. Mukundan, K. L. More, R. L. Borup, A. Z. Weber, D. J. Myers, and A. Kusoglu. New roads and challenges for fuel cells in heavy-duty transportation. Nat Energy, 6, (2021). https://doi.org/10.1038/s41560-021-00775-z

[18] S. Hienuki, H. Mitoma, M. Ogata, I. Uchida, S. Kagawa, Environmental and energy life cycle analyses of passenger vehicle systems using fossil fuel-derived hydrogen, International Journal of Hydrogen Energy. 46 (2021) 36569–36580. https://doi.org/10.1016/j.ijhydene.2021.08.135.

[19] M. A. Delavar, and J. Wang, PEM Fuel Cells, p. 173, Elsevier, (2022). https://doi.org/10.1016/B978-0-12-823708-3.00010-9.

[20] K. Jiao, J. Xuan, Q. Du, Z. Bao, B. Xie, B. Wang, Y. Zhao, L. Fan, H. Wang, Z. Hou, S. Huo, N.P. Brandon, Y. Yin, M.D. Guiver, Designing the next generation of proton-exchange membrane fuel cells, Nature. 595 (2021) 361–369. https://doi.org/10.1038/s41586-021-03482-7.

[21] X.-Z. Yuan, C. Nayoze-Coynel, N. Shaigan, D. Fisher, N. Zhao, N. Zamel, P. Gazdzicki, M. Ulsh, K.A. Friedrich, F. Girard, U. Groos, A review of functions, attributes, properties and measurements for the quality control of proton exchange membrane fuel cell components, Journal of Power Sources. 491 (2021) 229540. https://doi.org/10.1016/j.jpowsour.2021.229540.

[22]Steele B C H, Heinzel A. Materials for fuel-cell technologies[J]. Nature, 2001, 414(6861): 345-352.

[23] T. Wilberforce, Z. El Hassan, E. Ogungbemi, O. Ijaodola, F.N. Khatib, A. Durrant, J. Thompson, A. Baroutaji, A.G. Olabi, A comprehensive study of the effect of bipolar plate (BP) geometry design on the performance of proton exchange membrane (PEM) fuel cells, Renewable and Sustainable Energy Reviews. 111 (2019) 236–260. https://doi.org/10.1016/j.rser.2019.04.081.

[24] S. Ott, A. Orfanidi, H. Schmies, B. Anke, H.N. Nong, J. Hübner, U. Gernert, M. Gliech, M. Lerch, P. Strasser, Ionomer distribution control in porous carbon-supported catalyst layers for high-power and low Pt-loaded proton exchange membrane fuel cells, Nat. Mater. 19 (2020) 77–85.
https://doi.org/10.1038/s41563-019-0487-0.

[25] K. Shinozaki, Suppression of oxygen reduction reaction activity on Pt-based electrocatalysts from ionomer incorporation, Journal of Power Sources. (2016).

[26] M. Lopez-Haro, L. Guétaz, T. Printemps, A. Morin, S. Escribano, P.-H. Jouneau, P. Bayle-Guillemaud, F. Chandezon, G. Gebel, Three-dimensional analysis of Nafion layers in fuel cell electrodes, Nat Commun. 5 (2014) 5229.
https://doi.org/10.1038/ncomms6229.

[27] X.-Z. Yuan, E. Gu, R. Bredin, M. Baker, S. Lee, T. Biggs, A. Bock, V. Banhardt, J. Russell, F. Girard, Development of a 3-in-1 device to simultaneously measure properties of gas diffusion layer for the quality control of proton exchange membrane fuel cell components, Journal of Power Sources. 477 (2020) 229009.
https://doi.org/10.1016/j.jpowsour.2020.229009.

[28] A. Ozden, S. Shahgaldi, X. Li, F. Hamdullahpur, A review of gas diffusion layers for proton exchange membrane fuel cells—With a focus on characteristics, characterization techniques, materials and designs, Progress in Energy and Combustion Science. 74 (2019) 50–102.
https://doi.org/10.1016/j.pecs.2019.05.002.

[29] D. Gerteisen, C. Sadeler, Stability and performance improvement of a polymer electrolyte membrane fuel cell stack by laser perforation of gas diffusion layers, Journal of Power Sources. 195 (2010) 5252–5257.
https://doi.org/10.1016/j.jpowsour.2010.03.021.

[30] C. Simon, F. Hasché, H.A. Gasteiger, Influence of the Gas Diffusion Layer Compression on the Oxygen Transport in PEM Fuel Cells at High Water Saturation Levels, J. Electrochem. Soc. 164 (2017) F591–F599.
https://doi.org/10.1149/2.0691706jes.

[31] Y. Wang, C.-Y. Wang, K.S. Chen, Elucidating differences between carbon paper and carbon cloth in polymer electrolyte fuel cells, Electrochimica Acta. 52 (2007) 3965–3975. https://doi.org/10.1016/j.electacta.2006.11.012.

[32] N.D. Neehall, M.S. Ismail, K.J. Hughes, M. Pourkashanian, Effect of composition and structure of gas diffusion layer and microporous layer on the through-plane gas permeability of PEFC porous media, Intl J of Energy Research. 45 (2021) 20988–21005. https://doi.org/10.1002/er.7158.

[33] N. Zamel, E. Litovsky, X. Li, J. Kleiman, Measurement of the through-plane thermal conductivity of carbon paper diffusion media for the temperature range from −50 to +120°C, International Journal of Hydrogen Energy. 36 (2011) 12618–12625. https://doi.org/10.1016/j.ijhydene.2011.06.097.

[34] C. Simon, D. Kartouzian, D. Müller, F. Wilhelm, H.A. Gasteiger, Impact of Microporous Layer Pore Properties on Liquid Water Transport in PEM Fuel Cells: Carbon Black Type and Perforation, J. Electrochem. Soc. 164 (2017) F1697–F1711. https://doi.org/10.1149/2.1321714jes.

[35] J. Wu, X. Yuan, H. Wang, M. Blanco, J. Martin, J. Zhang, Diagnostic tools in PEM fuel cell research: Part I Electrochemical techniques, International Journal of Hydrogen Energy. 33 (2008) 1735–1746. https://doi.org/10.1016/j.ijhydene.2008.01.013.

[36] Proton exchange membrane fuel cells: materials properties and performance[M]. CRC press, 2009.

[37] M. Grandi, S. Rohde, D.J. Liu, B. Gollas, V. Hacker, Recent advancements in high performance polymer electrolyte fuel cell electrode fabrication – Novel materials and manufacturing processes, Journal of Power Sources. 562 (2023) 232734. https://doi.org/10.1016/j.jpowsour.2023.232734.

[38] O.Z. Sharaf, M.F. Orhan, An overview of fuel cell technology: Fundamentals and applications, Renewable and Sustainable Energy Reviews. 32 (2014) 810–853. https://doi.org/10.1016/j.rser.2014.01.012.

[39] J.-H. Jung, S. Ahmed, Dynamic Model of PEM Fuel Cell Using Real-time Simulation Techniques, Journal of Power Electronics. 10 (2010) 739–748.
https://doi.org/10.6113/JPE.2010.10.6.739.

[40] Mench M M. Fuel cell engines[M]. John Wiley & Sons, 2008.

[41] N. Ramaswamy, W. Gu, J.M. Ziegelbauer, S. Kumaraguru, Carbon Support Microstructure Impact on High Current Density Transport Resistances in PEMFC Cathode, J. Electrochem. Soc. 167 (2020) 064515.
https://doi.org/10.1149/1945-7111/ab819c.

[42] E. Padgett, V. Yarlagadda, M.E. Holtz, M. Ko, B.D.A. Levin, R.S. Kukreja, J.M. Ziegelbauer, R.N. Andrews, J. Ilavsky, A. Kongkanand, D.A. Muller, Mitigation of PEM Fuel Cell Catalyst Degradation with Porous Carbon Supports, J. Electrochem. Soc. 166 (2019) F198–F207.
https://doi.org/10.1149/2.0371904jes.

[43] A. Öztürk, B. Fıçıcılar, İ. Eroğlu, and A. Bayrakçeken Yurtcan, Facilitation of water management in low Pt loaded PEM fuel cell by creating hydrophobic microporous layer with PTFE, FEP and PDMS polymers: Effect of polymer and carbon amounts, Int. J. Hydrog. Energy, 42 (2017).
https://doi.org/10.1016/j.ijhydene.2017.06.202.

[44] A.K.C. Wong, N. Ge, P. Shrestha, H. Liu, K. Fahy, and A. Bazylak, Polytetrafluoroethylene content in standalone microporous layers: Tradeoff between membrane hydration and mass transport losses in polymer electrolyte membrane fuel cells, Applied Energy, 240 (2019).
https://doi.org/10.1016/j.apenergy.2019.02.037.

[45] M.V. Williams, H.R. Kunz, J.M. Fenton, Analysis of Polarization Curves to Evaluate Polarization Sources in Hydrogen/Air PEM Fuel Cells, J. Electrochem. Soc. 152 (2005) A635.
https://doi.org/10.1149/1.1860034.

[46] Y.-J. Wang, W. Long, L. Wang, R. Yuan, A. Ignaszak, B. Fang, D.P. Wilkinson, Unlocking the door to highly active ORR catalysts for PEMFC applications: polyhedron-engineered Pt-based nanocrystals, Energy Environ. Sci. 11 (2018) 258–275.
https://doi.org/10.1039/C7EE02444D.

[47] J.M. Morgan, and R. Datta, Understanding the gas diffusion layer in proton exchange membrane fuel cells. I. How its structural characteristics affect diffusion and performance, J. Power Sources, 251 (2014).
https://doi.org/10.1016/j.jpowsour.2013.09.090.
[48] Y. Nagai, J. Eller, T. Hatanaka, S. Yamaguchi, S. Kato, A. Kato, F. Marone, H. Xu, and F. N. Büchi, Improving water management in fuel cells through microporous layer modifications: Fast operando tomographic imaging of liquid water, J. Power Sources, 435, (2019).
https://doi.org/10.1016/j.jpowsour.2019.226809.
[49] P. Carrère, and M. Prat, Impact of the anode operating conditions on the liquid water distribution in the cathode gas diffusion layer, Int. J. Hydrog. Energy, 46(33), (2021).
https://doi.org/10.1016/j.ijhydene.2020.03.120.
[50] Z. Qi, and A. Kaufman, Improvement of water management by a microporous sublayer for PEM fuel cells, J. Power Sources, 109(1), (2002).
https://doi.org/10.1016/S0378-7753(02)00058-7.
[51] P. M. Wilde, M. Mändle, M. Murata, and N. Berg, Structural and Physical Properties of GDL and GDL/BPP Combinations and their Influence on PEMFC Performance, Fuel Cells, 4(3),180(2004).
https://doi.org/10.1002/fuce.200400022
[52] J. Chen, T. Matsuura, and M. Hori, Novel gas diffusion layer with water management function for PEMFC, J. Power Sources, 131, 1–2(2004).
https://doi.org/10.1016/j.jpowsour.2004.01.007.
[53] N. Wu, Y. Liu, X. Tian, F. Liu, Y. Ma, S. Zhang, Q. Zhang, D. Hou, Y. Qi, R. Yang, L. Wang, The microporous layer in proton exchange membrane fuel cells, from transport mechanism to structural design, Journal of Power Sources. 580 (2023) 233412.
https://doi.org/10.1016/j.jpowsour.2023.233412.
[54] J.P. Owejan, J.E. Owejan, W. Gu, T.A. Trabold, T.W. Tighe, M.F. Mathias, Water Transport Mechanisms in PEMFC Gas Diffusion Layers, J. Electrochem. Soc. 157 (2010) B1456.
https://doi.org/10.1149/1.3468615.

[55] P.K. Sinha, C.-Y. Wang, Liquid water transport in a mixed-wet gas diffusion layer of a polymer electrolyte fuel cell, Chemical Engineering Science. 63 (2008) 1081–1091. https://doi.org/10.1016/j.ces.2007.11.007.

[56] M.N. Islam, U. Shrivastava, M. Atwa, X. Li, V. Birss, K. Karan, Highly Ordered Nanoporous Carbon Scaffold with Controllable Wettability as the Microporous Layer for Fuel Cells, ACS Appl. Mater. Interfaces. 12 (2020) 39215–39226. https://doi.org/10.1021/acsami.0c10755.

[57] D.R. Baker, D.A. Caulk, K.C. Neyerlin, M.W. Murphy, Measurement of Oxygen Transport Resistance in PEM Fuel Cells by Limiting Current Methods, J. Electrochem. Soc. 156 (2009) B991. https://doi.org/10.1149/1.3152226.

[58] N. Nonoyama, S. Okazaki, A.Z. Weber, Y. Ikogi, T. Yoshida, Analysis of Oxygen-Transport Diffusion Resistance in Proton-Exchange-Membrane Fuel Cells, J. Electrochem. Soc. 158 (2011) B416. https://doi.org/10.1149/1.3546038.

[59] D.R. Baker, D.A. Caulk, Limiting Current as a Tool to Study Oxygen Transport in PEM Fuel Cells, ECS Trans. 50 (2013) 35–45. https://doi.org/10.1149/05002.0035ecst.

[60] Y. Ono, T. Mashio, S. Takaichi, A. Ohma, H. Kanesaka, K. Shinohara, The Analysis of Performance Loss with Low Platinum Loaded Cathode Catalyst Layers, ECS Trans. 28 (2010) 69–78. https://doi.org/10.1149/1.3496614.

[61] R. Jinnouchi, K. Kudo, K. Kodama, N. Kitano, T. Suzuki, S. Minami, K. Shinozaki, N. Hasegawa, A. Shinohara, The role of oxygen-permeable ionomer for polymer electrolyte fuel cells, Nat Commun. 12 (2021) 4956. https://doi.org/10.1038/s41467-021-25301-3.

[62] K. Kudo, R. Jinnouchi, Y. Morimoto, Humidity and Temperature Dependences of Oxygen Transport Resistance of Nafion Thin Film on Platinum Electrode, Electrochimica Acta. 209 (2016) 682–690. https://doi.org/10.1016/j.electacta.2016.04.023.

[63] R. Jinnouchi, K. Kudo, N. Kitano, Y. Morimoto, Molecular Dynamics Simulations on O 2 Permeation through Nafion Ionomer on Platinum Surface, Electrochimica Acta. 188 (2016) 767–776.
https://doi.org/10.1016/j.electacta.2015.12.031
.[64] R. Haider, Y. Wen, Z.-F. Ma, D.P. Wilkinson, L. Zhang, X. Yuan, S. Song, J. Zhang, High temperature proton exchange membrane fuel cells: progress in advanced materials and key technologies, Chem. Soc. Rev. 50 (2021) 1138–1187.
https://doi.org/10.1039/D0CS00296H.
[65] F.S. Nanadegani, E.N. Lay, B. Sunden, Effects of an MPL on water and thermal management in a PEMFC, Int J Energy Res. 43 (2019) 274–296.
https://doi.org/10.1002/er.4262.
[66] Y. Yu, S. Chen, H. Wei, Numerical study on the effect of microporous layer crack changes on water management in gas diffusion layer of proton exchange membrane fuel cell, International Journal of Heat and Mass Transfer. 212 (2023) 124275.
https://doi.org/10.1016/j.ijheatmasstransfer.2023.124275.
[67] G. Inoue, K. Park, M. So, N. Kimura, Y. Tsuge, Microscale simulations of reaction and mass transport in cathode catalyst layer of polymer electrolyte fuel cell, International Journal of Hydrogen Energy. 47 (2022) 12665–12683.
https://doi.org/10.1016/j.ijhydene.2022.02.021.
[68] G. Inoue, S. Takenaka, Design of Interfaces and Phase Interfaces on Cathode Catalysts for Polymer Electrolyte Fuel Cells, Chem. Lett. 50 (2021) 136–143.
https://doi.org/10.1246/cl.200649.
[69] P.K. Sinha, C.-Y. Wang, Liquid water transport in a mixed-wet gas diffusion layer of a polymer electrolyte fuel cell, Chemical Engineering Science. 63 (2008) 1081–1091.
https://doi.org/10.1016/j.ces.2007.11.007.
[70] G. Luo, Y. Ji, C.-Y. Wang, P.K. Sinha, Modeling liquid water transport in gas diffusion layers by topologically equivalent pore network, Electrochimica Acta. 55 (2010) 5332–5341.
https://doi.org/10.1016/j.electacta.2010.04.078.

[71] J. Zhang, B. Wang, J. Jin, S. Yang, G. Li, A review of the microporous layer in proton exchange membrane fuel cells: Materials and structural designs based on water transport mechanism, Renewable and Sustainable Energy Reviews. 156 (2022) 111998. https://doi.org/10.1016/j.rser.2021.111998.

[72] M. Li, S. Foroughi, J. Zhao, B. Bijeljic, M.J. Blunt, Image-based pore-scale modelling of the effect of wettability on breakthrough capillary pressure in gas diffusion layers, Journal of Power Sources. 584 (2023) 233539. https://doi.org/10.1016/j.jpowsour.2023.233539.

[73] D. Zapardiel, P.A. García-Salaberri, Modeling the interplay between water capillary transport and species diffusion in gas diffusion layers of proton exchange fuel cells using a hybrid computational fluid dynamics formulation, Journal of Power Sources. 520 (2022) 230735. https://doi.org/10.1016/j.jpowsour.2021.230735.

[74] T. Agaesse, A. Lamibrac, F.N. Büchi, J. Pauchet, M. Prat, Validation of pore network simulations of ex-situ water distributions in a gas diffusion layer of proton exchange membrane fuel cells with X-ray tomographic images, Journal of Power Sources. 331 (2016) 462–474. https://doi.org/10.1016/j.jpowsour.2016.09.076.

[75] Z. Zhan, J. Xiao, D. Li, M. Pan, R. Yuan, Effects of porosity distribution variation on the liquid water flux through gas diffusion layers of PEM fuel cells, Journal of Power Sources. 160 (2006) 1041–1048. https://doi.org/10.1016/j.jpowsour.2006.02.060.

[76] Z. Zhan, J. Xiao, Y. Zhang, M. Pan, R. Yuan, Gas diffusion through differently structured gas diffusion layers of PEM fuel cells, International Journal of Hydrogen Energy. 32 (2007) 4443–4451. https://doi.org/10.1016/j.ijhydene.2007.03.041.

[77] R. Omrani, B. and Shabani, Gas diffusion layer modifications and treatments for improving the performance of proton exchange membrane fuel cells and electrolysers: A review, Int. J. Hydrog. Energy, 42 (2017). https://doi.org/10.1016/j.ijhydene.2017.09.132.

[78] S. Park, J.-W. Lee, and B.N. Popov, A review of gas diffusion layer in PEM fuel cells: Materials and designs, Int. J. Hydrog. Energy, 37 (2012). https://doi.org/10.1016/j.ijhydene.2011.12.148.

[79] T. Kitahara, H. Nakajima, M. Morishita, Water vapor exchange system using a hydrophilic microporous layer coated gas diffusion layer to enhance performance of polymer electrolyte fuel cells without cathode humidification, Journal of Power Sources. 214 (2012) 100–106. https://doi.org/10.1016/j.jpowsour.2012.04.067.

[80] F.C. Cetinbas, R.K. Ahluwalia, A.D. Shum, I.V. Zenyuk, Direct Simulations of Pore-Scale Water Transport through Diffusion Media, J. Electrochem. Soc. 166 (2019) F3001–F3008. https://doi.org/10.1149/2.0011907jes.

[81] M. Sarker, M.A. Rahman, F. Mojica, S. Mehrazi, W.J.M. Kort-Kamp, P.-Y.A. Chuang, Experimental and computational study of the microporous layer and hydrophobic treatment in the gas diffusion layer of a proton exchange membrane fuel cell, Journal of Power Sources. 509 (2021) 230350. https://doi.org/10.1016/j.jpowsour.2021.230350.

[82] T. Kitahara, T. Konomi, H. Nakajima, M. Murata, Effects of Design Parameters in Paper Type Gas Diffusion Layer on the Performance of Polymer Electrolyte Fuel Cells (Measures to Prevent Flooding and Drying-Up): (Measures to Prevent Flooding and Drying-Up), JEE. 4 (2009) 338–345. https://doi.org/10.1299/jee.4.338.

[83] J. Biesdorf, A. Forner-Cuenca, T.J. Schmidt, P. Boillat, Impact of Hydrophobic Coating on Mass Transport Losses in PEFCs, J. Electrochem. Soc. 162 (2015) F1243–F1252. https://doi.org/10.1149/2.0861510jes.

[84] Y. Nagai, J. Eller, T. Hatanaka, S. Yamaguchi, S. Kato, A. Kato, F. Marone, H. Xu, and F. N. Büchi, Improving water management in fuel cells through microporous layer modifications: Fast operando tomographic imaging of liquid water, J. Power Sources, 435, (2019). https://doi.org/10.1016/j.jpowsour.2019.226809.

[85] Y. Yang, X. Zhou, B. Li, C. Zhang, Recent progress of the gas diffusion layer in proton exchange membrane fuel cells: Material and structure designs of microporous layer, Int. J. Hydrog. Energy, 46(2021).
https://doi.org/10.1016/j.ijhydene.2020.10.185.
[86] NEDO Fuel Cell/Hydrogen Technology Development Roadmap-Fuel cell roadmap for FCV/HDV (explanatory manual), Japan New Energy and Industrial Technology Development Organization, (2023).
https://www.nedo.go.jp/content/100956711.pdf
[87] T. Kitahara, T. Konomi, H. Nakajima, Microporous layer coated gas diffusion layers for enhanced performance of polymer electrolyte fuel cells, Journal of Power Sources. 195 (2010) 2202–2211.
https://doi.org/10.1016/j.jpowsour.2009.10.089.
[88] G. Velayutham, Effect of micro-layer PTFE on the performance of PEM fuel cell electrodes, International Journal of Hydrogen Energy. 36 (2011) 14845–14850.
https://doi.org/10.1016/j.ijhydene.2011.03.037.
[89] S. Latorrata, M. Sansotera, M. Gola, P.G. Stampino, W. Navarrini, G. Dotelli, Innovative Perfluoropolyether-Functionalized Gas Diffusion Layers with Enhanced Performance in Polymer Electrolyte Membrane Fuel Cells, Fuel Cells. 20 (2020) 166–175.
https://doi.org/10.1002/fuce.201900169.
[90] A. Öztürk, B. Fıçıcılar, İ. Eroğlu, A. Bayrakçeken Yurtcan, Facilitation of water management in low Pt loaded PEM fuel cell by creating hydrophobic microporous layer with PTFE, FEP and PDMS polymers: Effect of polymer and carbon amounts, International Journal of Hydrogen Energy. 42 (2017) 21226–21249.
https://doi.org/10.1016/j.ijhydene.2017.06.202.
[91] A. Öztürk, A. Bayrakçeken Yurtcan, Effect of calcination temperature on hydrophobicity of microporous layers prepared with two different molecular weights of PDMS polymer on PEM fuel cell performance with low Pt loading, International Journal of Hydrogen Energy. 42 (2017) 6250–6261.
https://doi.org/10.1016/j.ijhydene.2016.11.041.

[92] A.L. Ong, A. Bottino, G. Capannelli, and A. Comite, Effect of preparative parameters on the characteristic of poly(vinylidene fluoride)-based microporous layer for proton exchange membrane fuel cells, *J. Power Sources*, **183** (2008).
https://doi.org/10.1016/j.jpowsour.2008.04.064.
[93] J. Cho, D. Kim, J.S. Yi, and S. Park, Microarchitecture of polyvinylidene fluoride-bound self-standing microporous layer and its implication to water management in fuel cells, J. Power Sources, 506 (2021).
https://doi.org/10.1016/j.jpowsour.2021.230129.
[94] A.K.C. Wong, N. Ge, P. Shrestha, H. Liu, K. Fahy, A. Bazylak, Polytetrafluoroethylene content in standalone microporous layers: Tradeoff between membrane hydration and mass transport losses in polymer electrolyte membrane fuel cells, Applied Energy. 240 (2019) 549–560.
https://doi.org/10.1016/j.apenergy.2019.02.037.
[95] E.M. Can, A. Mufundirwa, P. Wang, S. Iwasaki, T. Kitahara, H. Nakajima, M. Nishihara, K. Sasaki, S.M. Lyth, Superhydrophobic fluorinated carbon powders for improved water management in hydrogen fuel cells, Journal of Power Sources. 548 (2022) 232098.
https://doi.org/10.1016/j.jpowsour.2022.232098.
[96] F.-B. Weng, C.-Y. Hsu, M.-C. Su, Experimental study of micro-porous layers for PEMFC with gradient hydrophobicity under various humidity conditions, International Journal of Hydrogen Energy. 36 (2011) 13708–13714.
https://doi.org/10.1016/j.ijhydene.2011.07.141.
[97] H.-H. Chen, and M.-H. Chang, Effect of cathode microporous layer composition on proton exchange membrane fuel cell performance under different air inlet relative humidity, *J. Power Sources*, **232** (2013).
https://doi.org/10.1016/j.jpowsour.2013.01.079.
[98] F. Jinuntuya, M. Whiteley, R. Chen, A. Fly, The effects of gas diffusion layers structure on water transportation using X-ray computed tomography based Lattice Boltzmann method, Journal of Power Sources. 378 (2018) 53–65.
https://doi.org/10.1016/j.jpowsour.2017.12.016.

[99] Z. Fishman, A. Bazylak, Heterogeneous Through-Plane Porosity Distributions for Treated PEMFC GDLs I. PTFE Effect, J. Electrochem. Soc. 158 (2011) B841. https://doi.org/10.1149/1.3594578.

[100] Z. Zhan, J. Xiao, Y. Zhang, M. Pan, R. Yuan, Gas diffusion through differently structured gas diffusion layers of PEM fuel cells, International Journal of Hydrogen Energy. 32 (2007) 4443–4451. https://doi.org/10.1016/j.ijhydene.2007.03.041.

[101] J.H. Chun, K.T. Park, D.H. Jo, J.Y. Lee, S.G. Kim, E.S. Lee, J.-Y. Jyoung, S.H. Kim, Determination of the pore size distribution of micro porous layer in PEMFC using pore forming agents under various drying conditions, International Journal of Hydrogen Energy. 35 (2010) 11148–11153. https://doi.org/10.1016/j.ijhydene.2010.07.056.

[102] G. Athanasaki, Q. Wang, X. Shi, N. Chauhan, V. Vimala, L. Cindrella, R. Ahmad, A.M. Kannan, Design and development of gas diffusion layers with pore forming agent for proton exchange membrane fuel cells at various relative humidity conditions, International Journal of Hydrogen Energy. 46 (2021) 6835–6844. https://doi.org/10.1016/j.ijhydene.2020.11.187.

[103] D. Kartouzian, A. Mohseninia, H. Markötter, P. Langner, J. Scholta, and I. Manke, Impact of Porosity Gradients within Catalyst Layer and MPL of a PEM Fuel Cell on the Water Management and Performance: A Neutron Radiography Investigation, ECS Trans., 92 (2019). https://doi.org/10.1149/09208.0135ecst.

[104] G. Lin, S. Liu, G. Qu, Y. Song, T. Li, F. Liu, Y. Hu, Effect of pore size distribution in the gas diffusion layer adjusted by composite carbon black on fuel cell performance, Int J Energy Res. 45 (2021) 7689–7702. https://doi.org/10.1002/er.6350.

[105] T. Tanuma, M. Kawamoto, Effect of Pore Volume of Hydrophilic Microporous Layer (MPL) on PEFC Performance, ECS Trans. 69 (2015) 1323–1329. https://doi.org/10.1149/06917.1323ecst.

[106] H. Tang, S. Wang, M. Pan, R. Yuan, Porosity-graded micro-porous layers for polymer electrolyte membrane fuel cells, Journal of Power Sources. 166 (2007) 41–46. https://doi.org/10.1016/j.jpowsour.2007.01.021.

[107] R. Lin, L. Chen, T. Zheng, S. Tang, X. Yu, M. Dong, Z. Hao, Interfacial water management of gradient microporous layer for self-humidifying proton exchange membrane fuel cells, International Journal of Heat and Mass Transfer. 175 (2021) 121340. https://doi.org/10.1016/j.ijheatmasstransfer.2021.121340.

[108] T. Li, K. Wang, J. Wang, Y. Liu, Y. Han, Z. Xu, G. Lin, Y. Liu, Optimization of GDL to improve water transferability, Renewable Energy. 179 (2021) 2086–2093. https://doi.org/10.1016/j.renene.2021.08.026.

[109] D. Ko, S. Doh, H.S. Park, M.H. Kim, The effect of through plane pore gradient GDL on the water distribution of PEMFC, International Journal of Hydrogen Energy. 43 (2018) 2369–2380. https://doi.org/10.1016/j.ijhydene.2017.12.007.

[110] C. Zhao, H. Zhang, Z. Huang, M. Zhao, H. Chen, G. Lin, Two-Stage Microporous Layers with Gradient Pore Size Structure for Improving the Performance of Proton Exchange Membrane Fuel Cells, Polymers. 15 (2023) 2740. https://doi.org/10.3390/polym15122740.

[111] H. Oh, J. Park, K. Min, E. Lee, J.-Y. Jyoung, Effects of pore size gradient in the substrate of a gas diffusion layer on the performance of a proton exchange membrane fuel cell, Applied Energy. 149 (2015) 186–193. https://doi.org/10.1016/j.apenergy.2015.03.072.

[112] J. Kim, H. Kim, H. Song, D. Kim, G.H. Kim, D. Im, Y. Jeong, T. Park, Carbon nanotube sheet as a microporous layer for proton exchange membrane fuel cells, Energy. 227 (2021) 120459. https://doi.org/10.1016/j.energy.2021.120459.

[113] H. Ito, Y. Heo, M. Ishida, A. Nakano, S. Someya, T. Munakata, Application of a self-supporting microporous layer to gas diffusion layers of proton exchange membrane fuel cells, Journal of Power Sources. 342 (2017) 393–404. https://doi.org/10.1016/j.jpowsour.2016.12.064.

[114] Y.W. Chen-Yang, T.F. Hung, J. Huang, F.L. Yang, Novel single-layer gas diffusion layer based on PTFE/carbon black composite for proton exchange membrane fuel cell, Journal of Power Sources. 173 (2007) 183–188.
https://doi.org/10.1016/j.jpowsour.2007.04.080.
[115] Q. Duan, B. Wang, J. Wang, H. Wang, Y. Lu, Fabrication of a carbon nanofiber sheet as a micro-porous layer for proton exchange membrane fuel cells, Journal of Power Sources. 195 (2010) 8189–8193.
https://doi.org/10.1016/j.jpowsour.2010.07.032.
[116] D. Spernjak, R. Mukundan, R.L. Borup, L.G. Connolly, B.I. Zackin, V. De Andrade, M. Wojcik, D.Y. Parkinson, D.L. Jacobson, D.S. Hussey, K.L. More, T. Chan, A.Z. Weber, and I.V. Zenyuk, Enhanced Water Management of Polymer Electrolyte Fuel Cells with Additive-Containing Microporous Layers, ACS Appl. Energy Mater., 1 (2018).
https://doi.org/10.1021/acsaem.8b01059.
[117] T. Kitahara, and H. Nakajima, Microporous layer-coated gas diffusion layer to reduce oxygen transport resistance in a polymer electrolyte fuel cell under high humidity conditions, Int. J. Hydrog. Energy, 41 (2016).
https://doi.org/10.1016/j.ijhydene.2016.04.117.
[118] T. Kitahara, H. Nakajima, M. Inamoto, and M. Morishita, Novel hydrophilic and hydrophobic double microporous layer coated gas diffusion layer to enhance performance of polymer electrolyte fuel cells under both low and high humidity, J. Power Sources, 234 (2013).
https://doi.org/10.1016/j.jpowsour.2013.01.150.
[119] T. Kitahara, H. Nakajima, and K. Okamura, Gas diffusion layers coated with a microporous layer containing hydrophilic carbon nanotubes for performance enhancement of polymer electrolyte fuel cells under both low and high humidity conditions, J. Power Sources, 283 (2015).
https://doi.org/10.1016/j.jpowsour.2015.02.115.
[120] T. Kitahara, H. Nakajima, and K. Mori, Hydrophilic and hydrophobic double microporous layer coated gas diffusion layer for enhancing performance of polymer electrolyte fuel cells under no-humidification at the cathode, J. Power Sources, 199 (2012).
https://doi.org/10.1016/j.jpowsour.2011.10.002.

[121] M. Ahn, Y. H. Cho, Y. H. Cho, J. Kim, N. Jung, and Y. E. Sung, Influence of hydrophilicity in micro-porous layer for polymer electrolyte membrane fuel cells, Electrochim. Acta, 56, 5(2011).
https://doi.org/10.1016/j.electacta.2010.11.063.

[122] T. Tanuma, S. Kinoshita, Impact of Gas Diffusion Layers (GDLs) on Water Transport in PEFCs, J. Electrochem. Soc. 159 (2011) B150–B154.
https://doi.org/10.1149/2.054202jes.

[123] T. Tanuma, Innovative Hydrophilic Microporous Layers for Cathode Gas Diffusion Media, J. Electrochem. Soc. 157 (2010) B1809.
https://doi.org/10.1149/1.3494603.

[124] T. Tanuma, M. Kawamoto, S. Kinoshita, Effect of Properties of Hydrophilic Microporous Layer (MPL) on PEFC Performance, J. Electrochem. Soc. 164 (2017) F499–F503.
https://doi.org/10.1149/2.0371706jes.

[125] C. Simon, J. Endres, B. Nefzger-Loders, F. Wilhelm, and H.A. Gasteiger, Interaction of Pore Size and Hydrophobicity/Hydrophilicity for Improved Oxygen and Water Transport through Microporous Layers, J. Electrochem. Soc., 166 (2019).
https://doi.org/10.1149/2.1111913jes.

[126] R. Schweiss, M. Steeb, P.M. Wilde, Mitigation of Water Management in PEM Fuel Cell Cathodes by Hydrophilic Wicking Microporous Layers, Fuel Cells. 10 (2010) 1176–1180.
https://doi.org/10.1002/fuce.201000003.

[127] G. Wang, Y. Utaka, S. Wang, Planar-distributed wettability of microporous layer of polymer electrolyte fuel cell to improve cold start performance, Journal of Power Sources. 437 (2019) 226930.
https://doi.org/10.1016/j.jpowsour.2019.226930.

[128] R. Lin, M. Dong, S. Lan, M. Lou, Numerical simulation of liquid water transport in perforated cracks of microporous layer, Energy. 262 (2023) 125372.
https://doi.org/10.1016/j.energy.2022.125372.

[129] M.P. Manahan, J.T. Clement, A.K. Srouji, S.W. Brown, T. Reutzel, M.M. Mench, Laser Modified Fuel Cell Diffusion Media: Engineering Enhanced Performance via Localized Water Redistribution, J. Electrochem. Soc. 161 (2014) F1061–F1069. https://doi.org/10.1149/2.0591410jes.

[130] R. Alink, J. Haußmann, H. Markötter, M. Schwager, I. Manke, D. Gerteisen, The influence of porous transport layer modifications on the water management in polymer electrolyte membrane fuel cells, Journal of Power Sources. 233 (2013) 358–368. https://doi.org/10.1016/j.jpowsour.2013.01.085.

[131] R. Banerjee, N. Ge, J. Lee, M.G. George, S. Chevalier, H. Liu, P. Shrestha, D. Muirhead, A. Bazylak, Transient Liquid Water Distributions in Polymer Electrolyte Membrane Fuel Cell Gas Diffusion Layers Observed through In-Operando Synchrotron X-ray Radiography, J. Electrochem. Soc. 164 (2017) F154–F162. https://doi.org/10.1149/2.0991702jes.

[132] H. Naito, K. Ishikawa, T. Sasabe, S. Hirai, T. Tanuma, Investigation of effects of hydrophilic micro-porous layer on liquid water behavior by X-ray imaging, Journal of Power Sources. 507 (2021) 230285. https://doi.org/10.1016/j.jpowsour.2021.230285.

[133] Y. Aoyama, Y. Tabe, R. Nozaki, K. Suzuki, T. Chikahisa, T. Tanuma, Analysis of Water Transport inside Hydrophilic Carbon Fiber Micro-Porous Layers with High-Performance Operation in PEFC, J. Electrochem. Soc. 165 (2018) F484–F491. https://doi.org/10.1149/2.0801807jes.

[134] P. Shrestha, R. Banerjee, J. Lee, N. Ge, D. Muirhead, H. Liu, A.K.C. Wong, D. Ouellette, B. Zhao, A. Bazylak, Hydrophilic microporous layer coatings for polymer electrolyte membrane fuel cells operating without anode humidification, Journal of Power Sources. 402 (2018) 468–482. https://doi.org/10.1016/j.jpowsour.2018.08.062.

[135] Y. Hou, X. Li, Q. Du, K. Jiao, N. Zamel, Pore-Scale Investigation of the Effect of Micro-Porous Layer on Water Transport in Proton Exchange Membrane Fuel Cell, J. Electrochem. Soc. 167 (2020) 144504. https://doi.org/10.1149/1945-7111/abc30a.

[136] P.Z. Lin, J. Sun, M.H. Shao, M.C. Wu, T.S. Zhao, Modeling proton exchange membrane fuel cells with fiber-based microporous layers, International Journal of Heat and Mass Transfer 198 (2022) 123398.
https://doi.org/10.1016/j.ijheatmasstransfer.2022.123398.

[137] M. Mortazavi, and K. Tajiri, Effect of the PTFE content in the gas diffusion layer on water transport in polymer electrolyte fuel cells (PEFCs), J. Power Sources, 245 (2014).
https://doi.org/10.1016/j.jpowsour.2013.06.138.

[138] Z. Fishman, A. Bazylak, Heterogeneous Through-Plane Porosity Distributions for Treated PEMFC GDLs. II. Effect of MPL Cracks, J. Electrochem. Soc. 158 (2011) B846.
https://doi.org/10.1149/1.3594636.

[139] J. Dai, Y. Gao, T. Zhang, Analysis on the influence of crack structure on MPL transmission properties, Journal of Power Sources. 562 (2023) 232790.
https://doi.org/10.1016/j.jpowsour.2023.232790.

[140] T. Sasabe, P. Deevanhxay, S. Tsushima, S. Hirai, Soft X-ray visualization of the liquid water transport within the cracks of micro porous layer in PEMFC, Electrochemistry Communications. 13 (2011) 638–641.
https://doi.org/10.1016/j.elecom.2011.03.033.

[141] S. Wang, S. Guan, L. Zhang, F. Zhou, J. Tan, M. Pan, Enhancing the properties of water and gas management for proton exchange membrane fuel cells via tailored intersected cracks in a microporous layer, Journal of Power Sources. 533 (2022) 231402.
https://doi.org/10.1016/j.jpowsour.2022.231402.

[142] D. Niblett, V. Niasar, S. Holmes, A. Mularczyk, J. Eller, R. Prosser, M. Mamlouk, Water cluster characteristics of fuel cell gas diffusion layers with artificial microporous layer crack dilation, Journal of Power Sources. 555 (2023) 232383.
https://doi.org/10.1016/j.jpowsour.2022.232383.

[143] F.C. Lee, M.S. Ismail, D.B. Ingham, K.J. Hughes, L. Ma, S.M. Lyth, M. Pourkashanian, Alternative architectures and materials for PEMFC gas diffusion layers: A review and outlook, Renewable and Sustainable Energy Reviews. 166 (2022) 112640.
https://doi.org/10.1016/j.rser.2022.112640.

[144] C.H. Kung, P.K. Sow, B. Zahiri, W. Mérida, Assessment and Interpretation of Surface Wettability Based on Sessile Droplet Contact Angle Measurement: Challenges and Opportunities, Adv Materials Inter. 6 (2019) 1900839.
https://doi.org/10.1002/admi.201900839.
[145] NEDO PEFC Cell Evaluation Analysis Protocol, Japan New Energy and Industrial Technology Development Organization, (2023).
https://www.nedo.go.jp/content/100963953.pdf
[146] J.P. Owejan, T.A. Trabold, M.M. Mench, Oxygen transport resistance correlated to liquid water saturation in the gas diffusion layer of PEM fuel cells, International Journal of Heat and Mass Transfer. 71 (2014) 585–592.
https://doi.org/10.1016/j.ijheatmasstransfer.2013.12.059.
[147] J.P. Owejan, J.J. Gagliardo, R.C. Reid, T.A. Trabold, Proton transport resistance correlated to liquid water content of gas diffusion layers, Journal of Power Sources. 209 (2012) 147–151.
https://doi.org/10.1016/j.jpowsour.2012.02.087.